UNIVERSITÀ DEGLI STUDI DI MILANO

Scuola di Dottorato in Fisica, Astrofisica e Fisica Applicata

Dipartimento di Fisica

Corso di Dottorato in Fisica, Astrofisica e Fisica Applicata

Ciclo XXXV

Investigating the origins of UHECRs using the Pierre Auger Observatory and paleo-detectors

Settore Scientifico Disciplinare FIS/01

Supervisor: Prof. Lino MIRAMONTI

Co-supervisor: Dr. Lorenzo CACCIANIGA

Coordinator: Prof. Matteo PARIS

Tesi di Dottorato di:

Claudio Galelli

Anno Accademico 2021-2022

External referees of the thesis:

Prof. Foteini Oikonomou

Prof. Markus Ahlers

Commission of the final examination:

Prof. Luigi Guzzo

Prof. Elisa Resconi

Prof. Olivier Deligny

Final examination:

Date: 08/02/2023

Università degli Studi di Milano, Dipartimento di Fisica, Milano, Italy

Abstract

A very fascinating region for investigating the origins of cosmic rays is the *toe* of the ultra-high energy cosmic ray (UHECR) spectrum, above ≈ 50 EeV. The potential for small magnetic deflections at these energies is coupled with the presence of flux suppression, which may be a sign of the sources' maximum acceleration potential or may have an explanation for the interactions of cosmic rays with background photons, effectively restricting the region of interest in the search for UHECR sources to a relatively small bubble around us. In this thesis, I present the latest dataset of cosmic rays at the highest energies collected by the Pierre Auger Observatory, the largest experiment dedicated to UHECR science ever built, and the anisotropy searches carried out using it. I have carried out blind, model-independent searches for overdensities, astrophysical structural correlation analysis, and cross-correlation investigations with catalogs of candidate sources. For UHECRs with energy greater than 38 EeV, the results show evidence of a deviation from isotropy at an angular scale of $\approx 25°$ at the 4σ level. Additionally in this thesis for the first time, I present the possibility of using ancient minerals as *paleo-detectors* to study the history of the flux of cosmic rays in the past by detecting the tracks left in the mineral structure by the interactions between ions and energetic secondary cosmic rays present in the extensive air showers.

The first chapter of the thesis is a description of the current knowledge on cosmic rays, their possible sources, propagation, and general measured characteristics. Chapter 2 describes in more detail the phenomenon of extensive

air showers (EAS), their properties, and the techniques for the indirect detection of UHECRs. Chapter 3 is an overview of the Pierre Auger Observatory, its technical features, event reconstruction procedures, and main scientific results. Chapter 4 presents the first contribution of this thesis: the construction of the largest dataset ever built of UHECRs with energy above 32 EeV and its selection procedure. Chapter 5 describes the intermediate scale anisotropy searches conducted using this dataset, the results, and their interpretations, together with the side analysis on small and extra-small scale anisotropies used to look for clusters of neutral particles around Galactic candidate sources. Chapter 6 describes the paleo-detector technique, its current proposed application to the detection of rare events, and an original proposal to apply it to UHECR studies.

Contents

Chapter 1

High energy cosmic rays

Cosmic rays have been central in the history of particle and high energy physics since their discovery in 1912 by Victor Hess, shown in figure 1.1 at the departure of one of its flights, who was awarded the Nobel prize in Physics in 1936. Most of the particles discovered in the first half of the XX century, such as pions and muons, come from cosmic rays, which remained the only source of high-energy particles to study fundamental physics until the construction of the first large accelerators.
A great boost in the understanding of cosmic rays came with the discovery of Extensive Air Showers (EASs) through particle coincidence by Bruno Rossi in 1934 and in 1937 by Pierre Auger, who, with his team, was also able to estimate the energy of the primary particle.

In the 1960s, following the discovery of the Cosmic Microwave Background (CMB) by Penzias and Wilson [1], Greisen and, independently, Zatsepin and Kuzmin, theorized the suppression of the flux of cosmic rays above $\approx$50 EeV (5×10^{19} eV) [2][3]; a compatible suppression was observed by the HiRes observatory [4] and, more recently, confirmed by the results of the Pierre Auger Observatory [5] [6].
In this first chapter, the current knowledge of cosmic rays will be presented, including spectrum, composition, arrival direction, and secondary particle production.

Figure 1.1: Viktor Hess at the departure of one of his hot air balloon flights from Vienna, around 1912. Credits to the Viktor Franz Hess Society

1.1 The cosmic ray spectrum

From 10^9 to 10^{20} eV, the cosmic ray spectrum is well described by a power law $\frac{dN}{dE} = E^{-\gamma}$. The factor γ is, apart from a couple of interesting features that will be discussed later, strikingly stable over 10 orders of magnitude, at a value of ~ 2.7, as visible in figure 1.2. This makes it so that 10 orders of magnitude translate to slightly less than 30 orders of flux, and this enormous difference impacts massively the studies at the highest energies: if for particles with an energy of the order of the GeV, the flux is more than 10000 particles per square meter every second, at the highest energies this is reduced to one particle per square kilometer every century, or even less. For this reason, direct detection of cosmic rays is only feasible up to energies around 100 TeV. At higher energies instead, cosmic rays are detected indirectly by sampling the EAS that is created by the interaction of the primary particles with molecules in the atmosphere. The fundamentals of indirect detection of cosmic rays will be discussed in chapter 2. This technique has the advantage of providing much higher statistics than direct detection, but crucially the most important properties of the primary (energy, mass, arrival direction) must then be reconstructed rather than directly measured.

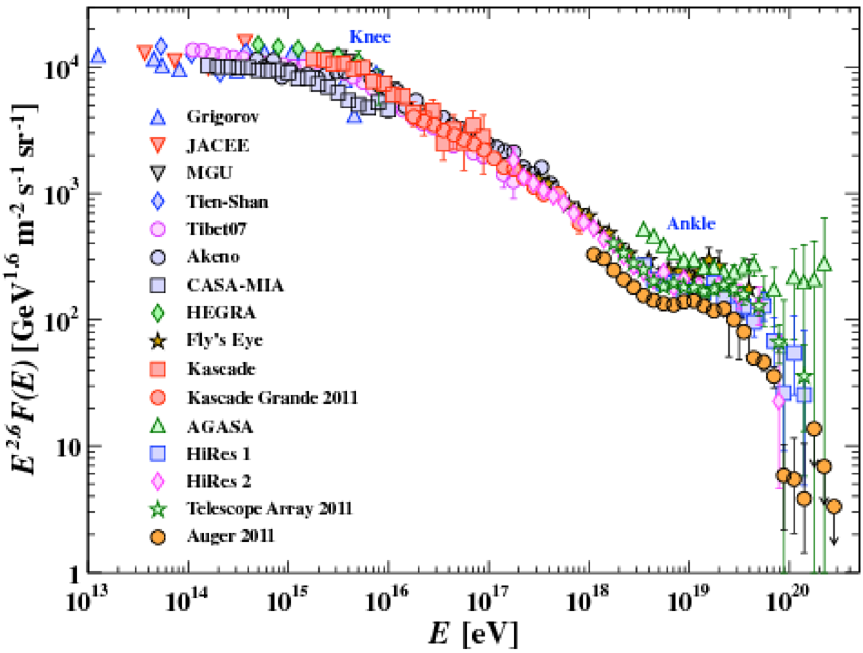

Figure 1.2: Cosmic ray flux (multiplied by energy$^{2.6}$) as a function of energy, measured by various past and present experiments. From [7].

Features of the cosmic ray spectrum

As previously stated, the cosmic ray spectrum is overall well described by a power law $\frac{dN}{dE} = E^{-\gamma}$, with $\gamma = 2.7$. However, a few features that modify the spectral index are present. These spectral features are generally named after the features of the human leg, because of shape similarity.

- The **knee** is a softening of the spectrum at around 5×10^{15} eV, where the spectral index rises from 2.7 to 3.0. This is thought to be a reflection of a limit of the confinement power of Galactic sources of light cosmic rays, which at this energy start to have a Larmor radius larger than the characteristic size of the shocks, thus escaping before being accelerated. As the radius, and therefore the maximum accelerating energy, depends on the charge of the primary particle, the steepening of the flux is the effect of the superposition of the spectra of heavier and heavier nuclei, which have a higher and higher cut-off energy.

- The **second knee** at roughly 10^{17} eV is an additional softening of the spectrum, which has a spectral index of 3.3. The second knee is also known as the *iron knee* [8], as it is thought to correspond to the energetic limit for Galactic sources accelerating iron nuclei. The origin of the component, Galactic or extragalactic, that makes up the region above the second knee but below the *ankle* is still being debated.

- The **ankle** at 4×10^{18} eV, the spectral index falls back to 2.7. Many alternative explanations for this feature exist, all tied to the presence of the transition between the Galactic and extragalactic components. Traditionally, the feature was explained as the simple transition from a very steep Galactic component to a flatter extragalactic proton contribution [9]. The *dip model* [10] assumes that the transition to a pure-proton extragalactic component is happening before the ankle, around the EeV: the ankle would be a feature due to proton energy losses through the interaction with the CMB creating electron-positron pairs. this model is currently disfavoured due to the heavier composition measured in the ankle region. The *mixed composition model* [11] assumes that a distinct light Galactic component dominates below the ankle, where a transition to an extragalactic component containing a fraction of heavier nuclei occurs. The feature would be the direct signature of the Galactic-extragalactic transition. The third, more recent model [12] theorizes that the observed spectral features and composition are the result of the photodisintegration of ultra-high energy nuclei in the vicinity of the sources; the environments close to the sources would act like a filter, allowing the highest energy nuclei to escape while disintegrating the lower energy ones, creating A nucleons of energy 1/A. The knocked-off nucleons naturally produce the feature and explain the transition from a lighter component to a heavier one at higher energies. Different model predictions are shown in figure 1.3.

- The **instep**, a recently discovered softening to index 3 at around $10 - 15 \times 10^{18}$ eV, which takes the name from the almost flat appearance in the common $J \times E^3$ visualization of the spectrum. The cause of this feature is thought to be the gradual change in composition towards heavy elements in the extragalactic components.

- The **toe**, at $40 - 50 \times 10^{18}$ eV is a steep increase in the spectral index which could be explained as the signature of the GZK effect cited above in the text, i.e. the interaction with high energy loss between cosmic rays and CMB photons. This effect will be discussed more precisely in a subsequent section. Another explanation for the toe could simply be a strong limit on the energies that can be reached inside the sources of UHECRs.

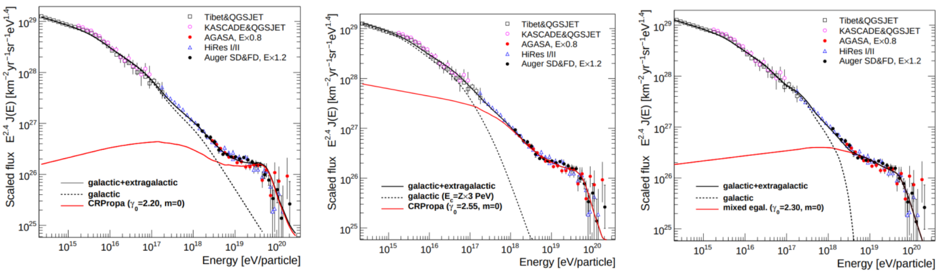

Figure 1.3: The three plots compare three different models to describe the ankle: the traditional ankle scenario with a flat extragalactic component, the dip scenario and the mixed composition scenario. From [13]

1.2 Mass composition

Under 100 TeV of energy, as cosmic rays are detected by satellite-borne experiments, the composition is directly measurable by spectrometers, such as the Alpha Magnetic Spectrometer (AMS-02) [14] on board the International Space Station. In this low energy region, the most abundant particles are protons and helium nuclei, which together make up around 99% of the particle fraction; electrons make up 1% circa of the flux while being absent at higher energies. The study of the presence of more exotic and low-abundance particles, such as positrons, antiprotons, anti-helium, ultra-heavy nuclei, radioactive isotopes, and dark matter, is a very active field of

astroparticle physics, with many space-based experiments, such as AMS-02, DAMPE [15], CALET [16] and more.
For indirect detection experiments, the determination of the mass of the primary particle is much more complex, as it has to be inferred from the characteristics of the EAS. The most used shower parameters to study the mass are the detection of the Cherenkov light (Tunka-133), the number of muons (KASCADE-Grande [17], IceTop [18], Pierre Auger Observatory) and the measurement of the shower maximum (Auger, Telescope Array (TA)) [19])[20]. The main obstacles in determining the primary species from the shower parameters are the statistical fluctuations between showers also of the same primary and the fact that the measurements have to be compared to non-completely reliable interaction models obtained from experiments in accelerators. A more thorough discussion of the models will be given in chapter 2.
Experimental results for average cosmic ray mass show a rise from lighter to heavier particles between 1 and 100 PeV [21][22][23]][24], a fact that supports the models proposed to explain the behavior of the cosmic rays spectrum between the *knee* and *second knee*; after that, a steep drop towards the lighter components is observed, with an almost proton-like composition around the EeV. The results at these energies are shown in figure 1.4. At higher energies, results from the Pierre Auger Observatory show an increase in the average mass of the particles, pointing to a mixed to heavy composition at the highest components of the spectrum (figure 1.5) [25], while the Telescope Array Collaboration supports instead a proton-like model [26]. The effective composition of the cosmic ray spectrum above the *ankle* is still one of the most important open problems in astroparticle physics.

1.3 Cosmic ray propagation

Cosmic rays propagate through a diffusive process as they are charged particles, their trajectory being affected by the Galactic and extragalactic magnetic fields. At the highest energies, cosmic rays can also interact with background radiation, modifying their propagation further.

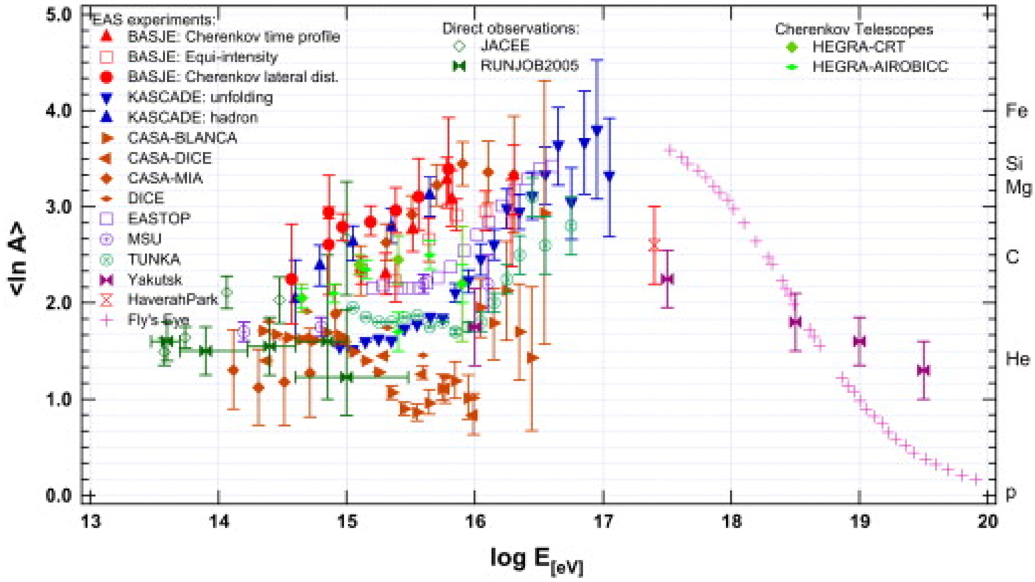

Figure 1.4: Average CR mass as a function of energy from different detectors, obtained comparing results to model predictions. From [27].

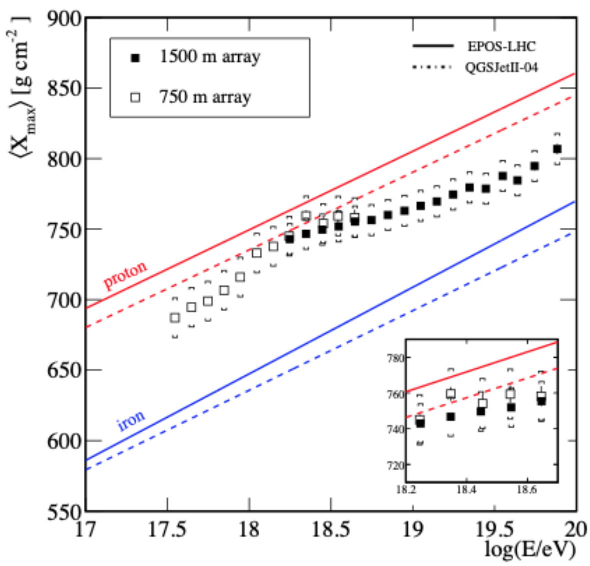

Figure 1.5: Depth of shower maximum measured by the Pierre Auger Observatory surface detector, compared to model predictions for protons and iron nuclei.

1.3.1 Magnetic fields

The deflection that cosmic rays experience is directly proportional to the magnetic field strength and the particle charge, and inversely proportional to the energy. The typical deflection can be estimated using [28]

$$d\theta(E,d) \propto Z \left(\frac{E}{10^{20}\,\mathrm{eV}}\right)^{-1} \frac{B}{10^{-9}\,\mathrm{G}} \frac{d}{\mathrm{Mpc}}$$

which gives that a proton of 100 EeV that travels through an nG magnetic field for 1 Mpc is deflected by 1 degree. It is also useful to estimate the confinement power of the magnetic field, given by the Larmor radius

$$r_L = 10\,\mathrm{kpc}\frac{E}{10^{17}\,\mathrm{eV}}\frac{1}{Z}\left(\frac{B}{10^{-6}\,\mathrm{G}}\right)^{-1}$$

Calculating the Larmor radius for different energies is essential to understanding which particles are confined inside sources or galactic environments and which escape into the outside universe. For example, galactic cosmic rays under the EeV are trapped in the galaxy disk, while above the threshold the Larmor radius becomes comparable with the size of the galaxy and the particles can escape. This sets a limit on the possibility of identifying the sources of Galactic CRs, but also the minimum energy of extragalactic CRs that have to escape from the galaxies that host their sources.

The Galactic magnetic field (GMF) has been only recently modeled in a quantitatively satisfying way. The main techniques employed in the determination of the GMF are the measurement of the Faraday effect in radio emissions [29] and the observation of polarized and unpolarized synchrotron emission by experiments such as WMAP [30] and Planck [31]. The Faraday effect is the rotation of the plane of polarization in radio emissions of different sources, proportional to the strength of the field in the direction of the emission; this gives information on the parallel component of the GMF. Galactic synchrotron emission gives instead information on the transverse component of the field.

Models trying to characterize the GMF exist, and the most used one is the Jansson-Farrar-2012 (JF12) model [32]. Below, an example of protons propagating in the JF12 model is displayed. Another model is the Psirkov-Tinyakov-2011 [33]. While useful for estimation of the magnetically induced delays in cosmic ray propagation, average deflections, and confinement, as seen in figure 1.6, GMF models are not yet reliable enough to give precise information on particular deflections and especially directions of deflections which would be of paramount usefulness in determining the sources of Galactic and extragalactic cosmic rays. It is also worth noting that the two models presented differ substantially in the prediction of deflections and delays.

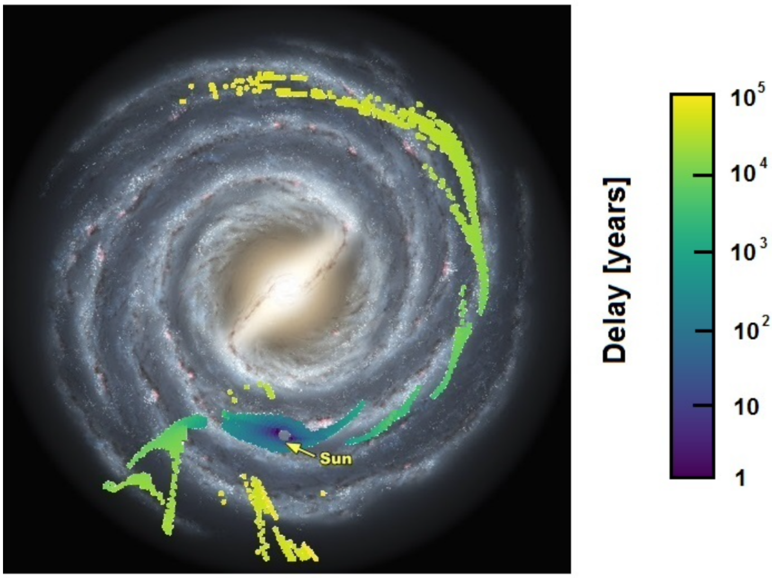

Figure 1.6: Deflection and delay experienced by protons of 1 EeV in the regular component of the GMF as in the JF12 model, superimposed on an artist's impression of our Galaxy. The colored dots represent the starting positions of CRs arriving at earth. Particles accelerated to 1 EeV in regions of the Galaxy without dots cannot reach the Earth in the span of 100000 years (the longest delay considered for this simulation).

The extragalactic magnetic fields (EGMFs) are investigated in similar ways to the Galactic ones, but their properties are much less well known. even if great advancements in their modeling have been made in the last decades; a good review of the available knowledge on the EGMF can be found in [34]. Upper limits are available, computed, for example, from diffuse radio emission [35], fast radio bursts [36], TeV blazar observations [37], and from UHECR anisotropy itself [38]. These observations agree to an upper limit in the average field strength of $\approx$ nG, up to $\approx$ 0.1 μG in filaments; inside galaxy clusters, the fields are thought to be larger, up to tens of μG

[39]. Even if the EGMF has a strength estimated to be smaller than the one of the GMF, its importance cannot be underestimated, as cosmic rays coming from other galaxies propagate inside it for tens or even hundreds of Mpc, amplifying the deflection magnitude.

1.3.2 Interactions with cosmic backgrounds

The background radiation permeates the cosmos, composed of photons with different origins and energies. The most famous kind of background radiation is probably the Cosmic Microwave Background (CMB), discovered by Arno Penzias and Robert Wilson in 1965 [1]; it is a relic black body radiation dating to the epoch of recombination, composed of photons with a density of about 411 particles/cm^3; the average energy of the CMB photons is $\approx 5 \times 10^{-4}$ eV [40]. Ultra-high energy particles that are propagating through space may interact with the CMB after a certain energy threshold depending on the processes involved. These interactions lower the cosmic ray energy and produce secondary particles. Greisen, Zatsepin, and Kuzmin in 1966 [2][3] independently theorized first the pion photoproduction from protons interacting with CMB photons, thus called the GZK effect:

$$p + \gamma_{CMB} \rightarrow \Delta^+ \rightarrow p + \pi^0$$
$$p + \gamma_{CMB} \rightarrow \Delta^+ \rightarrow n + \pi^+$$

The threshold energy for protons is:

$$E_{th} = \frac{m_\pi}{4E_\gamma}(2m_p + m_\pi) \approx 7 \times 10^{19}\,\text{eV for a photon with } E_\gamma = 1\,\text{meV}$$

it is important to remember that the CMB is a black body radiation and as such photons with higher energies exist, although with much lower density; interactions with these high energy tails require lower energy thresholds for the cosmic rays. Another important interaction is the Bethe-Heitler pair production:

$$p + \gamma_{CMB} \rightarrow p + e^+ + e^-$$

In this case, the threshold energy is lower than pion production, due to the lower mass of the electron-positron pair compared to the meson:

$$E_{th} = \frac{m_e(m_p + m_e)}{4E_\gamma}(2m_p + m_\pi) \approx 5 \times 10^{17}\,\mathrm{eV} \text{ for a photon with } E_\gamma = 1\,\mathrm{meV}$$

Heavy nuclei can also interact with the CMB via photodisintegration [41]:

$$A + \gamma_{CMB} \rightarrow (A-1) + N$$
$$A + \gamma_{CMB} \rightarrow (A-2) + 2N$$

the threshold energy for these processes increases with mass, and therefore heavier components survive longer compared to lighter ones. Heavy nuclei, just like protons, can also undergo pair production:

$$A + \gamma_{CMB} \rightarrow A + e^+ + e^-$$

while the GZK effect per se refers only to proton interactions, the term is often loosely used to embrace all of these effects occurring during UHECR propagation.

As previously stated UHECRs lose energy with every interaction. From the mean free path $\lambda = (n_\gamma \sigma)^{-1}$ (where n_γ is the CMB photon number density) and the average inelasticity (energy loss of the proton), one can compute the *energy loss length* i.e. the propagation length associated with an average energy loss of one order of magnitude for the primary CR. For pair production, the energy loss length is of the order of the Gpc, since protons lose on average ≈0.1% or less of their energy with each event, and heavier nuclei even less. In pion production for protons and photodisintegration for heavier nuclei the inelasticity factor is much higher, at ≈20%, and factoring in a mean free path of the order of Mpc to tens of Mpc, the energy loss length is of the order of 100 Mpc for protons and iron, and lower for intermediate nuclei. This implies a suppression of the cosmic ray flux at Earth at the highest energies, called *GZK cutoff*, and the definition of a local bubble of the universe, the *GZK horizon* or *bubble*, outside which sources cannot contribute significantly to the observed flux, as illustrated by figure 1.7.

Subdominant contributions to the energy loss due to interactions of protons and nuclei with other photon backgrounds, such as the Infrared Background Light (IBL) or the Cosmic Optical Background (COB), are also

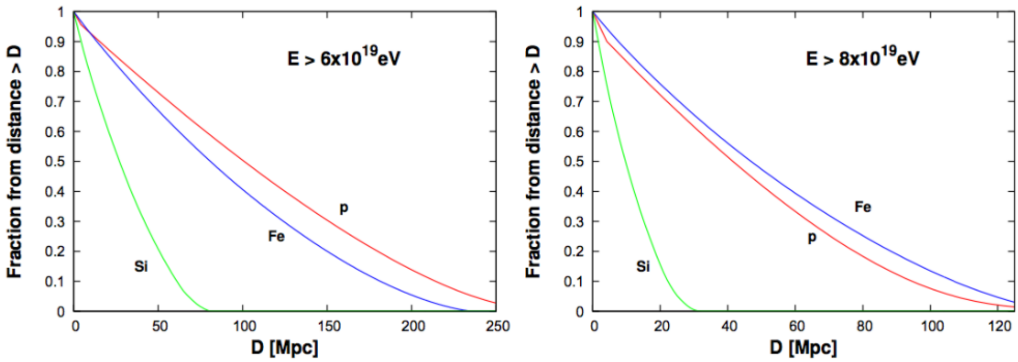

Figure 1.7: Fraction of CRs arriving at Earth with energy above 60 EeV (left) and 80 EeV (right) as a function of source distance D, for different species of primaries; from [42].

present. These contributions can generally be neglected due to the very low density of IBL and COB photons. The different shapes of the energy loss length with relation to the energy are shown in figures 1.8, 1.9.

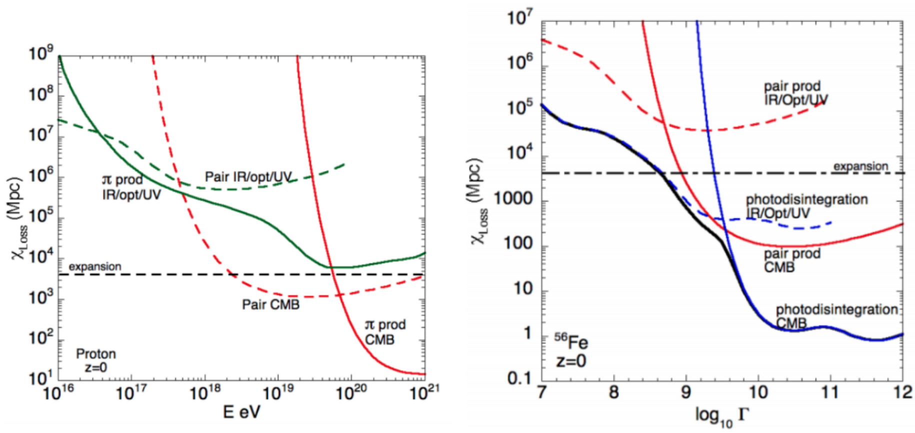

Figure 1.8: Evolution of the energy loss length for a UHE proton (left) and Iron (right) as a function of its energy. Left: pair production as the dashed curves, pion production as the continuous curves, interaction with the CMB in red and with other backgrounds in green. Right: interaction with the CMB as continuous curves, with other backgrounds as the dashed curves. In both plots, the adiabatic energy loss due to the universe expanding is also shown. From [43]

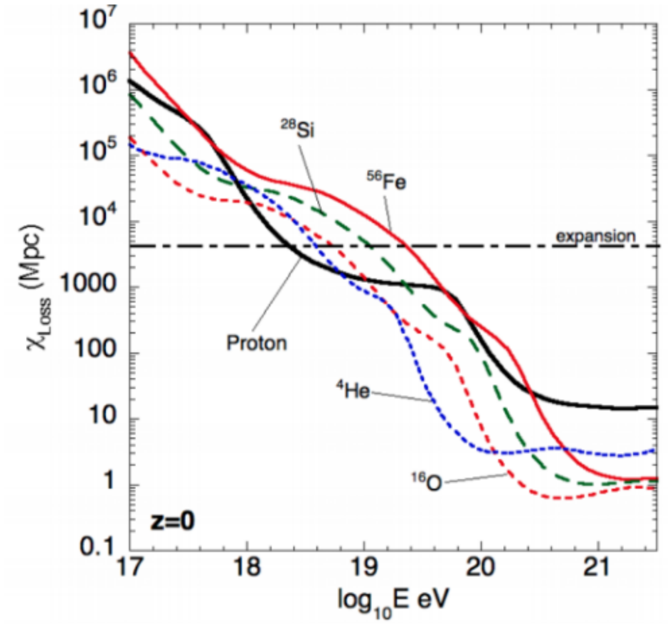

Figure 1.9: Comparison of the evolution of the attenuation length of different species at z=0. From [43]

Secondary particles

Many of the interactions between primary CRs and the background produce pions, both charged and neutral. These mesons decay shortly after, producing secondary emissions which are of astrophysical interest. In particular, charged pions decay states include neutrinos while neutral pions decay into two gamma rays. These are generally called *cosmogenic neutrinos and gamma rays* (or more colloquially *GZK* ν *and* γ). From an energetic point of view, these cosmogenic particles are expected to carry $\approx 5-10\%$ of the primary energy and are thus at the extreme tail compared to both astrophysical neutrinos and gamma rays.

Gamma rays, while having the advantage of not being deflected by magnetic fields, are much more absorbed than neutrinos; at the energies of interest, as visible in figure 1.10, the horizon is of the order of the Mpc; therefore GZK photons are not observable if not produced quite close to Earth [45], in cosmological terms. The Pierre Auger Observatory is conducting photon searches, without discriminating power between UHE *astrophysical* and *cos-*

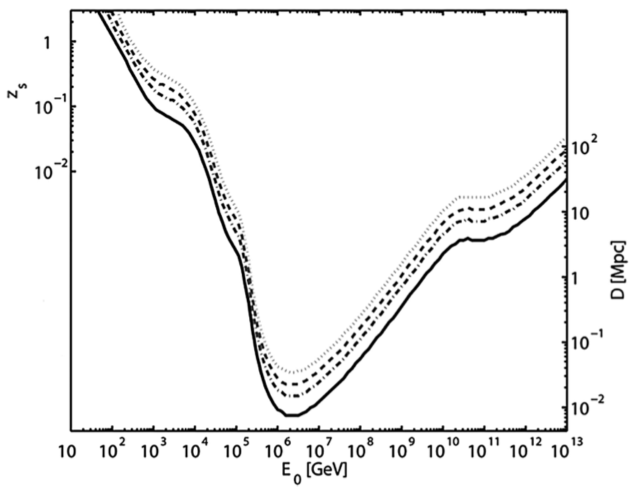

Figure 1.10: Source redshifts Z_s at which the optical depth takes fixed values as a function of the observed photon energy E_0; the y scale on the right side shows the distance in Mpc for nearby sources. The curves from bottom to top correspond to a photon survival probability of $e^{-1} = 0.37$ (the horizon), $e^{-2} = 0.14$, $e^{-3} = 0.05$ and $e^{-4.6} = 0.01$. For $D < 8$ kpc at any value of E_0 the photon survival probability is larger than 0.37. From [44].

mogenic γ-rays [46]. In principle, if the sources of UHECRs were identified, one could conduct a photon search in the direction of the sources to differentiate between the two classes of radiation.

On the other hand, neutrinos do not undergo any deflection or absorption process, and GZK νs produced in the far universe could be observed on Earth, still pointing to the original arrival direction of their primary particle. The detection - or non-detection - of cosmogenic neutrinos and gamma rays could also give fundamental information on the nature of the primaries, especially discriminating between proton-only scenarios and heavy-dominated ones, and the solidity of theoretical models of high-energy interactions [47]. Many current UHECR experiments, like Auger, search for cosmogenic neutrinos [48], and there are future ones, like GRAND [49], that will be optimized for UHE-neutrino searches.

1.4 Ultra high energy cosmic rays origin

Having described the spectrum and composition of cosmic rays at Earth, and having followed their trajectory back into space, it is time to ask probably the most thorny question still open in astroparticle physics, what are the objects so powerful in the universe, that are capable of accelerating particles to such extreme energies?

1.4.1 Arrival directions

The first approach to finding the sources of CRs, and the true experimentalist's one, is to look at their measured arrival directions. Due to the previously described magnetic deflections, one could expect that the CR flux appears generally isotropic on Earth for everything if not the highest energies. Indeed this is what is observed at least in the first order. In the energy region between 1 and 100 TeV, more precise observations suggest the presence of low-amplitude (of the order of $8 - 14 \times 10^{-4}$) large-scale anisotropies. This has been observed since the beginning of the arrival direction studies on CRs [50] and is confirmed by a plurality of experiments that probed this energy range during the years (Tibet ASγ [51], MILAGRO [52], IceTop [53], HAWC [54]). The more visible anisotropy feature is a dipolar structure with phase $\alpha = 40°$; significant large-scale ($\approx 60°$) and medium-scale ($10° - 30°$) signals have also been recently confirmed by IceTop and HAWC. The presence of these signals is not yet completely understood but can be used to better constrain source populations in the Galaxy and the deflection power of the Galactic magnetic fields.
In the energy range between 100 TeV and ≈ 1 EeV the anisotropy pattern changes losing all of its characteristic features. Results from KASCADE-Grande [55] and Auger-750m show non-significant dipole signals, but interestingly aligned phases pointing towards the Galactic center, hinting at a still-Galactic provenance of CRs in this energy bin.
At higher energy still, above the ankle, new structures come into prominence pointing to the transition to an extragalactic origin of the incoming flux. The Pierre Auger Observatory in particular reports the observation of a very significant dipolar feature above 8 EeV with phase direction away from the Galactic Center [56]. This dipole maintains its amplitude in higher energy bins, although losing significance due to lower statistics. At the

highest energies, in the toe region, anisotropy scales are typically smaller, and the two most prominent features are the so-called *TA hot-spot*, as seen by Telescope Array in the northern hemisphere, and the *Centaurus region warm-spot*, seen by Auger in the south, both of which have a scale of around 30°. This will be discussed in much more detail in chapter 5 of the thesis.

1.4.2 Cosmic ray acceleration

As sketched in the previous subsection, simply measuring the arrival directions of CRs does not give enough information to clearly identify their sources, and a more complex approach must be implemented to isolate candidate astrophysical objects. Firstly, it is important to understand the mechanisms in play inside astrophysical objects that can give way to extreme accelerations.

Particles are generally thought to be accelerated to the highest energies via a series of subsequent interactions while contained in the source region, through *diffusive acceleration*, rather than accelerated in one interaction, as a *one-shot mechanism*;. Thus, the most important ingredient in a cosmic accelerator is a strong magnetic field with a coherence length large enough to contain particles inside the source as they acquire energy, i.e. the condition $\frac{E_{max}}{ZcB} < L$; the larger the magnetic field, the smaller the object can be. The maximum energy reachable by a source can be obtained by rearranging the Larmor formula:

$$\left(\frac{E_{max}}{\text{EeV}}\right) \propto Z \left(\frac{B}{\mu\text{G}}\right) \left(\frac{R}{\text{kpc}}\right)$$

This implies that to accelerate particles to the highest energies, either extremely extended objects or extremely powerful magnetic fields are needed. The different classes of objects satisfying these conditions are customarily displayed in the *Hillas Plot* (figure 1.11), which shows their size L and magnetic field B over the lines which represent the characteristics necessary to accelerate protons or iron nuclei to 100 EeV; candidate sources of different classes have huge impacts on the characteristic of the spectrum and mass composition observed on earth, and observational data can support or disprove the contribution of certain classes of objects.

The most didactic model of particle acceleration in an astrophysical source is the so-called Fermi-I model, proposed in 1949 by Enrico Fermi

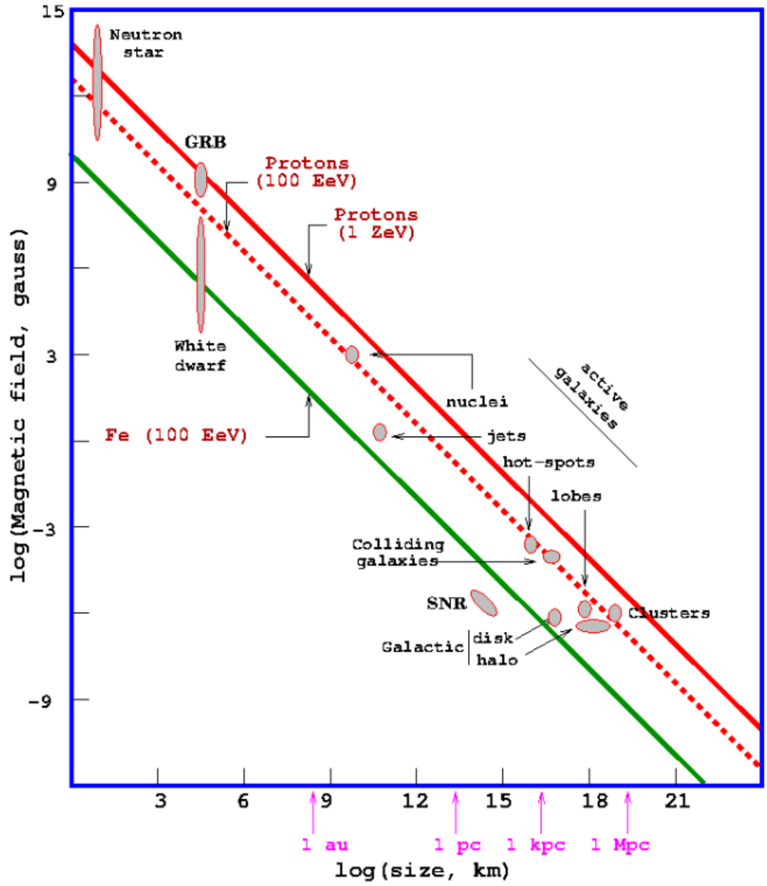

Figure 1.11: Hillas plot: the size of the objects on the x-axis, magnetic field on the y-axis, in log-log scale. The line shows the combination of parameters necessary to accelerate iron nuclei to 100 EeV (green), protons to 100 EeV (red dashed), and 1 ZeV (red). From [57].

[58]. Initially, Fermi theorized a mechanism to transfer energy from magnetized clouds to single particles; in this framework, particles are scattered by the irregularities in the magnetic field of the clouds, changing direction, and gaining or losing energy depending if the collision with the cloud is head-on or tail-on. In the end, the particles tend to gain energy due to a slightly higher probability of head-on collision. The energy gain is

$$\approx \Delta E/E_0 = \epsilon = 4/3\beta^2$$

where βc is the velocity of the cloud. Due to the quadratic dependency on the velocity, this model was named Fermi-II. The timescale of acceleration is:

$$t_{acc} = \frac{E}{(dE/dt)} \approx \frac{\Delta E}{E}\frac{c}{\lambda} = \frac{3\lambda}{4c}\frac{c^2}{V^2}$$

since the clouds are non relativistic, $(c/V)^2$ is >> 1, and the acceleration is quite slow.

If, however, these interactions take place in a *shock area*, the situation changes due to the higher velocity of the clouds, which become much faster than the magnetic irregularities and also faster than the typical velocity of magnetic perturbations in the Galaxy. In this case, the interactions can be considered at rest with the fluid both upstream and downstream, and as such all collisions can be thought of as head-on. The energy gain will be:

$$\approx \Delta E/E_0 = \epsilon = 4/3\beta$$

Under this linear dependence, the model is called Fermi-I.
This simple model is useful since it also reproduces the power-law shape of the spectrum of cosmic rays: after n collisions the particle will have energy:

$$E_n = E_0(1+\epsilon)^n$$

And the probability of escape at the n-th collision is

$$P_n = P(1-P)^n$$

Given N_0 particles at the start, the particles escaping with energy E_n will be

$$N_n = N_0 P_n = N_0 P(1-P)^n = N_0 P \left(\frac{E_n}{E_0}\right)^{\frac{ln(1-P)}{ln(1+\epsilon)}}$$

which translates to the differential spectrum of accelerated particles:

$$\frac{dN}{dE} \approx \frac{N_n}{(E_{n+1}-E_n)} = \frac{N_n}{\Delta E} \propto E^{-\gamma}$$

where, using reasonable values for P and ϵ, one gets $\gamma = 2$, which is consistent with observations when taking into account propagation effects.

Figure 1.12: Schematic representation of Fermi acceleration mechanisms. On the left is the Fermi-II, resembling a ball bouncing elastically on walls. On the right is the Fermi-I, showing the motion of the shockwave front.

The Fermi models (schematically shown in figure 1.12), even if very nice in simplicity and result reproduction, are not a comprehensive explanation of how cosmic rays are accelerated; they must be taken only as a first-order mechanism, or foundation upon which to build the effective models. For example, using these simple models one cannot explain the conditions that permit acceleration of particles up to 0.1 EeV inside supernovae remnants, of which there is evidence [59], corroborated also by the recent observations of Galactic Pevatrons by gamma observatories such as LHAASO [60]. Moreover, the "test particle" approach of the Fermi model, i.e. the accelerated particle has no impact on the energy balance of the source, is not compatible with real-world situations, in which a sizeable part of the kinetic energy released by the object is transformed in accelerated particles.
More complex and source-calibrated models are then needed to explain the acceleration in different astrophysical objects at different stages of their lives. Good theoretical models now exist for SNRs [61] and many other Galactic and extragalactic source candidates that will be introduced in the next section.

Candidate sources of UHECRs

Candidate sources of UHECRs comprise astrophysical objects that are very different from one another. Some are very compact objects (neutron stars), some are peculiar galaxies or galactic features (active galactic nuclei or AGNs, i.e. galaxies with the central black hole undergoing accretion, or starburst galaxies), and some are extreme transient events (GRBs). In the following, a list of proposed sources is reported.

- **Galaxy clusters**: as previously reported, magnetic fields with the strength of the μG or more are thought to permeate the intracluster space with coherence lengths of hundreds of kpc, which should be enough to accelerate CRs up to 100 EeV. However, the large distance that particles would need to travel increases the interaction with backgrounds, which should also be denser in the intracluster medium, lowering the maximum energy expected.

- **AGN accretion disks**: AGNs have been historically considered the most appealing candidates to accelerate UHECRs [57], because of their particularly extreme engines and their detection in the γ wavelengths. The simplest explanation for an AGN source of UHECRs would be that the particles are accelerated inside the accreting disk of matter orbiting closely around the central supermassive black hole of the galaxy (order of $10^6 - 10^{10}$ solar masses). The jets expelled from the black hole are $10^{-4} - 10^{-3}$ pc in size and could host magnetic fields of the order of the G [62]. However, the region close to the accretion disk is dense in both photon fields and high-energy particles. As such, it is not expected for UHE protons to survive and exit the region without interacting and losing energy, and heavier nuclei should photodisintegrate even more quickly. For this reason accretion disks of AGNs are now not expected to be significant contributors to the UHECR flux, especially if a heavy average mass composition is observed [39]. A schematic representation of different classes of AGNs can be found in figure 1.13.

- **Radio galaxy lobes**: certain kinds of radio-loud AGNs feature large lobes of plasma extending from the central black hole for hundreds of kpc, often exceeding the size of the host galaxy. The lobes are observed through radio synchrotron emission and can either dissipate in density with distance from the host or show high-density regions at their edge (*hot-spots*), with sizes of a few kpc. The host galaxies of the former type are called *Fanaroff-Riley type I* galaxies, of the latter *Fanaroff-Riley type II*; radio observations of these two types of galaxies are shown in figure 1.15 and a composite image of an FR-II galaxy is shown in figure 1.14. This difference in features is probably caused by the velocity of the plasma when expelled from the accretion region, either subsonic (FRI), or supersonic (FRII) [64]. In the lobes,

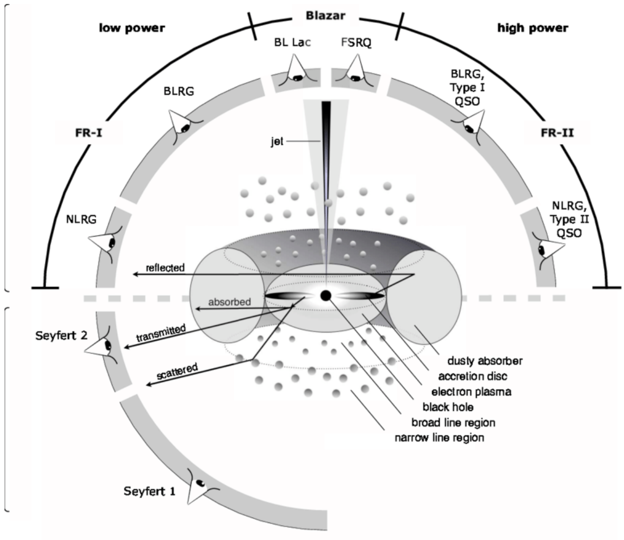

Figure 1.13: Schematic view of an AGN, showing features of different subclasses of objects. From [63].

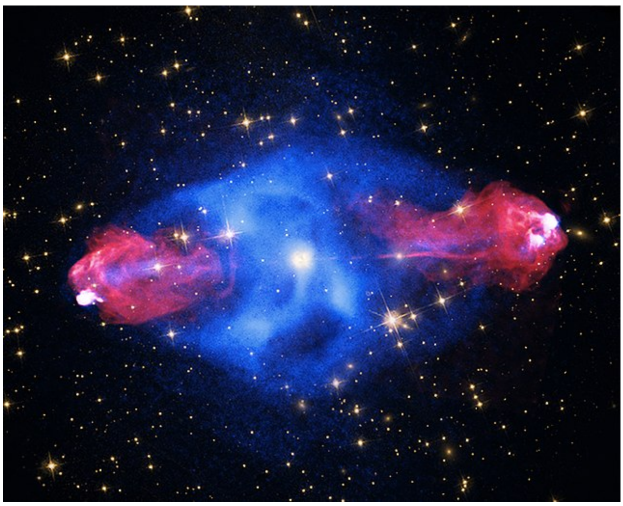

Figure 1.14: Cygnus A, a radio-active FR-II AGN showing extended radio emission in relativistic jets that protrude for more than 3×10^5 ly from the core with denser hot spots at the terminus. Radio observations are in red, and X-rays are in blue.

magnetic fields are less than a μG, while the hot spots in FRII objects are expected to feature fields up to hundreds of μG. Both the hotspots and the lobes in general are potential candidate sources of UHECRs. It is worth noting that when the lobes are pointing towards the Earth, the galaxy takes the name of *Blazar*. Blazars are the most commonly identified sources of extragalactic gamma rays known at the moment; as they are the same objects as Fanaroff-Riley, and more in general jetted, radiogalaxies, they are of course considered candidate hosts for UHECR acceleration.

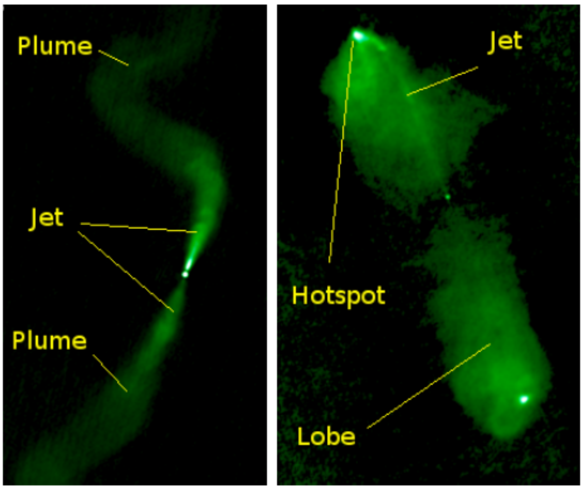

Figure 1.15: Fanaroff-Riley type I in the left panel (3C31), and type II in the right panel (3C98) in the radio band.

- **Starburst galaxies**: galaxies undergoing massive episodes of star formation are labelled as *starbursts* (such as the close-by galaxy M82 pictured in figure 1.17). Stellar winds from the multitude of hot stars and supernova explosions create extreme-temperature regions in the center of these galaxies as seen by the schematic representation in figure 1.16. The gas then expands adiabatically from the center into the halo, creating the so-called *superwind* [65]. These winds contain many temperature phases, with relativistic components. It is still debated if the superwinds alone can be responsible for the observed UHECR flux, although recent models propose that especially the terminal shock regions can accelerate CRs to the highest energies reproducing observed conditions [66]. It is also of importance the fact that starburst galaxies, as they show massively inflated star formation, should contain inside them a much higher concentration of peculiar compact objects also associated with possible UHECR acceleration.

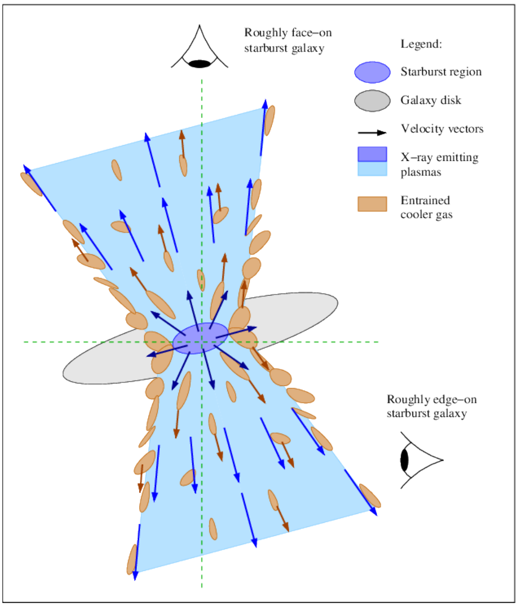

Figure 1.16: Schematic view of a starburst galaxy and its superwind. From [67].

Figure 1.17: The starburst galaxy M82, or *cigar galaxy*, in an image by the Hubble Space Telescope. Clearly visible are the starburst superwind filaments, in red.

- **Gamma ray bursts**: gamma-ray bursts (GRBs) are extremely energetic explosions in the γ wavelengths. They are generally classified based on their duration: short GRBs (< 1 s) have long been thought to originate when two binary neutron stars merge into a black hole, in an event also known as a *kilonova*. This has been recently confirmed by multimessenger observations with gamma rays and gravitational waves [68]. Long GRBs (1-2 s) have been associated with *hypernovae*, i.e. extreme core-collapse supernovae. Soft gamma repeaters (SGRs) were initially described as gamma-ray bursts, but are different kinds of events, associated with γ-emitting neutron stars, in particular, *magnetars*; this class of objects will be described in the next item. In general, GRBs are disfavored as the primary UHECR source because of their rarity in the local universe, as they were mostly observed at large redshifts, and the number of observations inside the GZK horizon is not enough to justify the UHECR flux according to models [69].

- **Compact objects**: neutron stars (such as the Crab pulsar shown in figure 1.18) are associated with the strongest magnetic fields in the known universe, of the order of $10^{10} - 10^{12}$ G, up to $10^{14} - 10^{16}$ G for the extreme cases known as *magnetars*. The maximum energy reached by the object is estimable as $E_{max} = \omega/cZB_sR^2$, where B_s is the magnetic field of the star, ω its spinning velocity, and R its radius. Using this estimation, magnetars should be able to sustain acceleration of UHECRs up to 100 EeV in their early stages [70]. Under 100 magnetars are known in our Galaxy, but none is currently accelerating particles to energies where they are not deflected enough by the GMF to be isotropized. A more accurate calculation of the density of these objects in the local universe is needed to understand if they alone are able to explain the majority of the UHECR flux.

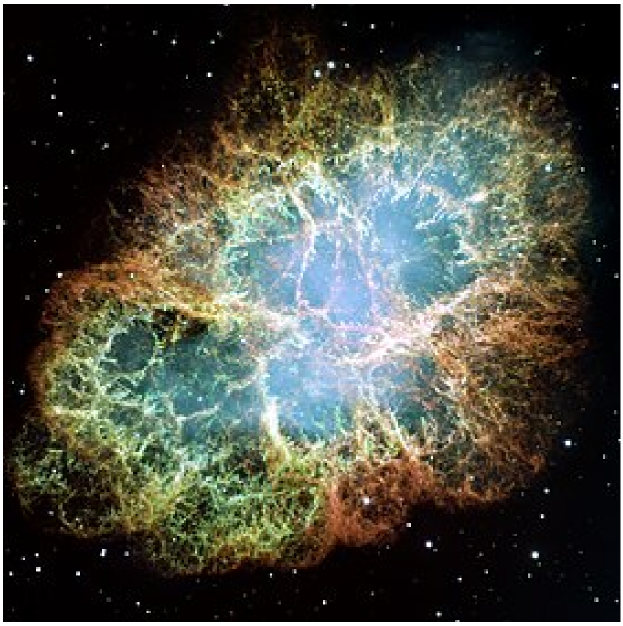

Figure 1.18: The Crab Nebula imaged by the Hubble Space Telescope. The Crab Nebula, discovered in 1731 and probably the most well-known gamma ray emitter in our Galaxy, is an expanding supernova remnant with a central pulsating neutron star. The remnant shows a blue-glowing core due to relativistic electrons moving around the magnetic field lines of the pulsar, and hydrogen filaments at its borders.

Chapter 2

Extensive air showers: science and detection

As mentioned in the previous chapter, it is not possible to perform direct detection for all energy ranges of cosmic rays, the main reason being the increasingly large effective area required to have usable statistics at higher energies due to the power-law shape of the flux. In particular, for particles with energy above the 100 TeV range, the flux is not strong enough to sustain direct detection in balloon- or space-based experiments. Cosmic ray detection has then to be indirect, i.e. made by sampling the secondary particles produced when the primary cosmic ray interacts with Earth's atmosphere. This cascade of secondary particles is called *Extensive air shower* (EAS).

In this chapter, I will present the current knowledge of extensive air shower physics and the different detection techniques used to detect it efficiently.

2.1 Extensive air showers

Extensive air showers are cascade productions of secondary particles stemming from the first interaction between the primary cosmic ray and a nucleus in the air. These cascades are sustained as long as the secondary particles have enough energy to produce a new generation in their next interactions. The majority of particles in the shower are photons, electrons, and positrons, which make up the *electromagnetic shower*, accounting for $\approx 99\%$ of the particles and $\approx 80 - 90\%$ of the total energy of the EAS. Muons carry about 10% of the energy. The rest of the particles are pions and baryons which compose the *hadronic shower*, and a component of neutrinos. The hadronic component is generally localized very close to the shower axis.

As an example, a 10 EeV proton can produce a shower of the order of 10^{10} particles, which spread on the ground for tens of kilometers. At the primary interaction point with the atmosphere, protons produce mainly pions and kaons, distributed between *charged* and *neutral* flavors. The charged particles lose energy via ionization until they decay in either pions (for kaons) or muons (both kaons and pions), generating the hadronic and muonic components of the shower. The neutral kaons decay mainly into two or three pions, with both a charged and neutral component. The neutral pions decay almost instantly into two photons, creating the electromagnetic shower. A schematic view can be found in figure 2.1.
The depth of the first interaction depends on the mass of the primary particle and its energy. The more energetic and lighter the particle, the deeper in the atmosphere it will interact.

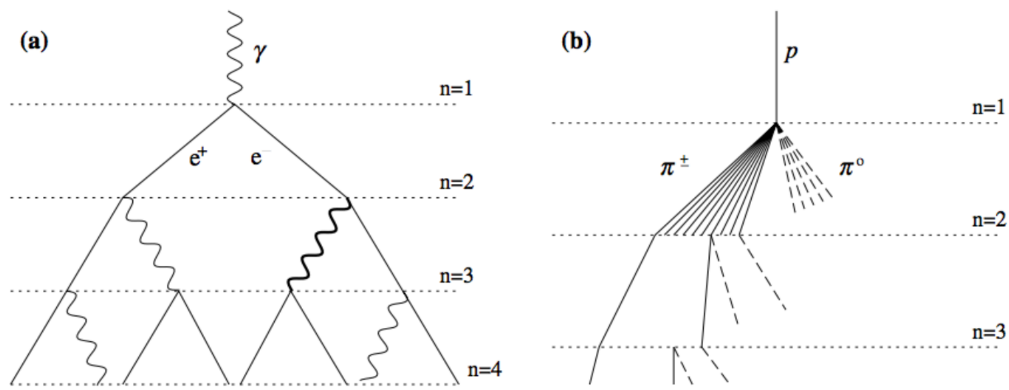

Figure 2.1: Schematic view of an electromagnetic (left) and hadronic (right) cascade (not to scale). In the left scheme, dashed lines are neutral pions that decay, and continuous lines are charged pions that interact sequentially.

2.1.1 Electromagnetic showers

The EM component is the most substantial component of the EAS, both in energy and in the number of particles. It is well described by the *Heitler model* [71], a toy cascade description as a perfect tree (figure 2.1).
The Heitler model divides the shower in equal *steps*, thanks to the fact that pair production for high energy photons and bremsstrahlung for high energy electrons have similar interaction length λ. Thus, at each step photons

produce an equi-energetic e^+e^- pair, while electrons lose half of their energy producing a γ by bremsstrahlung. The particles, losing energy, reach a lower energy threshold called *critical energy*, below which energy losses through collision start to dominate over pair production and bremsstrahlung ($E_c \approx 86$ MeV in air) and the number of particles starts decreasing. This point is called X_{max}.
After n interactions, the total number of particles is 2^n, each carrying $E_0/2^n$ where E_0 is the primary energy. After

$$n = \frac{\ln E_c/E_0}{\ln 2}$$

steps, $N_{max} = E_0/E_c$ particles will reach the critical energy at the depth

$$X_{max} = X_0 + \lambda(\ln E_0/E_c)$$

where X_0 is the electromagnetic radiation length, which for air is ≈ 37g/cm^2.
An important parameter of the shower is the *elongation rate*, which describes the change of the depth of the shower maximum with respect to the energy of the primary cosmic ray:

$$D = \ln 10 \frac{dX_{max}}{d\ln E_0}$$

which, substituting X_0 and λ, gives an elongation rate of 85 g/cm^2.
The lateral distribution of particles is dominated by the electromagnetic component's Coulomb scattering, and can be approximated as:

$$\rho(r) = k\left(\frac{r}{r_M}\right)^{-\alpha}\left(1 + \frac{r}{r_M}\right)^{-\eta-\alpha}$$

the Nishimura-Kamata-Greisen (NKG) formula, where r_M is the Moliere radius (approximately 80 m at sea level), and η and α are experimental parameters.

2.1.2 Hadronic showers

The hadronic component of EAS is approximated by the Heitler-Matthews model [72], an extension based on the electromagnetic shower model. The atmosphere is divided into layers of length $\ln 2\lambda_I$, where λ_I is the hadronic interaction length. At each step, hadronic interactions produce $2N_\pi$ charged pions and N_π neutral pions. Neutral pions decay immediately into photons, while charged pions interact further in the atmosphere until they reach a critical energy E_c^π ($\approx$ 20 GeV in air), below which they decay into muons and neutrinos. The critical energy is reached after

$$n_c = \frac{\ln E_0/E_c^\pi}{\ln 3N_\pi}$$

steps. If after reaching this energy ideally all charged pions decay into muons, the number of muons in the shower is

$$N_\mu = (2N_\pi)^{n_c} = \left(\frac{E_0}{E_c^\pi}\right)^\beta$$

where $\beta = \ln 2N_\pi \ln 3N_\pi$. The depth of the shower maximum estimation is similar to the electromagnetic component:

$$X_{max}^p = X_0 + \lambda(\ln E_0/3n_\pi E_c)$$

where n_π is the number of pions generated in the first interaction. This estimate is very approximated, as it only considers the first-generations pions. The elongation rate obtained from X_{max}^p is:

$$D = D_{em} + \frac{d}{d\log E_0}(X_0 - \lambda \ln 3n_\pi)$$

which yields $\approx$ 58 g/cm^2.
This model can be extended from protons to heavier nuclei via the *superposition model*, in which a nucleus with mass number A is simply viewed as A nucleons, each of energy E_0/A. Combining this approximation with the elongation rate leads to the fact that heavier elements interact higher in the atmosphere, which means pions will reach their critical energy sooner, leading to more muons being produced. In particular, the depth of the shower maximum is

$$X_{max}^A = X_{max}^p - \lambda \ln A$$

and the number of muons

$$N_\mu^A = N_\mu^p A^{1-\beta}$$

while the elongation rate is the same as for protons.
The average depth of shower maximum as a function of energy for different primary species and its fluctuations at fixed energy can be found in figure 2.2 and 2.3 respectively. Figure 2.4 also shows the average lateral profile for different secondary particles.

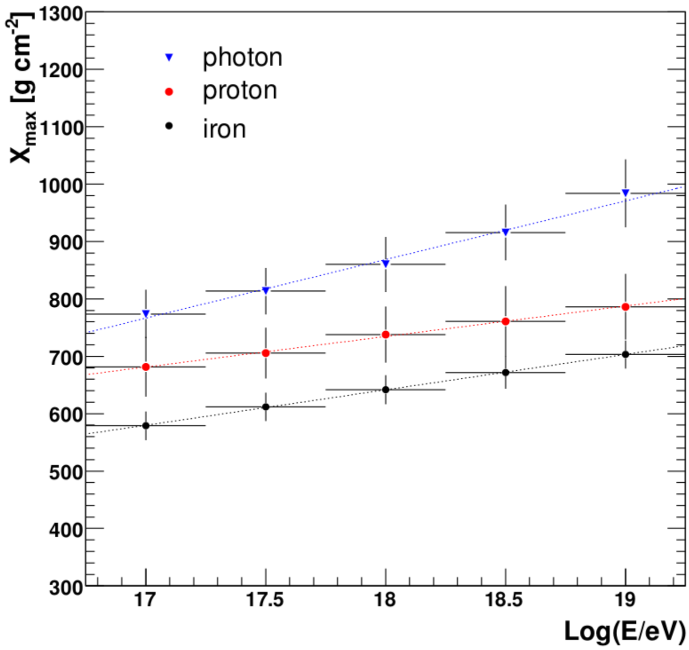

Figure 2.2: Behavior of the average depth of shower maximum as a function of energy for simulated protons, iron nuclei, and photons

2.2 Hadronic interaction models

Simplified shower models can give an estimate of the orders of magnitude of the parameters that characterize the EAS. To obtain more precise estimates, Monte-Carlo simulations are used. These simulations follow the shower development in the atmosphere, using phenomenological models based on accelerator particle physics and nuclear physics experiments, as well as theoretical EW and QCD models. The main problem of these models on which the MC simulations are based is the lack of measurements of interactions at the highest energies, which are not accessible in accelerators; for example, a cosmic ray at 10^{20} eV will experience a first interaction with a nucleus in the atmosphere at a center of mass energy of $\approx 3 \times 10^{16}$ eV, which is still orders of magnitude higher than energies available at the LHC or even in the next generation of proposed colliders.

The most used code to simulate EASs is CORSIKA (COsmic Ray SImulations for KAskade)[75], which can simulate full cascades from the first

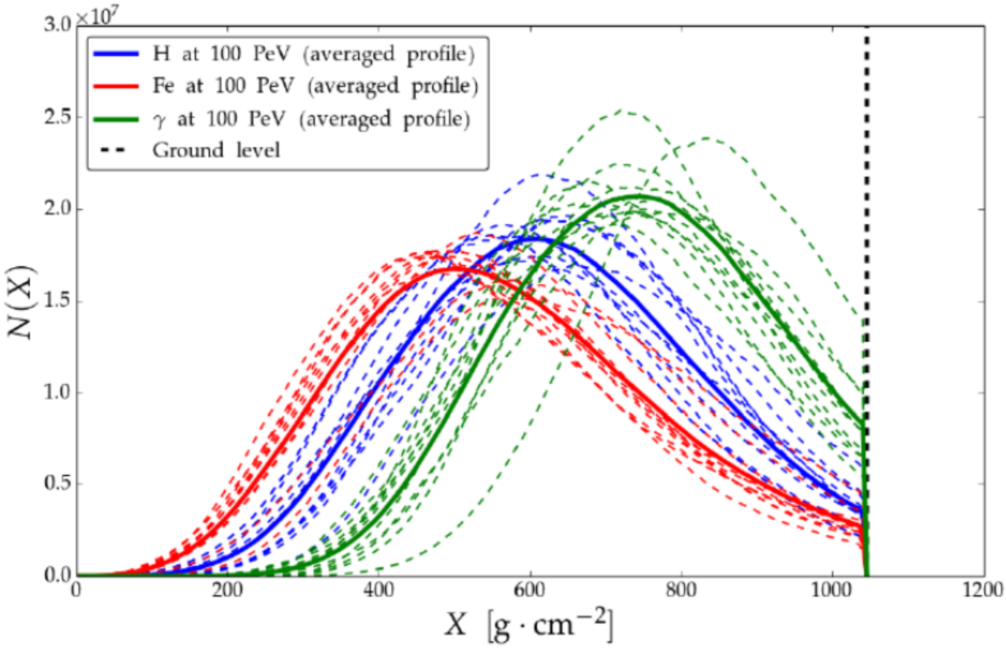

Figure 2.3: Average longitudinal profiles (solid lines), and single shower simulations (dashed lines), illustrating the shower-to-shower fluctuations and average behaviors of the particle density and X_{max} position as a function of X, for photons (green), protons (blue), iron nuclei (red) with the same primary energy of 10^{17}. From [73].

interaction to the detector or ground (a visualization of an example shower can be found in figure 2.5). CORSIKA is based on the Fortran programming language and is currently in its seventh iteration. CORSIKA8, a full rewrite of the code using C is in development and open beta version. Both low-energy and high-energy hadronic models are required to simulate the shower due to the extreme range of energies in play. Low energy interactions are generally simulated with a link from CORSIKA to the FLUKA [76] software; the GEISHA [77] and UrQMD [78] models are available natively. The high energy interactions can be described by several models alternatively: VENUS, DPMJET, and QGSJET [79] are models based on the Gribov-Rigge theory. EPOS-LHC [80], the most recent evolution of the EPOS framework, is based on a combination of the QGSJET and VENUS routines. SIBYLL, of which the most recent release is SIBYLL-2.3d [81], is based on the minijet model.

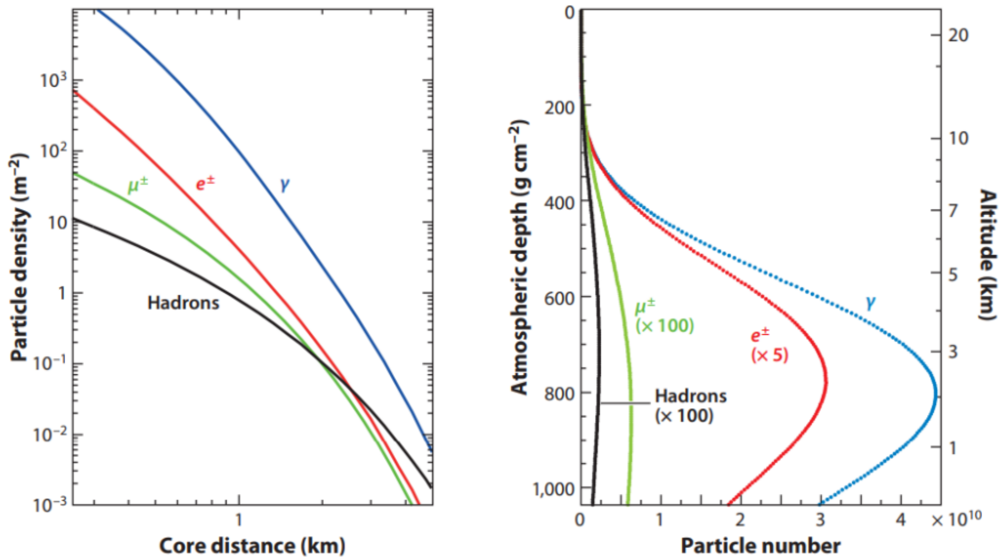

Figure 2.4: Average lateral (at the depth of the Pierre Auger observatory - left) and longitudinal (right) profiles for showers induced by a 10 EeV proton. From [74]

The most interesting parameters for all these models when simulating air shower development are the cross-section, the multiplicity of products, and the ratio of neutral to charged secondary particles. The LHC has been of paramount importance in constraining these parameters, and since its first run, the high-energy models have evolved and improved significantly in reproducing the conditions observed in ultra-high-energy showers. In figure 2.6 a comparison of pre-LHC and post-LHC models can be seen; the discrepancies in the modeled cross sections are evident, and as the increase in energy from pre-LHC to LHC-based models pointed out some errors and misextrapolation, in the same way, to correctly extrapolate these result up to the highest energies is an absolutely non-trivial task. In fact, none of the current high-energy hadronic interaction models reproduce correctly the observations of the current UHECR observatories; in particular, the X_{max} parameter and the number of muons in the shower are the two critical parameters for the mass of primary discrimination that are not consistent with simulations. These results will be presented more in detail in the next chapter, in section 3.10.2.

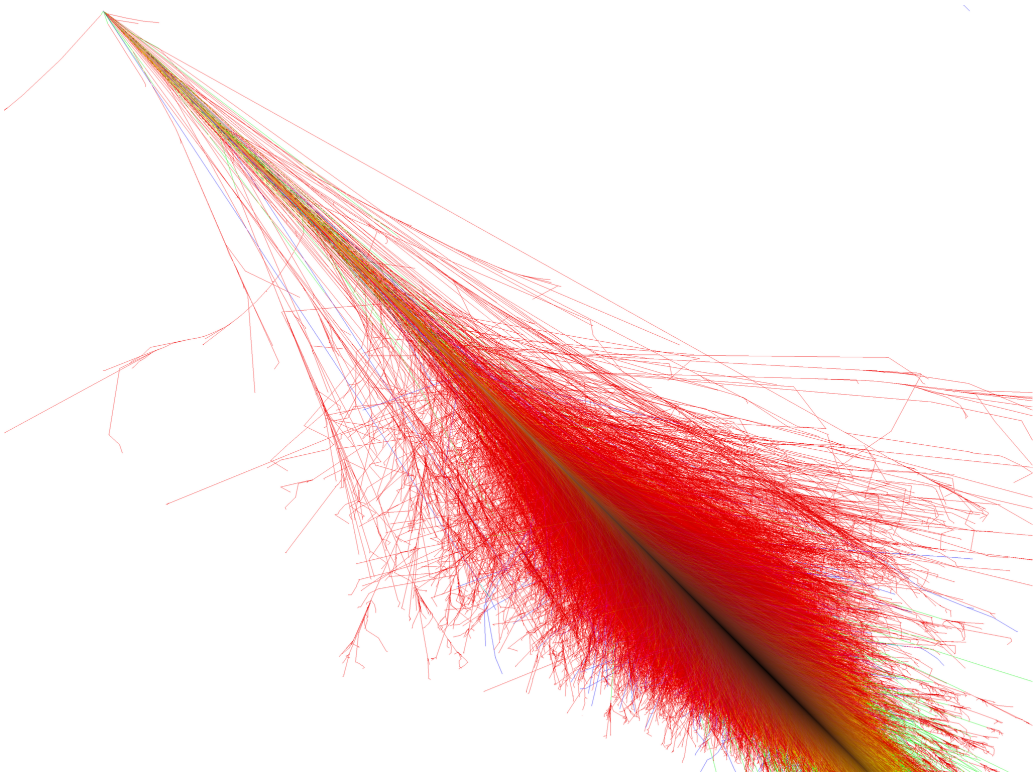

Figure 2.5: A shower example simulated with CORSIKA, a primary proton with energy 1 PeV, inclination 45 degrees. The electromagnetic component is in red, hadronic in blue, and muons are in green

2.3 Detection of extensive air showers

Extensive air showers can be detected during their development or once they reach the ground. Different techniques are suitable for different energy ranges and primary species. The main characteristics of the primary cosmic ray that have to be reconstructed from the shower are the mass, the arrival direction, and the energy. In the following, the main detection techniques are presented.

2.3.1 Arrays of particle detectors

The EAS can be detected once it reaches the ground by arrays of particle detectors sampling its front. This was the original technique used for the discovery of extensive air showers by Bruno Rossi and Pierre Auger, using

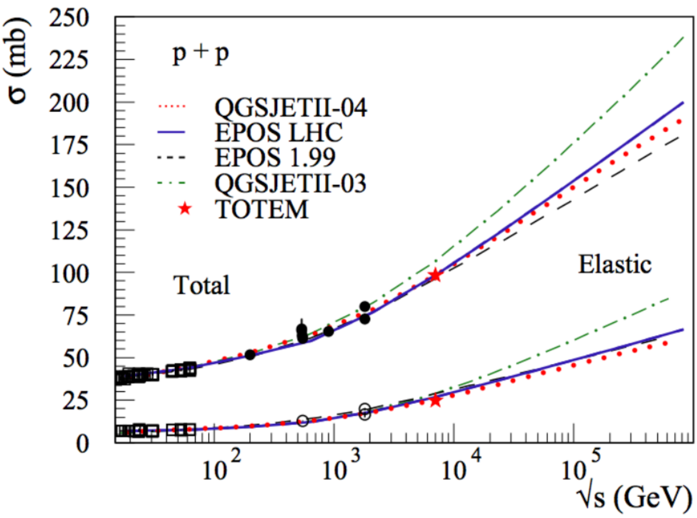

Figure 2.6: Cross sections calculated with various hadronic models before and after the data from LHC, superimposed with data from the TOTEM experiment at LHC and previous experiments.

Geiger-type counters as detectors.
The first array of particle detectors built for ultra-high energy cosmic rays detection was the Volcano Ranch experiment, composed of an 8 km^2 array of scintillators; this experiment detected the first 100 EeV-range cosmic rays [82]. In the 80s and 90s one of the two main UHECR-focused detector arrays was AGASA (Akeno Giant Air Shower Array) [83] in Japan, the other being the fluorescence-based Fly's Eye experiment in the USA. For the lower energy region, smaller arrays are used, such as EAS-TOP in Italy [84], KASCADE and KASCADE-GRANDE in Germany, and the current state-of-the-art experiment for the PeV range, LHAASO in China [85]. Detector arrays are also used for investigating the very high energy region of the gamma-ray spectrum, with experiments such as Milagro [86], HAWC [87], LHAASO and the future SWGO [88].

The two main types of detectors used to build the arrays are scintillators and water Cherenkov detectors.

- **Scintillators** were and still are used as main detectors in experiments such as AGASA, KASKADE, LHAASO, and Telescope Array, and as secondary detectors in the upgrade of the Auger Observatory, Auger-

Prime [89], for discrimination between the muonic and electromagnetic component of the shower; when shielded by an absorber material (iron, lead, the ground itself) scintillators can also be used for muon detection, for example as in the AMIGA extension of the Auger Observatory [46].

- **Water Cherenkov tanks** exploit the Cherenkov effect, i.e. the emission of light by charged particles faster than light in a medium, to detect the components of the EAS, and are sensitive to all components. Proposals for segmented tanks exist, to discriminate between electromagnetic radiation, which is blocked in the first layer or layers of the tank, and muonic component, more penetrating. WCDs are the main detector technique in the surface array of the Auger Observatory for UHECRs, as well as present in VHE gamma observatories such as HAWC, LHAASO, and the future SWGO.

The detector components of the array are distributed in the designated location with features that depend on the energy of cosmic rays that are the detection targets.

- **The altitude of the array**: in order to reconstruct efficiently the characteristics of the primary cosmic ray from the shower, the closer the array is to the shower maximum the better, as more particles are available for detection. As shown previously, the depth of the shower maximum increases with the primary energy; for UHECRs the ideal altitudes are between 1000 and 1500 m, while VHE gamma observatories such as HAWC and LHAASO are situated at over 4000 m of altitude.

- **The surface size of the array**: due to the shape of the spectrum of cosmic rays, at lower energies, smaller arrays are sufficient to have satisfactory detection statistics, while at the highest energies, a much larger array is needed due to the very low flux of less than 1 particle per km^2 per century. For example, in the knee region (PeV), tens or hundreds of thousands of km^2 are enough, while at the ankle thousands of km^2 are necessary. The surface of the array determines the maximum energy accessible by the observatories in a reasonable time.

- **The spacing of the array**: arrays optimized for the highest energies, which as said are enormous, are sparse, with spacings of 1 km or more between stations, mostly because of costs and practicality. Arrays for lower energies are more densely packed with detectors to efficiently capture the particles of the smaller and more compact showers. The spacing of the array determines the lower threshold energy accessible by the detector.

The arrival direction of the primary CR is measured based on the time-of-arrival difference of the particles of the EAS in the different detection stations. The shower axis, and hence the direction, can be reconstructed through a fit of the time distribution in the array. The resolution on the arrival direction is then strictly linked to the time resolution of the detectors. A more detailed report of the arrival direction reconstruction at the Pierre Auger Observatory ground array can be found in section 3.5.1.

The energy of the primary is estimated from an optimized signal at a certain distance from the core. The energy estimator is obtained as a fit parameter of the lateral distribution function (LDF) i.e. the signal in the detectors as a function of the distance from the shower core, and as such depends on the array spacing. The estimator is then correlated to the primary energy via Monte-Carlo simulations or with comparisons to different detectors (for example as done in the Pierre Auger Observatory, as detailed in section 3.5.3 of this thesis, or in Telescope Array).

The mass is much more difficult to reconstruct in ground arrays. Only mass-related variables, such as the number of muons, the shower shape or the depth of the shower maximum are measurable. The mass can then be inferred for statistical ensembles of data.

2.3.2 Cherenkov telescopes

Sufficiently energetic charged secondary particles in the EAS emit Cherenkov radiation in a very short flash of 5-20 ns. This Cherenkov flash is very faint, and can only be seen during dark nights with good atmospheric conditions. As the flash is directed very close to the shower axis, the detector must be near the EAS core.

The detector, which takes the name of Imaging Air Cherenkov Telescope, or IACT, is composed of a large mirror that reflects and focuses the photons into an array of photomultiplier tubes. Since the HEGRA experiment, which was operated between 1987 and 2002, most Cherenkov observatories are stereoscopic, i.e. they operate more than one telescope for better detection efficiency and discrimination between massive cosmic rays and high energy gamma rays, obtained thanks to the characteristic shapes of the different EASs.

Cherenkov telescopes can measure the longitudinal development of the shower, with direct measurement of the depth of shower maximum and calorimetric energy. As the atmospheric conditions influence the accuracy of the instruments, good monitoring of the atmosphere is necessary.

This technique is used in the TUNKA experiment [27] for cosmic rays and gamma rays above the ankle, but it is mostly employed in gamma-ray observatories specialized in the GeV-TeV range, like HEGRA, MAGIC [90], HESS [91][92] and as a secondary enhancement, LHAASO. CTA [93] will be a large array of IACTs of different sizes specialized for different energy ranges, with two sites, one in the Canary islands and one in Chile; it is currently under construction.

2.3.3 Fluorescence telescopes

As they travel through the atmosphere, particles in the shower excite nitrogen atoms. These then decay in their ground state, emitting fluorescence light. The light yield is about 4-5 photons per electron per meter at ground pressure; this means that only the highest energy events can produce enough light to be detected. Through a telescope of aperture ≈ 1 m^2, with photomultipliers as sensors, a shower is visible as far away as 20 km from the shower axis.

As for Cherenkov telescopes, fluorescence telescopes detect the longitudinal profile of the shower and have good capabilities for measuring directly the primary energy, depth of shower maximum, and arrival direction; similarly, the signal is very faint and needs dark nights and good atmospheric conditions to be efficiently detected. However, unlike Cherenkov light, which is highly beamed, fluorescence light is an isotropic emission.

The first fully functional fluorescence telescope for UHECRs was Fly's Eye, which operated in Utah between 1981 and 1993, and between 1993 and 2006 in the updated version, HiRes [94]. It is now used in both the Telescope Array and the Pierre Auger Observatory.

2.3.4 Radio arrays

Radio emission from cosmic ray air showers was measured at first in the 1960s, but the technique has caught on, especially in more recent times. This emission comes from different contributions [95]:

- The main contribution is from *geomagnetic origin*; it can be understood as arising from the time-varying transverse current which is a consequence of the acceleration-deceleration that electrons and positrons experience in the Earth's magnetic field while interacting with atmospheric molecules. The number of charges varies during the EAS evolution, creating the time variation.

- The second contribution is from the time variation of the total charge of the shower itself. The emission is linearly polarized with electric field vectors oriented radially with respect to the shower axis. It is also time-varying because of the change in the number of charges in the shower. This contribution is also called *Askaryan effect*, as it was proposed as the main emission mechanism by Askaryan in 1962.

- Tertiary mechanisms add small contributions, such as the *geosynchrotron* emission, atmospheric electric fields, transition radiations from the impact of electrons and ions with the ground, etc.

Arrays of radio antennas are suitable for detecting CR showers with energies above 10^{16} eV. The radio signal is coherent, i.e. scaling with the number of particles in the shower and thus the primary energy, at least up to 100 MHz. The signal also scales with the distance from the shower axis, which can be reconstructed with an exponential lateral distribution function (LDF). One of the main advantages of arrays of radio antennas as cosmic ray detectors is the possibility of employing a smaller number of very simple stations, keeping the cost low while opening the possibility of covering an extremely large area.

The first generation of radio arrays, which operated in the 2000s was CODALEMA [96], in France, and LOPES [97], at the KASKADE-Grande site in Germany. In both cases, the main obstacle was the extreme difficulty in self-triggering the radio array, which had to be supported by a different detection technique (particle detectors for CODALEMA, the entire KASKADE array for LOPES). These experiments were followed by a second generation mainly consisting of Tunka-Rex [98], which operates at the Tunka-TAIGA site, AERA [99], a sparse radio array of 150 antennas complementary to the Auger Observatory, and LOFAR [100], a dense purpose-built radio array, whose main goal is radio astronomy but also has cosmic ray detection capabilities. In the near future AERA will be expanded, with a radio antenna on the top of every Auger Cherenkov station; the Square Kilometer Array (SKA) [101] will be built in South Africa, with, similarly to LOFAR, mainly radio astronomy as a goal, but also strong EAS detection capabilities; another proposed radio experiment for astroparticle physics is GRAND [49], an extremely large array of radio antennas with many sites in the world, designed to detect mainly UHE-neutrinos interacting in the mountains, but also UHECR showers.

2.3.5 Other detection techniques

Other methods for detecting secondary cosmic rays in extensive air showers have been used historically. Wilson cloud chambers were invented in the early 1900s by Charles Wilson and have been used extensively in decades past especially to detect muons in EASs. Bubble chambers and spark chambers were also used [102], especially in the 1950s and 60s. These techniques have largely been supplanted by more modern detectors, but are still in use for demonstration purposes.

Neutrinos are present in the showers, produced by the decay of pions, kaons, and muons. The particles in the neutrinic component of the EAS are commonly known as *atmospheric neutrinos*. Detecting them, as any other neutrino, is incredibly hard. Atmospheric neutrinos are however one of the main backgrounds for astrophysical neutrino observatories. Three of these observatories are currently active: IceCube at the South Pole [103], KM3NET in the Mediterranean [104], and Baikal-GVD in Siberia [105]. Recently, the ANTARES observatory was dismantled [106], after being operated in one of the sites composing KM3NET. All of these experiments use the same detection principle, in which neutrinos passing through the earth interact with the medium they are crossing, producing charged leptons that, if energetic enough, emit Cherenkov light; this Cherenkov light is then collected by a series of photomultiplier tubes disseminated in the medium. IceCube uses polar ice as a medium, while KM3NET, ANTARES, and Baikal-GVD use water.

A completely different framework for the detection of particles of astrophysical origin consists of investigating the effect of these messengers on natural materials rather than building an artificial detector. This is the principle behind the Paleo-Detectors, a class of natural minerals which could contain traces of the history of astroparticle physics in the form of track defects of their crystalline structure. These minerals are currently proposed to be used for studies on beyond-the-standard-model physics, such as WIMP Dark Matter [107], or rare events, such as past supernova neutrinos [108]. A more complete description of this technique and a proposal for application in UHECR physics will be given in chapter 6 of this thesis.

2.3.6 Hybrid arrays

A lot of modern experiments that detect extensive air showers are of hybrid construction, i.e. they are composed of more than one class of detectors. Observing the same showers with two or more methods allows for cross-calibration and reduction in systematics. For example, a high-accuracy detector with a low duty cycle such as a set of fluorescence telescopes can be coupled with an array of particle detectors, less precise in reconstructing the shower characteristics but with a duty cycle of almost 100%.

Examples of hybrid detectors are: IceCube-IceTop, which combines strings of photomultiplier tubes (PMT) domes detecting the Cherenkov light emitted by leptons produced by neutrino interaction with an array of particle detection on top of the ice for muon tagging; the Telescope Array, in Utah, USA, comprised of an 800 km^2 array of scintillators as a surface detector, overlooked by 3 fluorescence telescope stations; the Pierre Auger Observatory, in Argentina, is the largest hybrid observatory, and UHECR detection experiment in general, as it covers 3000 km^2 with its surface detector composed of Cherenkov tanks, in addition to 4 fluorescence telescope sites. The Pierre Auger Observatory and its science will be described in more detail in the next chapter of the thesis.

Chapter 3

The Pierre Auger Observatory

The Pierre Auger Observatory [109] is the largest cosmic ray experiment ever built. It was conceived and optimized to measure extensive air showers induced by cosmic rays of energy above $\approx$1 EeV. The observatory is named after Pierre Auger, one of the pioneers of extensive air shower observations. The observatory is the first facility used to perform hybrid observations of air showers induced by ultra-high energy cosmic rays.

The Observatory is located in Argentina, near the town of Malargue in the province of Mendoza at an altitude of around 1400 m above sea level, and it covers 3000 km^2 of the local *pampa*, as seen in the map in figure 3.1. It started taking data in 2004 with 154 surface detectors and was completed in 2008 reaching 1600 Cherenkov station. 24 fluorescence telescopes in 4 sites complement the surface array, observing the development of the shower on dark nights. The surface array presents an enhancement region, called Infill, with half the normal grid spacing for detecting lower energy showers. The Infill is overlooked by the high-elevation telescope HEAT for hybrid calibration. It also contains buried muon detectors near a subsample of the stations. The Infill and muon detectors make up the AMIGA enhancement. A sparse array of radio antennas, AERA, is deployed amongst the surface detector. The Observatory is currently in the final phases of deployment of its upgrade, called AugerPrime.

In this chapter, the key technical characteristics of the observatory and its upgrade, along with some of the outstanding results obtained in over 15 years of operation will be presented.

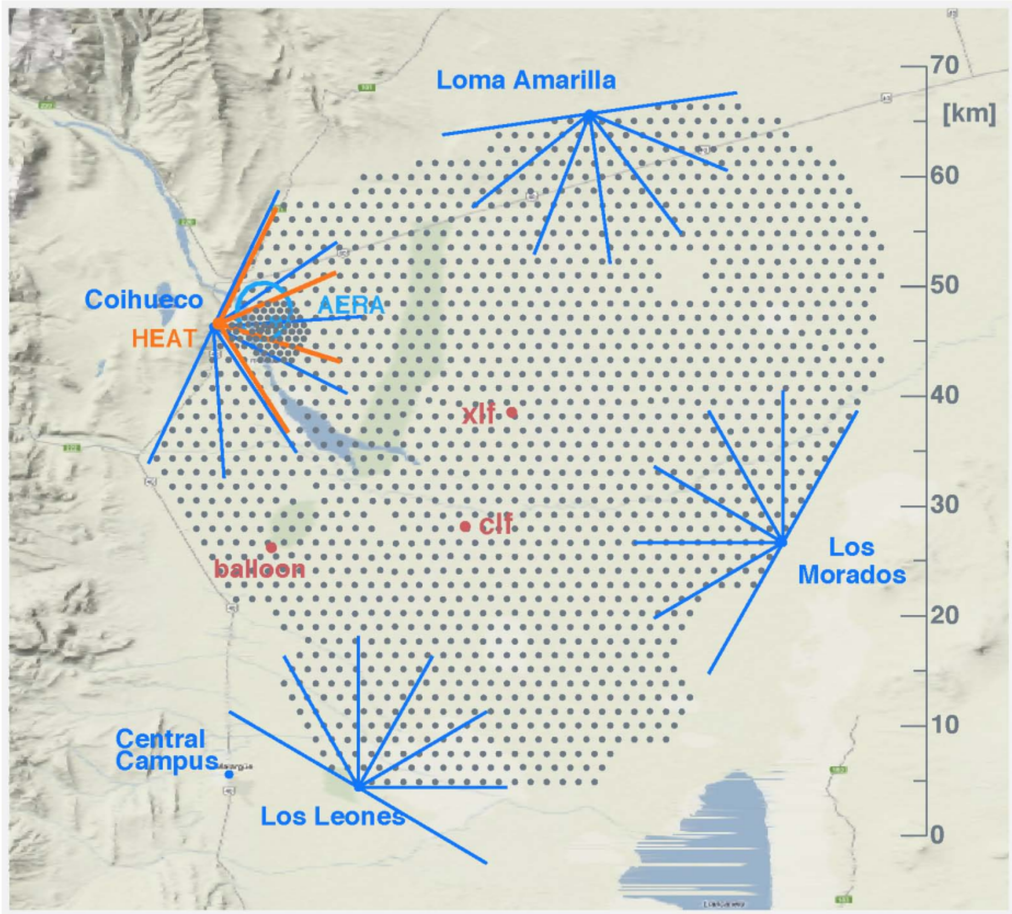

Figure 3.1: Map of the Pierre Auger Observatory. Surface detector stations are in black. The field of view of the fluorescence telescopes is represented by blue lines. Enhancements such as AERA, HEAT, and AMIGA are highlighted (see text for definition).

3.1 The site

The elevation of the site is a very important parameter to optimize when characterizing a cosmic ray observatory. The Auger Observatory site was chosen to be high enough (above 500 m a.s.l.) so that the shower maximum can be observed by the fluorescence telescopes, but low enough (below 1500 m a.s.l.) so that the shower maximum is still above the ground. As observatories for UHECRs need to be extremely large in size to have sufficient statistics due to the very low flux, the site must be flat enough to host a very extensive surface detector without considerable altitude changes, to ease deployment, communications, and response control. The chosen site in Malargue was one of the few in the world that satisfied all the necessary conditions, with other possibilities in Argentina, Australia, and South Africa. The initial proposal also foresaw a northern site, which was to be built in Colorado, USA, but was not followed through due to lack of funding. Most of the main facilities of the Observatories are hosted in the town of Malargue, such as the Central Data Acquisition System (CDAS), an assembly hall, laboratories for the detector parts, and the office building for local staff.

3.2 The Surface Detector

The surface detector (SD) is composed of 1600 water Cherenkov detectors (WCD) disposed on an equilateral triangular grid spaced by 1500 m. The resulting array spans 3000 km ^{2}. The SD has a duty cycle of almost 100% and is fully efficient for showers induced by cosmic rays with energy above $\approx 3 \times 10^{18}$ eV. Part of the SD is filled with 60 more stations, deployed between 2008 and 2010, creating a sub-array spaced by 750 m which can detect vents with full efficiency with energy above 3×10^{17} eV. This addition to the SD, called the *Infill array*, as presented before, is part of the AMIGA enhancement.

Each WCD (as seen in figure 3.2) is composed of a cylindrical polyethylene tank with a diameter of 3.6 m and a height of 1.55 m, filled with 12 tons of ultrapure water; three 9-inch PMTs overlook the water. The walls of the WCD are lined with a plastic material that contains the water, reflects and diffuses the light produced in the water, and provides light a path to the PMTs; in this way, the PMTs can be swapped without exposing or changing the water. Each part of the WCD was designed to survive at least 20 years; the water purification, which prevents the proliferation of micro-organisms, was an additional step to insure the long-term stability of the detectors and reduce the Cherenkov light absorption.

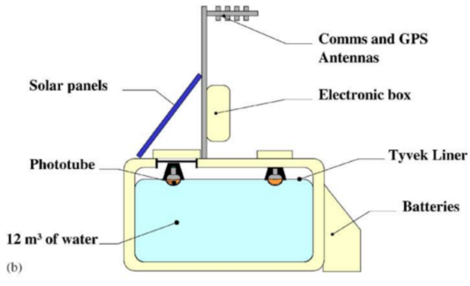

Figure 3.2: Schematic cross-section view of an SD station

3.2.1 PMTs and signal

Three PMTs look downward in the water from clear windows in the polyethylene, placed 1.2 m from the tank center in a triangular shape. From each of the three PMTs in the WCD, two signals are taken: one directly from the anode and one from the last dynode, amplified by a factor 32 and inverted. The dynode signal is called "high gain", while the anode signal, "low gain", is used when the former is saturated. The six signals are processed with a frequency of 40 MHz by flash analog to digital converters (FADC). The signals, once digitized, are sent to a logic device board that implements the station-level triggers, called T1 and T2, which will be discussed in more detail later. The signals are time-stamped thanks to a commercial Motorola GPS unit with an accuracy of 8 ns, a precision reachable also due to the high accuracy in the measurement of the tank position during deployment. A wide range of monitoring and diagnostic information is also collected from the stations. The power required for each WCD to function is provided by a solar panel, providing 10 W, located on top of the tank; the energy collected by the solar panels is stored in on-site acid batteries. This way, each station is fully autonomous, with no wired communication or power line.

3.2.2 Data acquisition and monitoring

The SD stations communicate via radio with the fluorescence detector (FD) sites using a Local Area Network (LAN). The FD buildings are linked to the central campus using a primary radio network that operates in the microwaves. The data is all sent to the CDAS, which collects the station-side triggers, performs the off-station triggers, checks for coincidences in the FD and SD collected data ("hybrids"), analyzes the monitoring and diagnostic information, and stores the data. The CDAS is designed to be almost fully autonomous and runs continuously on six server machines.

Local staff regularly performs maintenance on the SD. A comprehensive monitoring system constantly runs through all the diagnostic data collected by the stations. When a part shows malfunctioning, a team is sent to check and, if necessary, substitute the part. PMTs, for example, when substituted, are brought back to the central campus for repairing and reusing. In this way, less than 1% of the stations are inactive on average.

3.3 Exposure of the Surface Detector

The SD is fully efficient above 3×10^{18} eV; this means that every cosmic ray with energy above this threshold will trigger the array. The threshold was determined using hybrid events and Monte-Carlo simulations. Above this threshold, the effective aperture is equivalent to the geometrical one, integrated over the solid angle. Thanks to the simple array shape, the geometrical aperture is a sum of the apertures of all active hexagons composed of a central station and the 6 surrounding active stations, known collectively as *elementary cell* (figure 3.3). As all the hexagons are of equal area, the total aperture is simply *area of a cell*$\times$*number of active cells*. As the detection area per cell is 1.95 km^2, the corresponding aperture is 4.59 km^2 sr. The number of cells (or colloquially *hexagons*) that are active is monitored second by second with an error of $\approx$ 1.5%. To obtain the cumulative exposure at a certain moment, the geometrical exposure, which directly depends on the number of active cells as a function of time, is integrated over the number of elapsed seconds. Combining the uncertainties, the total error on the exposure is $\approx$ 3%.

3.4 SD data acquisition

Most of the particles reaching the SD are muons, low-energy photons, and electrons; these particles come from lower-energy cosmic ray showers, which are mostly extinguished in the higher atmosphere but have a much higher

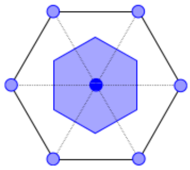

Figure 3.3: Scheme of an elementary cell, with its effective area of 1.95 km^2 shaded in blue

rate than EAS generated at the energies of interest for Auger. To differentiate this background from the particles of high-energy showers, a set of conditions has been set in place, consisting of a five-tier trigger system. The first two are applied at the station level, the third at the array level, and the last two are applied offline on recorded data. A summary chart of the first three triggers is visible in figure 3.5.

3.4.1 The Vertical Equivalent Muon

The stations need to be calibrated with a common source to account for possible variations due to atmospheric and detector effects. The chosen unit is the signal produced by a vertical central through-going muon (*Vertical equivalent muon* or VEM). This reference signal is extracted by the distributions of charge deposit and pulse height of omnidirectional atmospheric muons, due to the fact that the peaks of these distributions are proportional to the charged deposit of a VEM and its pulse height, respectively Q_{VEM} and I_{VEM}. To be more precise a value $Q_{VEM} = (0.96 \pm 0.03) Q_{VEM}^{peak}$ has been measured, thanks to dedicated scintillators above and under some tanks to select the muons. An example of these distributions is shown in figure 3.4. The CDAS stores the collected charge information in histograms, and for each triggered station the software checks the distribution of the signal deposited by crossing atmospheric muons in the minute before the trigger.

The algorithm converting the signal from the PMTs to VEM units starts by subtracting a baseline value in the dynode trace or, if this trace is saturated, in the anode one. The signals from the three PMTs are then merged into one, and the merged trace is used to determine the starting time of the event; the trace is converted into VEM, with a Poissonian error on the signal value, $\sqrt{S}$. In the eventuality of the saturation of the anode channel,

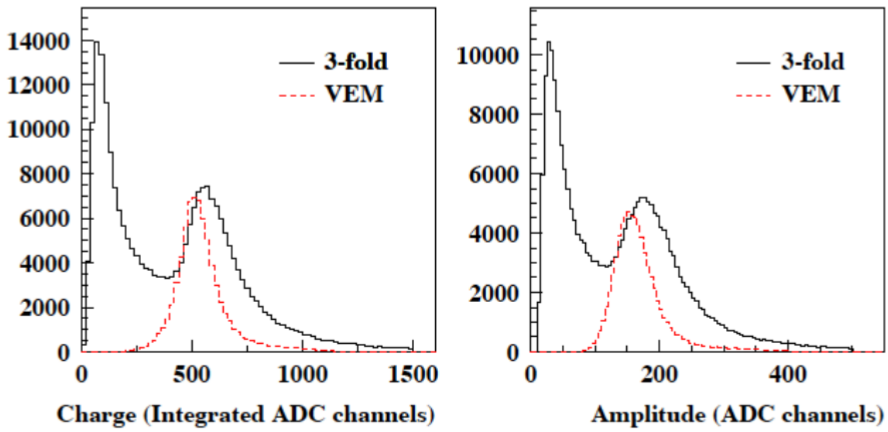

Figure 3.4: Distirbution of the charge (left) and amplitude (right) measured by the tanks (black line) and the charge and amplitude for vertical muons measured by scintillators (red line).

a recovery procedure based on the undershoot in the channels after the end of the trace is used.

3.4.2 Station and array triggers: T1, T2 and T3

The event selection and reconstruction chain starts with two triggers at the station level, i.e. that take into account the signal in the PMTs of each station, called T1 and T2, and one trigger at the array level, T3.

The T1 trigger

The first trigger, T1, is the trigger that decides if the traces of the three PMTs are to be stored in memory. It consists of two alternative conditions:

- Th-T1 is a simple threshold condition that requires that all 3 PMTs register a signal above 1.75 VEM. In the case of only two or one active PMTs in the WCD, 2 VEM or 2.8 VEM respectively. Th-T1 reduces the event rate from $\approx$3 kHz to $\approx$100 Hz.

- ToT-T1 is a *time over threshold* trigger which generates a sliding 120-bin window (approximately 3 μs) and requires that at least 13 bins are above a signal value of 0.2 VEM. This trigger is intended for small

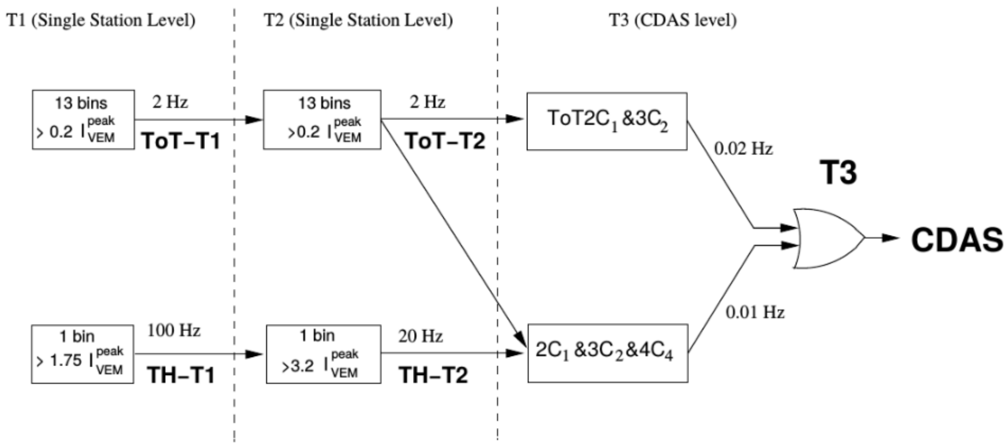

Figure 3.5: Structure of the SD triggers from the trace to the T3 array trigger.From [110]

signals spread in time, for example, lower energy events or high energy events far from the shower core. The ToT rate is 2 Hz or less.

The T2 trigger

The T2 trigger is more stringent than T1 and it reduces the rate of events to 20 Hz, to render the data stream digestible by the bandwidth of the communication line between the stations and the campus. All ToT-T1 are considered automatically ToT-T2, while Th-T1 triggers need to exceed a higher threshold of 3.2 VEM with a coincidence of 3 PMTs to be promoted to T2.

Two additional T2 triggers have been implemented since 2013:

- ToTd-T2 (Time-over-Threshold deconvoluted) uses the average decay time of light inside the Cherenkov tank to identify signals too small to trigger the ToT criteria. The concept behind the trigger is the fact that signals with a large electromagnetic component will present themselves as a sharp peak followed by a long exponential decay tail with Poissonian fluctuations. Once the exponential tail has been deconvoluted, the trace is processed by the ToT algorithm. This results in a rate of 0.3 Hz

- MoPS-T2 (Multiplicity of Positive Steps) is a unique trigger, completely detached from the VEM calibration. The algorithm tracks the number of consecutive bins registering an increase and the amplitude of that increase. These clusters of bins have an upper threshold, given by the increase from a vertical muon, and a lower threshold, dictated by the average noise. The clusters that pass these thresholds are counted in the multiplicity of positive steps m. A trace passes the MoPS trigger if $m > 4$ in a window of 120 bins. This also results in a rate of 0.3 Hz.

Examples of traces passing the different T2 triggers are shown in figure 3.6.

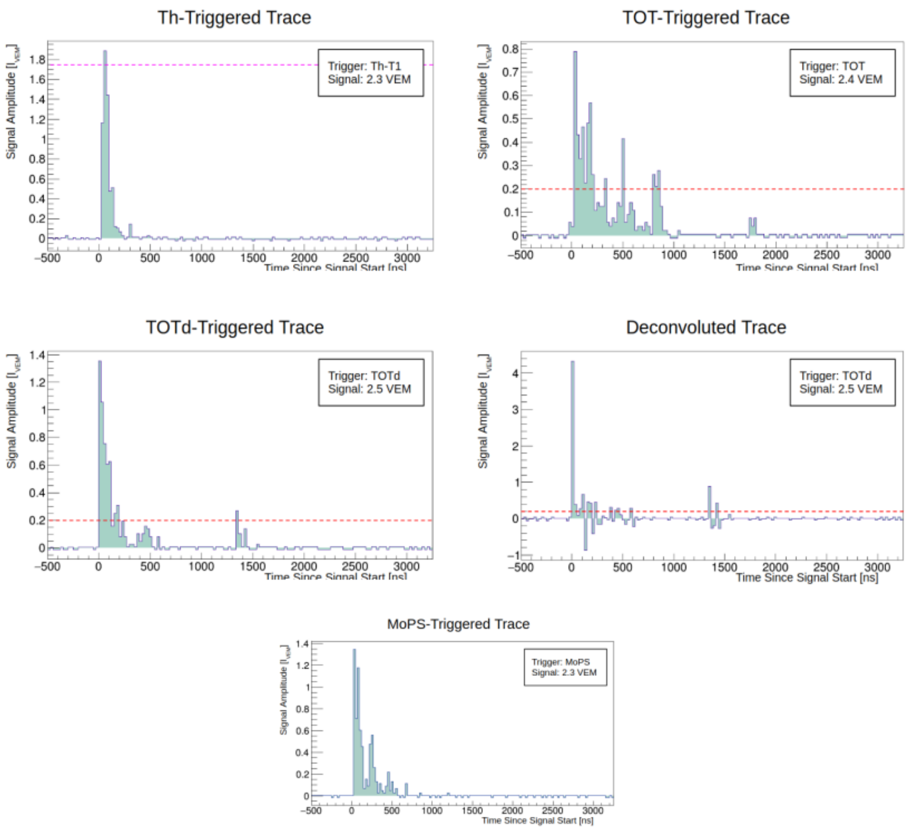

Figure 3.6: Examples of traces that pass the four T2 triggers. Top row the "old triggers" Th and ToT. Second-row ToTd, before deconvolution on the left and after on the right. Bottom row MoPS.

The T3 array trigger

The stations that trigger any of the T2 conditions send a notification to the CDAS. The CDAS then applies the T3 trigger, which is an array-wide selection. It searches for real showers by identifying clusters of nearby T2-triggered stations. Two clustering configurations are used, based on the division of the array in *crowns* surrounding a selected station, as can be seen in figure 3.7. The first is ToT2C1&3C, which asks for 3 ToT in coincidence, with one triggered station taken as the center of the crowns, one in its first crown and one in its second. This trigger is very efficient at selecting physics events, with a 90% success rate; around 1600 events per day pass it. The 2C1&3C2&4C4 configuration is more relaxed, and it is particularly useful for selecting inclined showers because of their footprint on the ground. It requires no ToT in particular but adds the requirement of an additional fourth station at least as close as the fourth crown from the core. Around 1200 events pass this selection daily, but only 10% are real showers. For both configurations, a timing selection is added to check if the traces are distributed in time in a way that is consistent with particles in a shower traveling at almost the speed of light. The clusters of triggered stations that pass these requirements are promoted to T3, and the CDAS stores all the information received from the stations in the selected configuration as well as nearby stations that were T1- or T2-triggered in a window of 30 μs around the T3.

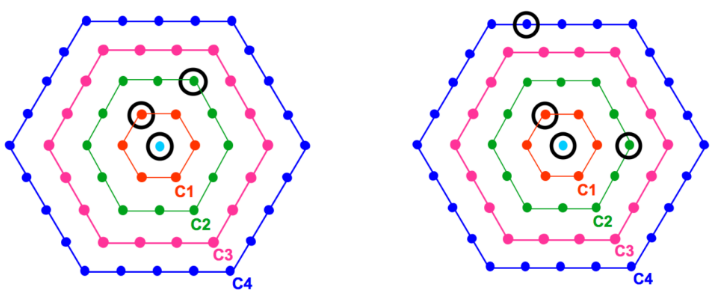

Figure 3.7: Examples of the two T3 triggering modes: ToT2C1&3C on the left, 2C1&3C2&4C4 on the right.

3.4.3 Selection triggers: T4 and T5

The T4 physics trigger

The T4 trigger is responsible for selecting the T3 configurations that are consistent with EASs. This selection is needed due to the high number of fortuitous coincidences that are expected. Two different selection conditions are applied. The first is the 3ToT, which requires the presence of 3 ToT stations in a triangular pattern; due to the very low rate of ToT, less than 1 chance coincidence per day is expected. The second condition does not require any particular T2 class, only 4 nearby triggered stations, hence the name 4C1. As for the T3 selections, both configurations also require timing information consistent with a shower front moving at close to the speed of light. Events with a zenith angle below 60 degrees are easier to identify due to the very compact shower front (in fact the T4 trigger efficiency is 100%), while more inclined events require a much different procedure for the application for the T4 trigger, called *top-down*.

Having discarded the accidental events, the focus of the trigger is shifted to the stations present in the real events, to select the spurious triggers. A *seed* of stations is picked, composed of three non-aligned neighboring stations. The arrival direction is estimated from the seed by fitting the timings and the geometry of the triangle. If the event only has aligned stations it is not reconstructed due to the difficulty in determining the arrival direction. Subsequently, the other tanks are evaluated and added to the *selected stations* of the event if their timing is consistent, or flagged as *random stations* if their time delay from the core is outside the expected window. Stations are also flagged as random if they have no triggered neighbors in a 3 km radius.

The inclined T4 trigger by contrary is *seedless*, so no group of stations is picked at the start of the procedure. The goal is similarly to make sure that the start times of the signals of at least four neighboring T2-triggered stations are consistent with a shower front traveling at the speed of light. From the full list of triggers, stations with times outside the window that corresponds to the passage of the shower front, as established by the other stations, are removed to eliminate accidental triggering. Starting with the

T3 trigger selection, stations are eliminated one at a time by picking the ones with the highest timing offsets, until a good configuration with four or more stations arranged compactly is discovered. This removes a large number of showers reconstructed with incorrect arrival directions due to random coincidences [111].

The stations that are active but not triggered are used in the reconstruction if they are close enough to the core of the shower, because of the possibility of being sub-threshold. These stations, called *silent stations*, are found by looking at the database of all stations involved in reconstruction and counting how many T2 triggers are missing from an event.

The T5 fiducial trigger

For an accurate reconstruction of the characteristics of the showers, the full shower footprint needs to be detectable. The T5 trigger selects events by starting from the station with the highest signal, or *hottest*, and cataloging them based on the number of active stations in its surroundings (non-triggered stations are counted as active). For example, if a shower was to fall on the border of the array or in the vicinity of an inactive tank, the vent could have a misreconstructed core position and energy.

The prime selection is the **6T5** condition, which labels all events in which the hottest station is surrounded by 6 active stations, a full *hexagon*. This selection however reduces the instantaneous exposure of the array by circa 10%; this is not a major issue for most physics analyses and as such almost all Auger analyses use the 6T5 condition. An exception is the ones that focus on the highest energy events: in this energy region low statistics are the main hurdle and additionally, the footprint of the shower on the ground is large enough to ensure a good sampling even without a complete hexagon near the hottest tank. Thus, the relaxed conditions **5T5** and **4T5** are used, respectively requiring 5 and 4 active tanks in the hexagon. 5T5 and 4T5 events are required to satisfy an additional condition on the position of the reconstructed shower core: if the core position is within an equilateral triangle of active stations the event is labeled as **pos**, while if within an isosceles triangle, it is labeled as **pos2**. Events that do not pass any of these two conditions are **nopos**. 6T5 events are automatically also pos.

In the case of very inclined showers, the application of the T5 trigger is largely the same, with the difference that the center of the hexagon is not the hottest station but the station closest to the reconstructed shower core position.

3.5 SD event reconstruction

The main goal of the event reconstruction of the SD is to estimate the arrival direction and energy of the primary cosmic ray. Arrival direction is mostly estimated via *geometrical* reconstruction, via a fit of timing information from the stations. Energy is more complicated to reconstruct, and it is mostly obtained by estimation of the *density of particles* and its dependence on the distance from the shower core, the so-called *lateral distribution function* (LDF).

3.5.1 Geometrical reconstruction and arrival direction

As previously mentioned in the T4 trigger section, when at least three non-aligned stations are triggered, it is possible to apply a fit to the shower front it is assumed plane, which is a rough approximation but proven robust. Imagining a plane shower front arriving at the ground with direction a, stations at position x will be triggered at time:

$$ct(x) = ct_0 - (x - b)a$$

where t_0 is the impact time of the shower core and b points to the impact point. A sketch of this approximation is visible in figure 3.8. The vector a can be evaluated by minimizing a χ^2 function built on the previous equation. This vector translates to first approximation values for the coordinates in the local coordinate system of the Observatory, the zenith angle θ and the azimuth angle ϕ. The uncertainties, assuming perfect knowledge of the shower positions, only come from the timing of the stations. The approximation of the shower front can be refined using a non-planar geometry after the application of the LDF fit and determination of the position of the shower core.

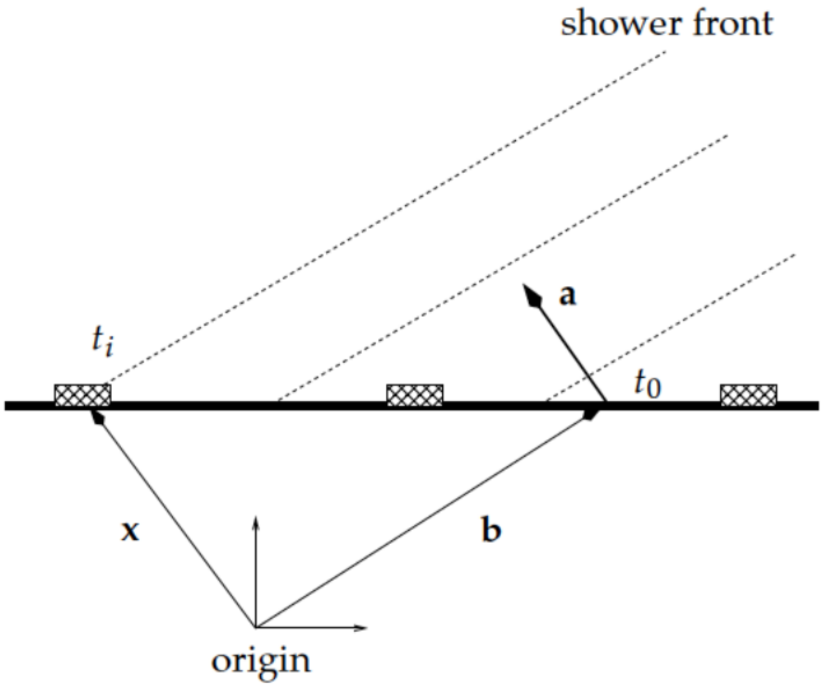

Figure 3.8: Planar approximation of the shower front. Courtesy of Hugo Rivera

1282 3.5.2 Lateral distribution of particles

The density of particles was highlighted as a good estimator of the energy of the primary particle by Hillas. As it is not feasible to cover the whole surface of the array with detectors, the density of the particles is unlikely to be measured directly at the needed distance from the core. Hence the signal at the selected distance is inferred from a fit to a given LDF, using the signals from the triggered stations. This fit gives information on two shower observables, the lateral density of particles, and the position of the shower core. The estimation of the shower core, as said previously, is used to obtain a more refined determination of the arrival direction, modeling the shower front using spherical geometry. The signal estimation at fixed distances allows for the determination of the energy of the event after appropriate calibration. The optimal distance for this estimation is 1000 m in the Auger SD, and it is estimated primarily from the array geometry. The model signal is called S_{1000}, or *size parameter*, i.e. the signal that would have been

measured by a detector placed 1000 m from the shower axis; the LDF must also satisfy the condition LDF(1000 m)=1. The signal at a certain distance can then be extracted using the formula $S(r) = LDF(r)S_{1000}$.
The Pierre Auger Collaboration uses two main versions of reconstruction software for the vertical events in the SD: the CDAS-Herald and the OffLine. The first has historically been used for studies on the arrival direction of events and for quality controls because of its quicker visualization of the data, while the second is used for studies on the spectrum and mass composition, among others. While initially two different LDFs were implemented in the two pieces of software, now they both employ the NKG function [112][113] for the fitting procedure; however, the fit is performed using a maximum likelihood method in OffLine and a χ^2 minimization in CDAS-Herald. The NKG function is defined as:

$$S(r) = S_{1000} \left(\frac{r}{1000m}\right)^{\beta} \left(\frac{7000m + r}{1000m + 7000m}\right)^{\beta+\gamma}$$

where the β parameter is related to the slope of the LDF and γ to the curvature.

3.5.3 Energy calibration

Once the size parameter is estimated, the last piece to reconstruct the energy of the primary cosmic ray is the energy calibration of the estimator. Auger has the great advantage of being a hybrid observatory and thus having the calorimetric energy from the Fluorescence Detector available for a subset of lucky events, the so-called *hybrids*. The cross-calibration from these events allows us to compute a conversion factor that is effective for all the SD events.

The constant intensity cut

Beforehand however an additional correction must be applied to S_{1000}, to eliminate its dependence on the zenith angle of the incoming shower. At fixed energy S_{1000} decreases with increasing θ due to atmospheric absorption and weather effects. The correction is done using the attenuation curve of showers, which is derived using a *constant intensity cut* method (CIC) [114], which assumes that the flux of cosmic rays is largely isotropic. The θ-independent energy estimator is S_{38}, or the S_{1000} that the shower would have produced had it arrived at the median zenith angle of 38 degrees $S_{38} = S_{1000}/p(x)$, where $x = \cos^2(\theta) - \cos^2(35°)$ and $p(x)$ is a polynomial obtained from the CIC.

Golden hybrids event and the energy

With the zenith angle correction applied, the energy can be estimated with the formula $E = AS_{38}^{B}$, where the coefficients A and B are determined by the cross-calibration to fit with the measurements with the Fluorescence Detector applied to a subset of high-quality hybrid events, the *golden hybrids* (figure 3.9). These events are required to have triggered the SD and FD independently, as well as being 6T5 with a reconstructed core closer than 750 m to the hottest station; on the FD side, the shower is required to have an X_{max} inside the field of view of the telescope and a Cherenkov light fraction in the signal detected below 50%, as well as robust χ^2 reconstruction and errors on E_{FD} below 20% and under $40g/cm^2$ for X_{max}(for more detail on FD reconstruction see the following sections). Additional cuts based on atmospheric conditions further reduce the number of these events. The overall resolution on the energy is 15%.

3.5.4 The reconstruction of inclined showers

The previous sections focused on the reconstruction performed for *vertical* showers, i.e. with zenith angle below 60°. For *Inclined* (also called *horizontal*) showers, with zenith angles between 60° and 80°, due to the complex morphology of the EAS at ground level, a different procedure is followed.
Up to the T3 level, the trigger is the same. The T4 and T5 trigger levels, as described in their respective sections, are different from their vertical counterparts, in that the inclined T4 is a *top-down* procedure, that does not start from a seed consisting of a compact group of triggered stations, but instead eliminates stations from the triggered list until a satisfactory configuration is reached; the inclined T5 instead differs from the vertical one as the center of the crowns is not the station with the highest signal but the closest to the reconstructed shower core, making it an *a posteriori* selection.
The most consistent difference in the reconstruction of inclined showers comes at the level of energy reconstruction. The method is not based on the signal at a fixed distance from the reconstructed core of the shower plane but

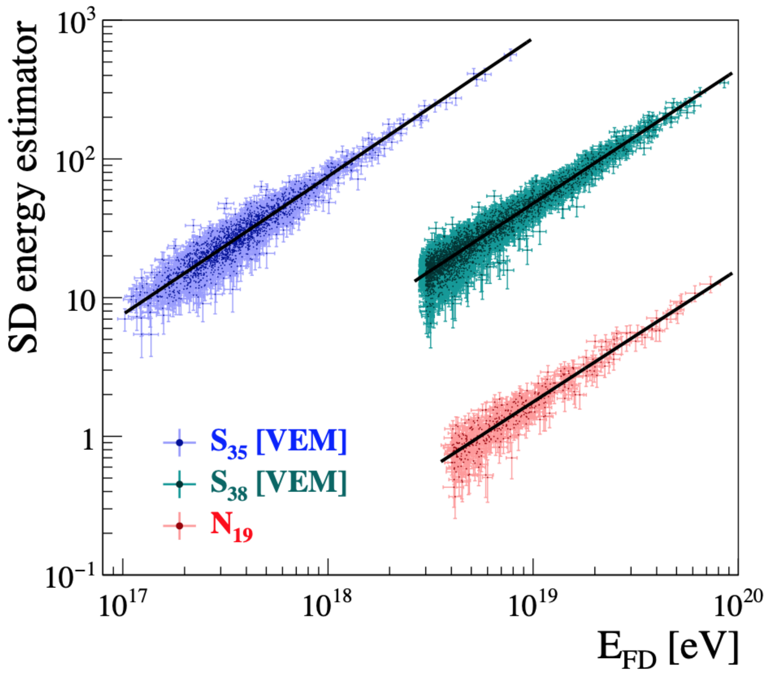

Figure 3.9: Calibration function of the SD estimators for vertical events (S_{38}), infill events (S_{35}) and inclined events (N_{19}) to the energies reconstructed by the FD. From [115]

on a fit of the measured signals to the expected pattern from simulations. This is due to the fact that inclined EAS patterns on the ground are strongly dominated by muons, and thus their reconstruction requires accurate two-dimensional modeling of the muon number densities, the detector responses, and the treatment of the electromagnetic component of the signal. As the reference pattern taken is the one for a proton shower at an energy of 10^{19} eV, the energy estimator is called N_{19}, defined as the measured shower size normalized to the reference muon distribution: $N_{19} = \rho_\mu(r)/\rho_{\mu,19}(r,\theta,\phi)$. The energy calibration to golden hybrids events is performed similarly to vertical events.

3.6 The fluorescence detector

The fluorescence detector of the Pierre Auger Observatory, or FD, is composed of twenty-four telescopes with four groups of six in different locations, or *sites*, called Los Leones, Coihueco, Loma Amarilla, and Los Morados. The FD is designed to complement the detection technique of the SD. Charged particles in the EAS excite the molecules (primarily the Nitrogen) in the atmosphere, and subsequently, these molecules decay in their ground state emitting ultraviolet fluorescence light in the 300-450 nm range. The telescopes in the FD observe the atmosphere looking for these faint light signals, which are visible only on clear nights with low moon coverage, and due to these constraints the duty cycle of the FD is limited to $\approx 15\%$. The great advantage of this technique, as stated in the previous chapter, is the possibility of using the atmosphere effectively as a calorimeter, as integrating the shower profile seen by the telescope accounts for $\approx 90\%$ of the energy of the EAS, while the remaining part, the *invisible energy*, is carried away by neutrinos and high energy muons and does not dissipate in the atmosphere.

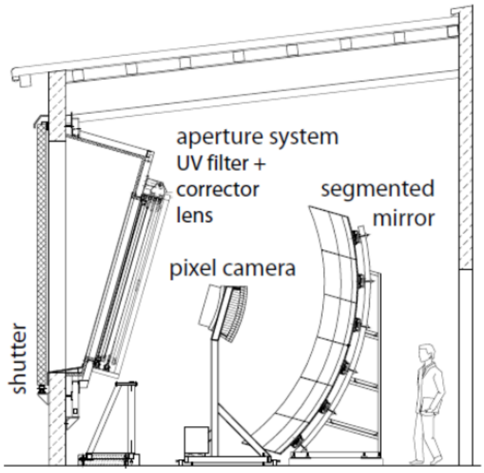

Figure 3.10: Schematic side view of the fluorescence telescope optical system.

3.6.1 The telescopes

Each of the 24 telescopes that compose the FD has a field of view of $30^\circ \times 30^\circ$ in elevation and azimuth, which, when combining all of the 6 telescopes in one site, gives a total of $30 \circ \times 180 \circ$ per site. The telescopes are of Schmidt design, with a 3.6 m diameter mirror focusing the light on an array (or *camera*) of 440 PMTs (or *pixels*), each with a field of view of $1.5^\circ \times 1.5^\circ$. Light enters through an aperture diaphragm of 1.7 m. The illuminating aperture features a UV filter that improves the signal-to-noise ratio and a corrector lens is installed around the aperture to reduce aberrations. A sketch of the FD optical configuration can be seen in figure 3.10.

3.6.2 FD triggering and calibration

PMT signals from the camera of the FD telescopes are collected by an analog board, which filters and amplifies them. The analog board is connected to a digital front-end that hosts the first and second-level triggers (FLT and SLT), respectively at pixel and camera levels, which are applied to the signals after 12-bit 10 MHz digitization.
The FLT is imposed to keep the event rate at around 100 Hz and requires that the sum of the last 10 bins of the PMT trace are above the set threshold value. The SLT searches the camera using a sliding window of 5×22 pixels requiring at most one below threshold and results in a rate of 0.1 Hz. The third level trigger (TLT) is at the level of the *mirror PCs*, and it loops all the SLT events looking for spurious triggers and random alignments. TLTs are then merged to have complete telescope information. An example of the final trace can be seen in figure 3.11.

The absolute calibration of the FD telescopes is performed once a year with a diffuse light source consisting of two pulsed LEDs of 375 nm wavelength. The source illuminates each pixel with a known intensity, allowing the transformation of the integrated electronic signal in collected photons. A relative calibration procedure also confronts the total charge collected by all the PMTs. A cross-check of the calibration is performed using the Central Laser Facility (CLF), which is positioned at the center of the array. CLF fires a laser of known energy and direction; these lasers Rayleigh scatters in the air and in part arrive in the fluorescence telescopes' field of view. The light from CLF produces a signal comparable to a shower of energy around 10^{20} eV.

3.6.3 FD event reconstruction

In the FD the showers are detected as a series of triggered pixels with timing information. The reconstruction of the events starts with the determination

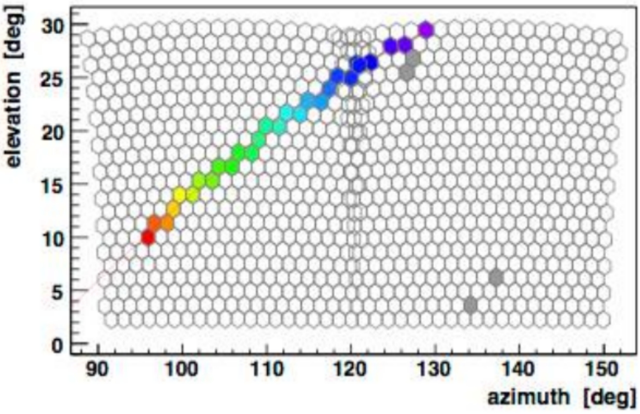

Figure 3.11: Example FD trace, with the color code corresponding to the timing

of the Shower-Detector plane (SDP), which is the plane that includes the eye and the shower axis (figure 3.12). A fit is then applied to the time information of the pixels illuminated by the fluorescence light, and results in three parameters: the perpendicular distance from the shower axis to the FD site R_p, the timing of such distance t_0 and the orientation of the shower axis, χ_0:

$$t_i = t_0 + \frac{R_p}{c} \tan\left(\frac{\chi_0 - \chi_i}{2}\right)$$

where χ_i is the angle between the horizontal line of the SDP to each pixel. If the angular speed $d\chi/dt$ is particularly stable, multiple solutions for χ_0 and R_p are possible. This degeneracy can only be broken by adding information from the SD. The resolution for arrival direction is improved when the same event is seen by two (*stereo*), three (*triple*), or more FD stations.

Once the shower geometry is known, the light collected as a function of time can be converted into energy deposit as a function of slant depth. The fluorescence light contribution to the total signal must be disentangled from other contributions, direct and scattered Cherenkov light from particles in the shower and multiple-scattered light. The light collected by the telescopes must be corrected for the attenuation between the shower itself

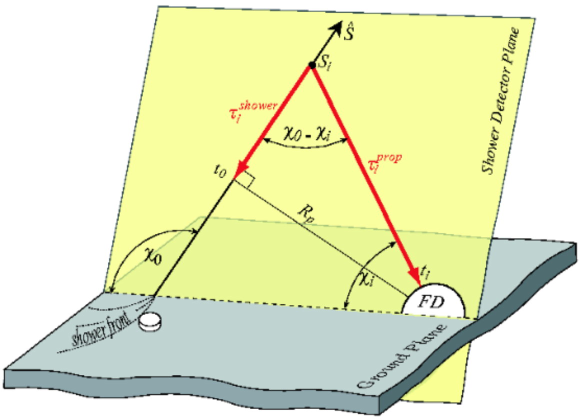

Figure 3.12: Representation of the shower-detector plane

and the detector: this is done thanks to accurate continuous atmospheric and weather monitoring. The calorimetric energy of the shower is estimated by fitting the reconstructed profile to the Gaisser-Hillas function [116] and integrating it:

$$f_{GH} = \left(\frac{dE}{dX}\right)_m ax \left(\frac{X - X_0}{X_{max} - X_0}\right)^{(X_{max}-X_0)/\lambda} \exp\left(\frac{X_{max} - X}{\lambda}\right)$$

From Monte-Carlo simulations, this accounts for circa 90% of the total energy, with the remaining *invisible* energy carried away by neutrinos and high-energy muons. The systematic uncertainty on this fraction is of the order of 5%. Overall, the resolution of the FD is 10%, mostly of statistical origin. The position of the shower maximum X_{max} is also obtained from the fit to the Gaisser-Hillas function, with an associated uncertainty of ≈20 g/cm^2.

3.7 The hybrid exposure

As previously introduced, events that trigger both the FD and the SD are called *hybrids*. Events with energy above 1 EeV that trigger the FD always also trigger the SD, helping with the FD reconstruction and providing, as stated in the previous sections, the possibility of cross-calibration for energy determination is SD-only events. The exposure of the Observatory in hybrid mode is calculated using Monte-Carlo simulations tuned to the time dependence; this tuning takes into account the changing configurations in the SD and FD, with a time window of 10 min, evaluating the efficiency of all detectors down to the single PMT level. Atmospheric monitoring data is added as input for the simulation. One of the issues in the evaluation of the hybrid exposure is the impact of the hadronic models, which is linked with the missing knowledge on mass composition. The total systematic uncertainties, mostly due to the composition, are around 10% at the EeV and 1% at 10 EeV.

3.8 Observatory Enhancements

The Pierre Auger Observatory, in addition to the main components of the FD and SD, has additional detection features with multiple objectives: extending the energy range to the region between 10^{17} eV and 10^{18} eV; adding detection techniques to investigate mass composition; extending the longitudinal profile studies to the surface detector via radio arrays. In this thesis, no data from the enhancements was used directly for the analyses.

3.8.1 AMIGA and the Infill

AMIGA (Auger Muons and Infill for the Ground Array) is an SD enhancement consisting of two main parts:

- A denser sub-array of the Surface Detector called the *Infill*, composed of 60 stations added to a region of 23.5 km^2 close to the Coihueco FD side; the infill has a spacing of 750 m, allowing for full efficiency detection of showers of energy above 3×10^{17} eV, which gives Auger the possibility of investigating in full the region across the ankle of the CR spectrum. The infill was completed in 2010 and uses the same reconstruction as the SD, substituting the estimator S_{450} to S_{1000}. It is capable of detecting showers up to 55° in Zenith.

- A series of Muon detectors, in continuous deployment, buried at a depth of 2.3 m. Each detector consists of 64 plastic scintillator bars with a total area of 30 m^2, capable of detecting > 1 GeV muons that penetrate into the soil. The purpose of these detectors is to study the accuracy of the muon counting algorithms in the SD.

3.8.2 HEAT

As lower energy showers develop higher in the atmosphere, the regular FD telescopes are not able to detect them. HEAT (High Elevation Auger Telescopes) is an additional group of three telescopes, situated very close to the Coihueco FD building and thus overlooking the Infill array; it was optimized for higher altitude observation, with the capability of tilting the eye 29° upwards. In the energy and elevation range sampled by the HEAT telescopes, the total EAS light emission has a sizeable Cherenkov component; this Cherenkov light is visible by the HEAT telescopes if the shower is close enough to the FD site, due to the beamed nature of the effect. The combined Coihueco-HEAT site covers from 0 to 58 degrees in elevation. A view of the HEAT telescopes can be seen in figure 3.13.

Figure 3.13: The three HEAT telescopes in the tilted-up position overlooking the SD array.

3.8.3 The 433 m array

The SD-433 is a region of additional tank density inside the Infill, consisting of 19 WCD separated by 433 m that fill out the space between the 750 m distanced stations. As it is even denser than the Infill, it can observe showers with full efficiency from the energy of 3×10^{16} eV, in the region of the second knee. The SD-433 was deployed in 2018.

3.8.4 AERA

The Auger Engineering Radio Array, AERA, is a radio array composed of more than 150 radio antenna stations deployed in three phases in the same region as AMIGA. The stations have various different spacings, between 150 and 750 m; each station is equipped with two antennas, aligned north-south and east-west and sensitive to the 30-80 GHz frequency range. Its main objective is the calibration of the radio emission from air showers, and demonstrating the arrival direction, energy, and mass reconstruction capabilities and resolution. The more densely packed antennas are more efficient for vertical showers, while the more sparse part of the array is more sensitive to high-inclination ones.

3.9 The Auger Prime upgrade

The Pierre Auger Observatory is currently undergoing a massive upgrade of many parts of its detectors, called *AugerPrime*. The main objectives of the upgrade are the following [117]:

- Clarify the mass composition at the highest energies, including elucidating the origin of the flux suppression at the toe of the spectrum. The Pierre Auger Observatory had as one of the primary goals at its construction the verification of the existence of the supposed GZK flux suppression, observed by HiRes but not by AGASA. Having observed the suppression, AugerPrime will have the task to differentiate between energy loss due to interaction with the cosmic backgrounds and the limit on acceleration energy in the sources.

- Search for the proton fraction at the highest energies, which is an extremely important ingredient for a possible future proton astronomy and the addition of cosmic rays in multimessenger frameworks. The fluxes of secondary particles, neutrinos, and gamma rays, also benefit from more precise discrimination of protons.

- Study extensive air shower to better the understanding of hadronic interactions. This task also includes particle physics studies at energies beyond accelerators, and beyond-the-standard-model physics, such as Lorentz invariance violation and Dark Matter searches.

To accomplish this, the Observatory's sensitivity to mass composition is the main area of interest and upgrade, especially in the highest-energy region. As for now, only the FD has direct access to the X_{max} of the showers, one of the two main ingredients in discriminating the primary species, the other being the number of muons, which is not directly measurable by the full detector at the moment. The strategy of improvement is then to extend sensitivity to these observables to as much of the Observatory as possible, by adding new detectors and improving the present ones, as well as reducing the systematic uncertainties and expanding the duty cycles of instruments.

The Scintillator Surface Detector

Each SD station will be equipped with a plastic scintillator (SSD), positioned on top of the WCD tank. As the WCD and the SSD have different responses to muons and electromagnetic particles: the measurements are complementary, providing a good separation between the two components. In more detail, the SSD will be much more sensitive to the electromagnetic component with respect to the muons, while the WCD is more sensitive to the muonic component. Discriminating between the muonic and electromagnetic components gives way to a more precise determination of the muon number in the shower, enabling mass reconstruction in the Surface Detector. Due to the small geometric cross-section, the SSDs will not be sensitive to the inclined air showers. Each SSD station has two modules of 2 m^2, composed of 24 bars; the scintillation light is guided and wavelength-shifted by optical fibers and collected by photomultiplier tubes. The bars are positioned in a "U" configuration that permits single-PMT readout. Aluminum sheets are placed on top of the modules to prevent excessive movement or damage to the scintillating bars. The detector shield also comprises a roof of waved aluminum plates placed on top of the sheet to prevent direct sunlight. The deployment process is straightforward and simple to apply in all of the 3000 km^2 of the SD array; it started in 2016 and is now complete with the exception of small areas now unreachable due to difficulties in communications with local landowners.

Surface Detector electronics

The SD stations will be equipped with new, faster, and more powerful processors and FPGAs, designed to read both the WCD and the SSD outputs. The faster sampling and better accuracy will also improve the data quality, enhance the local triggering and processing capabilities, and widen the monitoring and calibration capabilities of the stations. The deployment of the boards is also simple and started right after the SSD; at the moment around one-third of the stations are equipped with the new electronics.

Small PMT

The dynamic range of the current PMTs in WCDs presents an obstacle, especially in the case of very energetic events. In fact, as much as 40% of the events with energy above 30 EeV suffer from saturated traces in one or more channels of the stations closest to the shower core. A fourth new phototube with a smaller cathode, called "SmallPMT", will be added to each station to extend the dynamic range, with an expected drop of saturated events to 2% even at the highest energies.

Underground Muon Detector

The Underground Muon Detector (figure 3.14) is designed to provide direct measurements of the shower muon content and timing distribution, as well as provide calibration to the SSD+WCD combination. As the AMIGA muon detectors fulfill the requirements, the plan is to deploy the MDs all over the SD Infill area, covering 23.5 km^2. The completed AMIGA MD array will then become the UMD.

Radio array

On top of the WCD and SSD, each Surface station will be equipped with a *short aperiodic loaded loop antenna* (SALLA) (view of a completed station

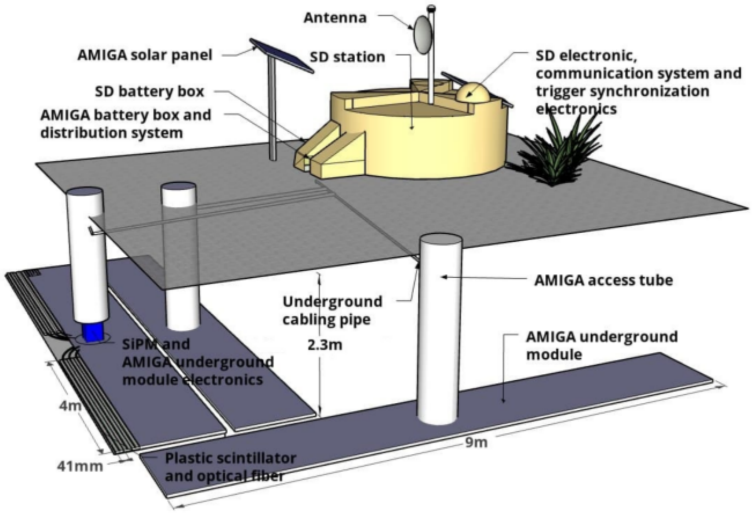

Figure 3.14: Schematics of a UMD station, with the buried modules and plastic electronics access tubes.

is shown in figure 3.15). As discussed previously the radio emission from EAS come primarily from the electromagnetic component of the shower. In inclined showers the em and hadronic components are absorbed by the atmosphere before reaching the ground, leaving only the muonic component as a measurable footprint on the SD. However, radio emission from the electromagnetic component of the shower reaches the ground anyway, opening the possibility of electromagnetic/muonic ratio measurements for high-inclination showers, just as the combination of WCD and SSD will do for vertical ones. This e/μ ratio will be used to extend particle mass discrimination studies to the whole zenith angle range.

Duty cycle of the Fluorescence Detector

The Fluorescence Detector will be updated in parallel with the SD to extend the uptime of the telescopes. The current nominal duty cycle is 19%, reduced to 15% due to weather effects, power cuts, and limiting exposure of the PMTs to periods of high luminosity. Lowering the supply voltage, and thus the gain of the PMT improves their capability of operating in periods of the higher sky background. The current setup is compatible with this modification, bringing the duty cycle to an expected 29%.

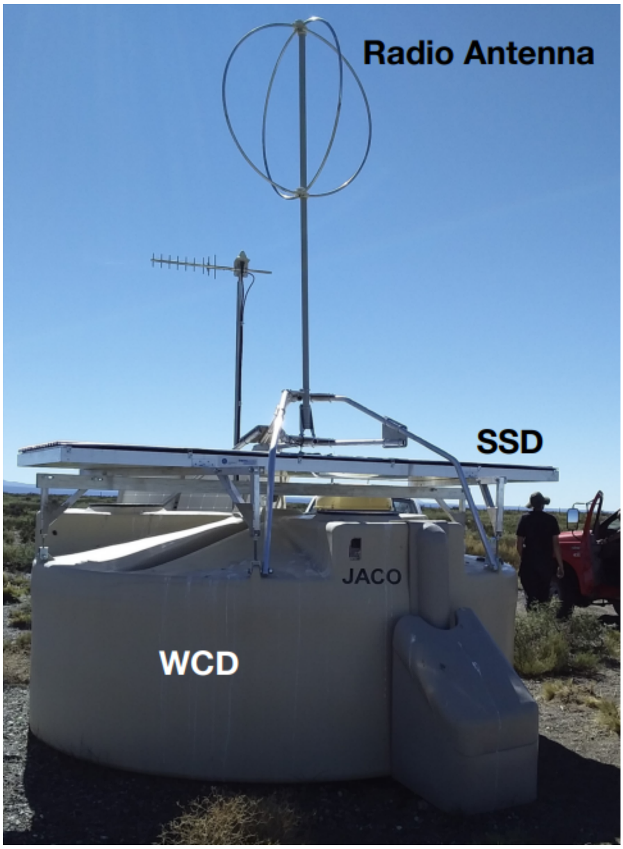

Figure 3.15: A complete AugerPrime Surface Detector station, comprising the WCD, SSD, and radio antenna

3.10 Review of the main physics results of the Pierre Auger Observatory

The Pierre Auger Collaboration in more than 20 years of existence and 18 years of operation of the Observatory has published some of the most advanced results in the field of Ultra High Energy cosmic rays. In this section, some of the most interesting results are briefly presented.

3.10.1 Energy spectrum

The CR spectrum with the widest energy range measurable by the Observatory spans from 6×10^{15} eV to the highest energies and is obtained as a combination of five datasets: SD-1500 events, vertical and inclined, SD-

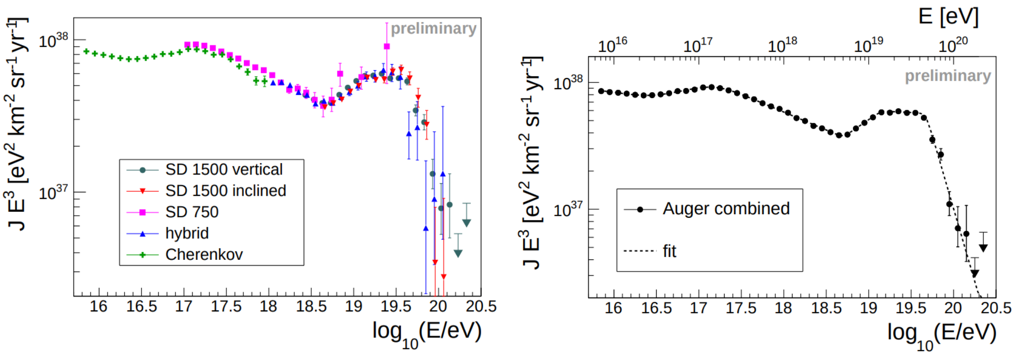

Figure 3.16: Cosmic ray intensity J, multiplied by E^3 estimated using five different techniques. The different spectra had to be systematically shifted between 5% and 7% to match each other. The different spectra are shown as separated and color-coded (left plot) or combined and superimposed with the fit function (right plot). From [118]

750 events, hybrid FD+SD events, and a set of Cherenkov-dominated events recorded by the HEAT telescopes (figure 3.16). This allows full investigation of the regions across the ankle, as well as the 2nd knee, and the first detection by Auger of the *low energy ankle* a hardening of the spectrum at 28 PeV probably connected to changes in the mass composition of the Galactic component of cosmic rays [118].
The most recent publications, in 2020, focused on the spectrum measured by the SD-1500 above 2.5×10^{18} eV. In these results, the energy of the ankle, and other highest-energy features such as the instep and the toe/suppression, which was first proven to exist definitively by Auger, as well as all the changes in the spectral index, are determined with an unprecedented level of precision.(3.17).

3.10.2 Mass measurements

The mass of the primary particle is not directly measurable in the indirect detection of cosmic rays. However, as described in chapters 1 and 2 and in the previous sections, the primary mass has a strong impact on many properties of the EAS, among which the depth corresponds to the maximum extension of the shower, X_{max}. The Fluorescence Detector is able to directly measure the showers' longitudinal profiles, and therefore has access to the X_{max}, reported in figure 3.18. Diverse methods, based on Monte-

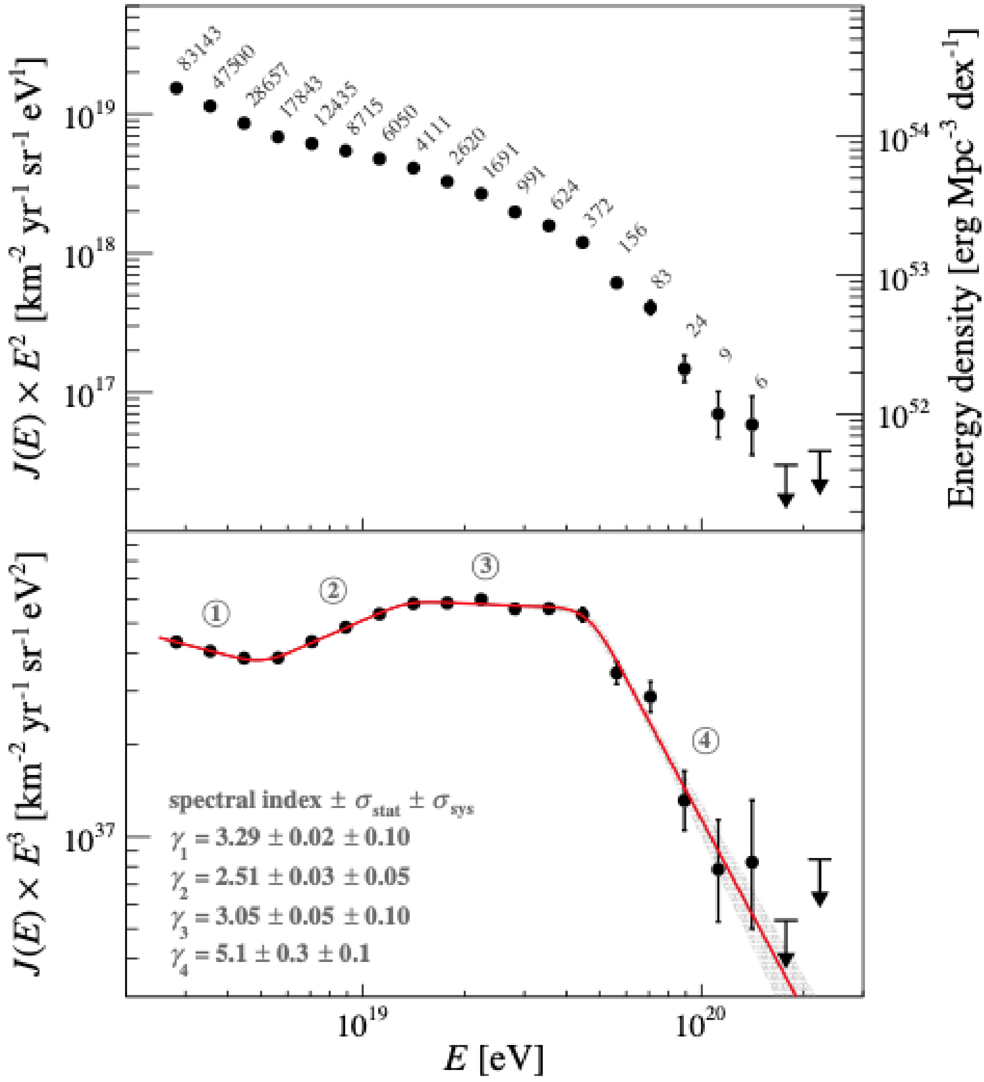

Figure 3.17: Cosmic ray spectrum at the highest energies as measured by the Pierre Auger Observatory. From [119].

Carlo simulations, are now being applied to data from the Surface Detector in order to extract information on X_{max} (figure 3.19). AERA is also able to reconstruct the X_{max} based on simulations of the shower's radio footprint on the ground (figure 3.20).

All the measurements done with different sections of the Observatory

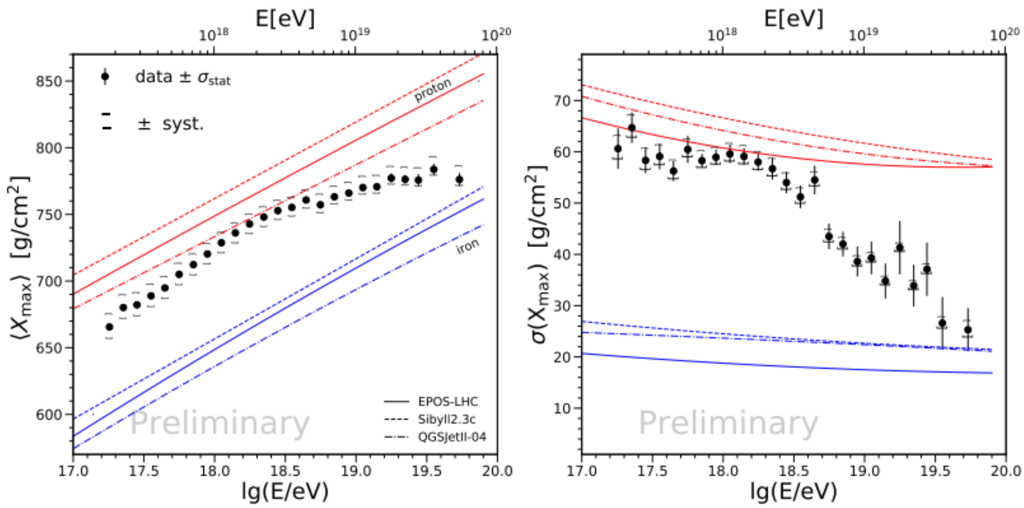

Figure 3.18: Measurements of of X_{max} from the FD. The left plot shows the average depth of maximum as a function of energy; the right plot shows the standard deviation. Auger data, in black, is compared to simulated results from proton (blue), or iron (red) showers, produced with different hadronic models. From [120].

are in statistical agreement with each other. The mean X_{max} shows a composition that is compatible with lighter and lighter primaries in the range between 10^{17} and $10^{18.4}$ eV, after which the trend reverses, and the distribution of the average mass grows increasingly heavy; the trend is supported also by the second-moment distribution, which shows a narrower distribution after the turn towards heavy primaries.

Combined Fit

The X_{max} measurements are not enough to infer the distribution of the primary composition. The degeneracy can be broken down by adding information on the spectrum of UHECRs, as well as source models. As detailed in chapter 1, the maximum attainable energy in the sources of UHECR depends on the rigidity: the spectrum at the highest energies is expected to be dominated by heavier, higher-Z elements, if there are no additional reasons for these heavier components to be absent or absorbed in the sources. This is shown in figure 3.21, taken from [123], obtained by simultaneously fitting X_{max} measurements and spectrum measurements, with a model of the

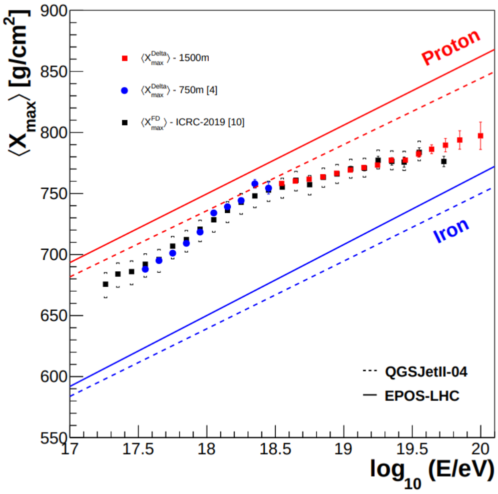

Figure 3.19: Evolution of X_{max} with energy inferred with the *delta method* using SD measurements. The SD-1500 measurements are reported in red squares, SD-750 in blue squares, and FD measurements in black for comparisons. The data are compared with simulated results from proton (blue), or iron (red) showers, produced with different hadronic models. From [121].

source contributions across the ankle. The result is a region above the ankle described by a very hard extragalactic component dominated by medium mass elements, with the suppression being the result of a mix of propagation energy losses and source energy cutoffs; below the ankle, the presence of a Galactic light component is disfavored, as the data is better described by a second, very soft and light extragalactic component, either composed of protons in the case of photodisintegration near the acceleration sites or light mixed nuclei in the case of a different population of sources.

Mass-dependent anisotropies

As the composition around and above the ankle region is thought to be of mixed nature, the effect of the Galactic Magnetic Field will be a differing deflection based on the primary species. Additionally, different primaries are thought to have differing horizons due to propagation effects, and therefore different source distributions. These ingredients point to the possible rise of mass-dependent anisotropies in the UHECR flux. Specifically, the result due to the propagation of UHECRs in the GMF would be a stronger

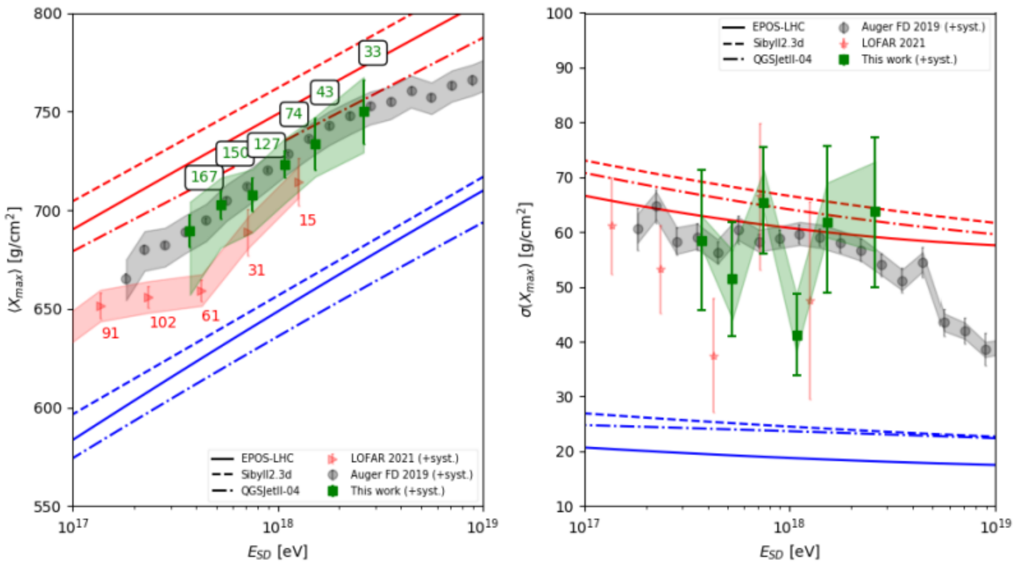

Figure 3.20: Measurements of of X_{max} from AERA. The left plot shows the average as a function of energy; the right plot shows the standard deviation. AERA data, in green, is compared to Auger FD measurements, in black, and radio reconstruction of the same kind done by LOFAR, in red. Also reported are simulated results from proton (blue), or iron (red) showers, produced with different hadronic models. From [122].

isotropicization of the flux for heavier elements, while lighter, less deflected components could retain anisotropies from their source distribution; additionally, the Galactic disk with its much stronger field is expected to obscure sources behind itself, washing out possible anisotropies and leaving only the isotropic flux of deflected heavy elements. This hypothesis was tested for cosmic rays with energy above $10^{18.7}$ eV in [124], where two analyses were performed: a simpler on-Galactic plane versus off-Galactic plane comparison of the average depth of maximum (figure 3.22) and a more complex average composition mapping analysis, comparing top-hat regions of 30 degrees in the sky versus the rest of the flux (figure 3.23). Both analyses highlight the possible presence of the theorized X_{max} anisotropy, and therefore mass difference.

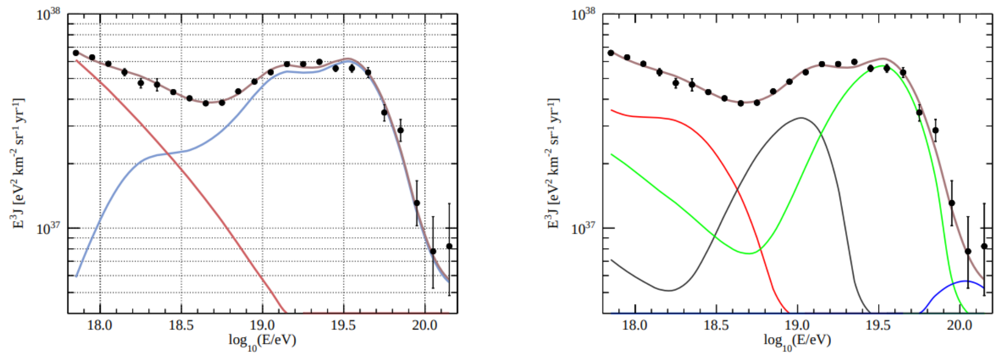

Figure 3.21: The measured energy spectrum and the estimated best-fit results in the scenario with two mixed extragalactic components. Left: the estimated contributions from the two extragalactic components (red: LE component, blue: HE component). Right: the partial fluxes related to different nuclear species at the top of the atmosphere, grouped according to their mass number: $A = 1$ (red), $2 < A < 4$ (grey), $5 < A < 22$ (green), $23 < A < 38$ (cyan), $A > 39$ (blue). From [123]

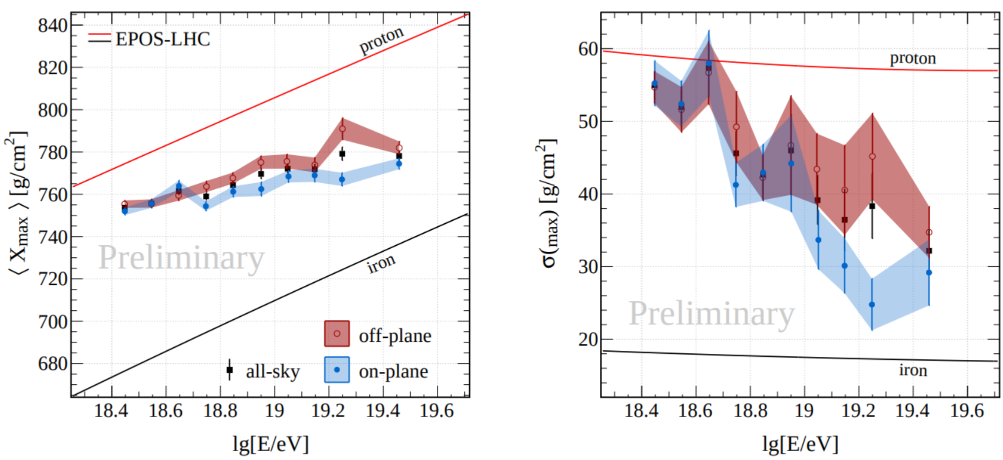

Figure 3.22: X_{max} first (left panel) and second moment (right panel), off-plane and on-plane, highlighting the trend towards a heavier composition along the Galactic disk. From [124].

3.10.3 Searches for neutral particles

Along with charged cosmic rays, the Pierre Auger Observatory is sensitive to other neutral messengers. In particular, UHE photons and neutrinos could

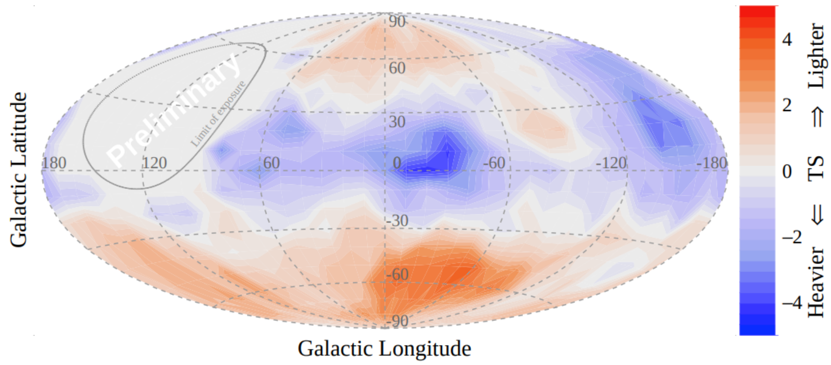

Figure 3.23: Sky map of cosmic ray average composition above $10^{18.7}$ eV. From [124].

be distinguished from the bulk of charged cosmic rays due to the different characteristics of the showers they induce; neutrons, instead, induce showers that are physically indistinguishable from proton-induced EASs, and their presence can only be inferred by the presence of very small scale clusters of events, that can be created only by non-deflected particles.

Search for photons

The Auger Observatory is the most sensitive detector in the world to photons with energy above 0.2 EeV. Photon-induced air showers are in principle discernible from hadron-induced showers thanks to a larger depth of shower maximum X_{max} and a steeper lateral distribution function, along with a lower number of muons. Combining these characteristics a discriminant parameter can be drafted, distributing the shower events between *hadron-like* and *photon-like*. In [125], X_{max} measurements are taken from the FD, while the number of muons is inferred from SD measurement thanks to the *universality of showers*, the concept which states that the energy spectrum, angular and lateral distributions of the secondary particles produced in the showers depend mostly on the primary energy and the stage of shower development. No event registered by Auger has been definitively classified as a photon event as of yet, but these searches provide the most stringent upper limits to photon fluxes in the UHE range, as seen in figure 3.24.

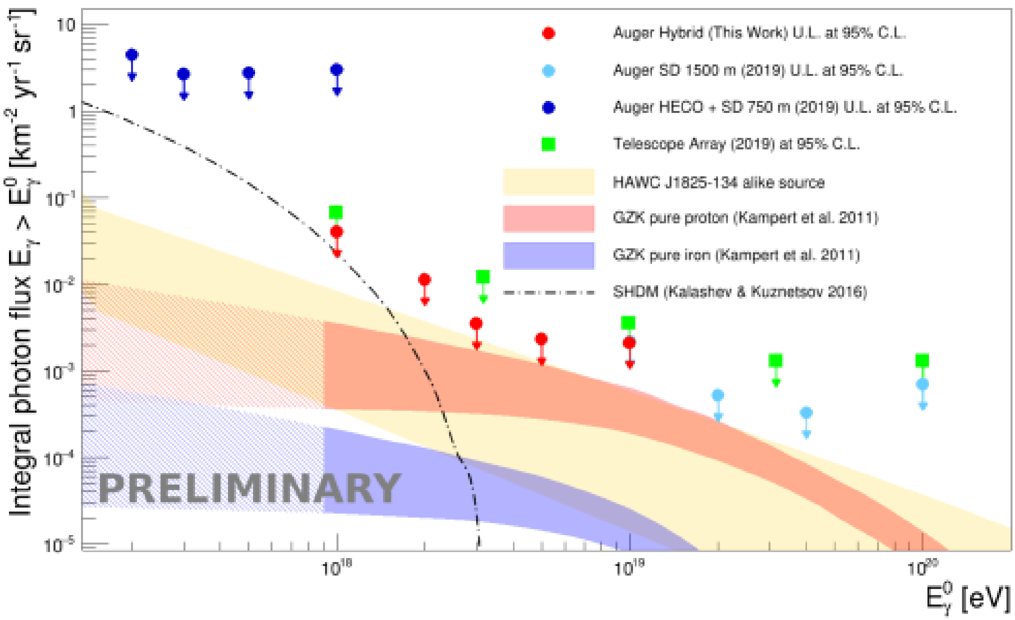

Figure 3.24: Photon flux limits at 95% C.L. obtained in [125], in red circles. Light and dark blue circles show the limits obtained by other Auger analyses using Auger data below 1 EeV and 10 EeV. The light green symbols show the limits derived from Telescope Array data. Predictions of UHE photon fluxes are indicated as colored bands, for comparison

Searches for neutrinos

Neutrino searches were planned before the actual start of operations at the Pierre Auger Observatory. In fact, the possibility of seeing a neutrino was one of the main physics cases presented. This was supported by many technical works which showed that the observatory was in an optimized position and configuration for the detection of neutrino-induced-showers, especially ν_τ, as well as more specific studies on the range of the tau leptons which were expected to be a possible target of detection by the Observatory.

The SD is sensitive to neutrino-induced showers with energies above 0.1 EeV. There are two main ways (figure 3.25)to use the SD for UHEν-EAS:

1. "Downward": the main idea is that cosmic rays interact generally shortly after entering the atmosphere, while neutrinos due to their extremely small cross-sections can start interacting at any point in the

trajectory; very inclined events are needed to provide the neutrino enough space to have a higher chance of interacting. The signature for neutrino-generated showers is steeply inclined events that start deep in the atmosphere. As these showers start closer to the ground than normal UHECR showers, they will reach detectors in a "younger" stage, characterized by a very prominent electromagnetic component that generally is completely exhausted or very minor in "older" showers, which are instead dominated by the muonic component. The angular range for this type of interaction is generally above 60 degrees, up to 90.

2. "Earth-skimming": an upward-going τ neutrino that is propagating inside the Earth can interact near the crust, producing a τ lepton that emerges from the ground and decays in flight, producing an EAS. These interactions may be identified only in the 90-95 degrees range of zenith angles. The parameter space region is practically background-free.

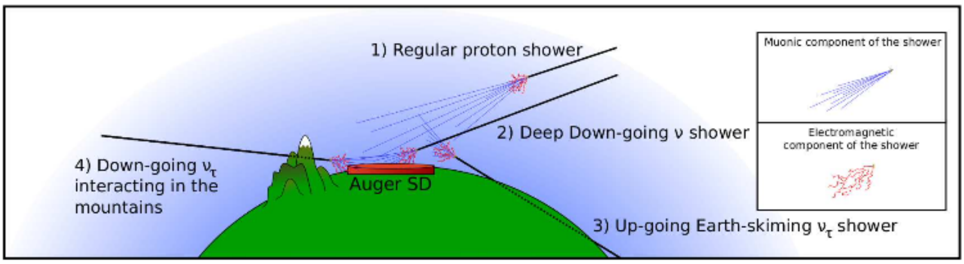

Figure 3.25: Representation of different types of neutrino events over the SD of the Pierre Auger Observatory. The "type 4" events are grouped with the ES channel.

No neutrino candidates have been found so far in Auger data [126]. However, as for photons, upper limits on the fluxes of these particles can be added, as shown in figure 3.26.

Search for neutrons

Ultra-high energy neutrons can be produced in interactions between primary protons or nuclei with the dense material close to the CR accelerators. They

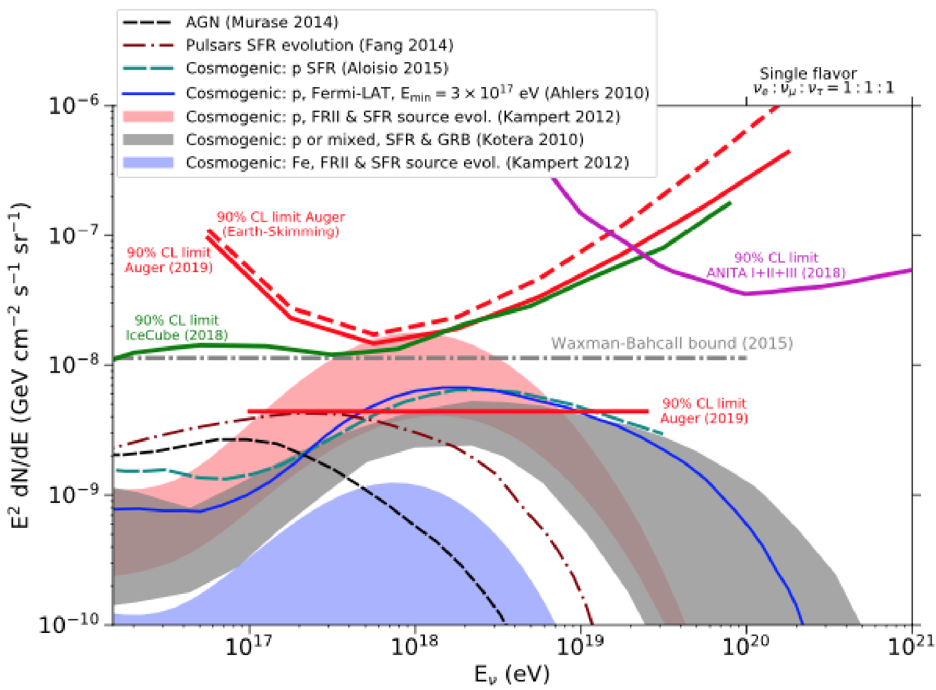

Figure 3.26: Upper limits and predictions for UHE neutrino fluxes. An upper limit to normalization of diffuse flux differential in energy bins of 0.5 in $\log_{10} E_\nu$(red line all flavors, dashed red line only ES). Differential limits from ANITA (magenta) and IceCube (green). Neutrino fluxes for various cosmogenic (highlighted areas) and astrophysical (dashed lines) models of production. From [126]

are unstable particles when free, with a lifetime of ≈15 minutes in their rest frame. The mean decay path length for a neutron of energy E is easily visualizable as $l = 9.2\times$ (E/EeV) kpc. At the EeV, this means that the Galactic Center is within the mean decay length, and most of the Galactic disk is included in the decay horizon at higher energies. Neutron-induced showers are completely non-distinguishable from proton-induced ones, however, the presence of neutrons can be inferred if the distribution of events in the sky shows excesses of events in a given direction within a small angular scale, due to the fact that neutrons are not deflected by magnetic fields and point directly to their source. The search for such excesses has been performed in Auger with two approaches: a “blind” search, scanning the whole sky in the search for excesses [127], and a “targeted” one, performing a localized search in the direction of interesting catalogs of Galactic objects [128]. The latter allows for higher statistical significance since the trial penalization is lower. For the “targeted” search, known gamma-ray emitters in the GeV-TeV range were chosen as candidate sources: millisecond pulsars, magnetars, microquasars, X-ray binaries, as well as the Galactic Center, and the Galactic Plane. None of the two approaches found evidence for an EeV neutron flux, thus allowing us to put severe limits to such fluxes. The absence of detectable fluxes of EeV neutrons is one of the pieces of evidence of the extragalactic origin of UHECRs.

3.10.4 Large scale anisotropies in the arrival directions

With $\approx$10 degrees deflections for protons of 10 EeV predicted by models of the GMF, analyses of the large-scale structure of the arrival distribution are possible, aiming at the identification of possible deviations from an isotropic arrival distribution. Figure 3.27 is the result of such an analysis which investigated the presence of a dipolar structure in the observed UHECR arrival directions for events with energy above 8 EeV [56]. The direction of the dipole relating to maximal flux is indicated by the black cross and encircled by the 68% and 95% confidence intervals. This figure is shown in Galactic coordinates with the Galactic center at the origin. At a significance of 6.6σ [129], this is the first result in the ultra-high energy regime for which anisotropy has been observed. Further, the dipole direction at $100°$ in right ascension gives compelling evidence that above 8 EeV, cosmic rays have an extragalactic origin.

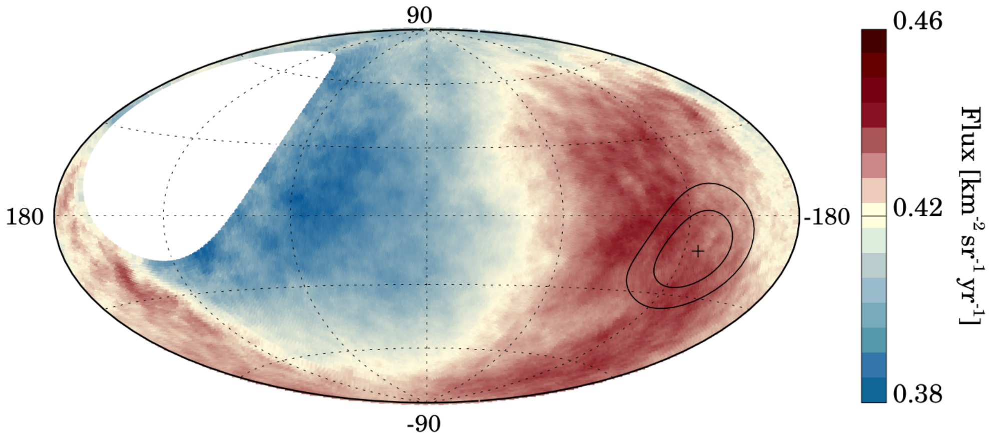

Figure 3.27: The large-scale distribution of cosmic rays above 8 EeV as observed by Auger. The fluxes of cosmic rays, smoothed by a 45° top-hat function, are shown above in Galactic coordinates. The direction of the dipole is shown by a black cross. The black lines enclose the 68% and 95% confidence intervals. From [56]

Chapter 4

The Auger Phase One dataset of highest-energy events

As detailed in the previous chapter, the Pierre Auger Observatory is in the final phases of a massive upgrade, AugerPrime, which brings new detectors, new and improved electronics, and changes in the methods of operation of existing parts of the array. AugerPrime will vastly modify the capabilities of the Observatory, introducing new information in the data and substantially changing the starting points in numerous science analyses in the fields of UHECR spectrum, mass composition, and anisotropy searches. As such the time before the upgrade is now labeled as *Auger Phase One*, or simply *Phase One*.

In this chapter the latest Phase One dataset of the highest-energy events recorded by the surface detector of the Observatory will be presented. The dataset is constructed specifically for arrival direction studies at the highest energies, and it was made available at the link `https://doi.org/10.5281/zenodo.6504276` together with the first publication using it [130], which will be discussed in detail in the next chapter.

The work described in this chapter has been performed as a member of the high energy flux distribution working group of the arrival directions task of the Pierre Auger Collaboration.

4.1 Event selection

Events recorded by the surface detector array are continuously archived in *raw* files containing all the relevant information in `.root` format. These events can then be reconstructed by the CDAS and OffLine software, with the procedures listed in the previous chapter, and generally made available to the Collaboration in a text archive containing all the physics information as well as reconstruction triggers and flags. For this work, I used the CDAS reconstruction. I selected events recorded from 1 January 2004 to 31 December 2020 with reconstructed energy above 32 EeV. The choice of an energy threshold at 32 EeV anticipates upcoming publications focused on lower energy bins. Different selection criteria were applied to *vertical* events, with zenith angle θ below 60°, and *inclined* events, with θ between 60° and 80°. These differences are due to the separate reconstruction techniques that these two subsets of events undergo. The procedures for reconstructing the energy and arrival directions of events recorded by the SD were described in detail in the previous chapter and in publications by the Collaboration such as [131] and [111].

Vertical events were included when the SD station with the largest signal is surrounded by at least four active stations, the condition called 4T5. The *a posteriori pos* requirement, i.e. that the reconstructed core of the shower lies within an elementary isosceles triangle of active stations, complements the *a priori* 4T5 condition. On the other hand, inclined events are chosen if the station nearest to the reconstructed core position is encircled by at least five active stations, the 5T5-inclined condition.

These specifications guarantee that the shower's footprint is completely contained within the array and that there is sufficient information for a precise reconstruction [110]. Note that the Pierre Auger Collaboration routinely uses a tighter selection in other analyses conducted at lower energy. For instance, the dataset used in the computation of the UHECR spectrum in [119] is compiled by requiring the operational status of all six stations surrounding the station with the strongest signal, the prime 6T5 condition. Due to the high-energy events featured here all having substantial footprints, with an average of 17.7 triggered stations, I was able to utilize a relaxed selection.

Each event was singularly inspected, and it was confirmed that even with inactive stations in the core region, the reconstruction was reliable. In comparison to earlier analyses, a better reconstruction has been made by improving the identification of active stations that were not triggered. This was accomplished by performing a *a posteriori* check on the consistency of the signal distribution at ground level. If a station is not triggered in an area of the array where the signal is greater than two times the full trigger efficiency, which occurs for 11 events in the data set, the station is categorized as inactive at the time of the event.

An effective technique for assessing the goodness of the reconstruction of an event is obtained by repeating the procedure after having manually removed one of the stations with a higher signal: in the case of a well-reconstructed event, the final inferred characteristics should not deviate much from the original ones, while if the event was misreconstructed they could oscillate wildly. By using this method, two *fake* events were excluded from the dataset.

If an event with θ close to $60°$ is present in both samples, I kept the version included in the inclined sample due to the more robust arrival direction reconstruction and angular resolution.

In order to prevent border effects at the zenith angle separating the inclined and vertical selections, I identified events in the $60° < \theta < 62°$ region that are well-reconstructed with the vertical procedure but not included in the inclined data set, and vice versa, events in the $58° < \theta < 60°$ region that are well-reconstructed with the inclined procedure but not included in the vertical data set. I identified one occurrence in the former case and none in the latter.

At all energies taken into consideration here, the angular resolution for both data sets measured as the 68 percent confinement radius, is better than $1°$. The energy calibration has a systematic uncertainty of $\approx 14\%$. while the energy resolution of the SD at the energies under consideration is $\approx 7\%$ [111].

4.2 Exposure calculation

The exposure can be computed in a geometrical way since we are operating above the energy threshold for full efficiency for both data samples (3EeV for vertical and 4 EeV for inclined). The geometrical exposure for the vertical events is computed each minute with a simple formula that depends on the number of active hexagons satisfying the 6T5, 5T5, and 4T5 conditions:

$$EXP = (N_{6T5} + N_{5T5} + 2/3 \times N_{4T5}) \times EXP_{unit}$$

in the case of a 4T5 selection, while

$$EXP = (N_{6T5} + 2/3 \times N_{4T5}) \times EXP_{unit}$$

for the 5T5 selection.
Where $EXP_{unit} = 4.59$ km^2 sr is the vertical exposure of the unitary cell. For the inclined exposure, the formula is corrected by multiplying the result by the geometrical factor $EXP_{inclined} = 0.29313$. The result is then integrated over the data-taking period. This results in 95,700 km^2 sr yr for the vertical sample and 26,300 km^2 sr yr for the inclined data set, for a total of 121,000 km^2 sr yr. I also computed the exposure accumulated at the moment of detection of each event, to display the evolution of the dataset over time. The previous formulae refer to the *integrated* exposure value over the whole sky, but how any number of detected cosmic rays are distributed on the sky depends on both the true celestial anisotropy and the observatory's *relative* exposure ω, which is a function of the declination. The relative exposure for a detector operating continuously at a single location may be determined as follows [132]. Full-time operation implies continual exposure in right ascension and no variance in sidereal time exposure. Let's assume that the detector is at latitude a_0 and fully efficient for particles arriving with zenith angles less than a certain maximum value θ_M. This causes the dependency on declination δ to be as follows:

$$\omega(\delta) \propto \cos(a_0)\cos(\delta)\sin(\alpha_M) + \alpha_M \sin(a_0)\sin(\delta)$$

where α_M is 0 if $\xi_M > 1$, π is $\xi_M < -1$ and $\cos^{-1}(\xi_M)$ otherwise, and

$$\xi_M = \frac{\cos(\theta_M) - \sin(a_0)\sin(\delta)}{\cos(a_0)\cos(\delta)}$$

This is the case for the vertical sample considered here. For the inclined sample, which has a maximum zenith angle θ_M but also a minimum angle θ_m, the formula is slightly more complicated:

$$\omega(\delta) \propto \cos(a_0)\cos(\delta)(\sin(\alpha_M) - \sin(\alpha_m)) + (\alpha_M - \alpha_m)\sin(a_0)\sin(\delta)$$

where α_M and α_m are obtained in the same way as previously described by evaluating the two parameters ξ_M and ξ_m.
In our case, the latitude of the Observatory is $a_0 = -35.2°$; the maximum

zenith angle for the vertical sample is $\theta_M, V = 60^\circ$, while for the inclined sample $\theta_m, V = 60^\circ$ and $\theta_M, V = 80^\circ$. To combine the two exposure functions, I normalized them to the number of events contained in their respective samples and added them. Figures 4.1 and 4.2 show the exposure plotted as a function of declination and projected in the sky in Galactic coordinates.

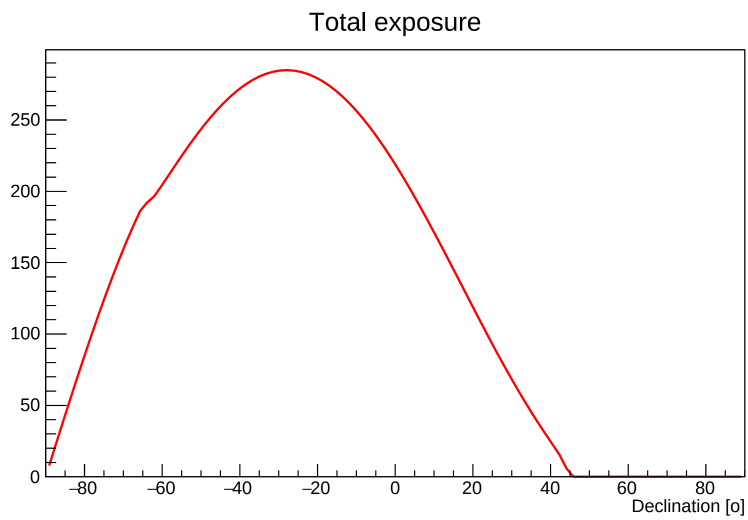

Figure 4.1: Combined exposure function in arbitrary units w.r.t the declination

4.3 The resulting dataset

The selection results in 2,040 events with $\theta < 60^\circ$ and 595 with $\theta \geq 60^\circ$ above 32 EeV.

The data set is formatted as shown in table 4.1, which features the twenty highest energy events for illustration. For each event, I report the year in which the event was detected, the Julian day of the year, and the exact time of detection expressed in UTC seconds. The arrival directions are expressed both in local coordinates, (θ, ϕ), which denote the zenith and azimuth angle, respectively, and in equatorial coordinates (J2000), (α, δ), which denote the right ascension (R.A.) and declination (Dec), respectively. Finally, the reconstructed energy, in EeV, and the integrated exposure accumulated up to the time of detection are reported in the last two columns. When compared to those already published in earlier works, such as [133], the energy and

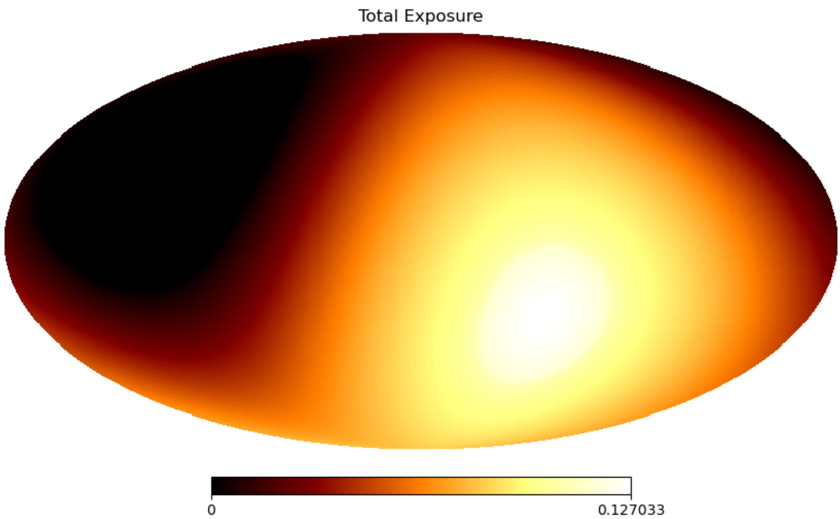

Figure 4.2: Combined exposure, normalized to 1, projected on the sky in Galactic coordinates.

arrival directions of the events may have changed due to the improved reconstruction, the main difference being the change in the CDAS-Herald software from a log-log parabola to the NKG function to fit the lateral distribution of data, as detailed in the previous chapter. These modifications result from revisions to the energy scale and calibration as well as improvements made to the reconstruction throughout time.

Year	JD	UTC (s)	θ (°)	ϕ (°)	R.A. (°)	Dec (°)	E (EeV)	Exposure (km^2 sr yr)
2019	**314**	**1573399408**	**58.6**	**-135.6**	**128.9**	**-52**	**167.7**	**111928.9**
2007	13	1168768186	14.2	85.6	192.9	-21.2	164.9	9784.9
2020	163	1591895321	18.9	-47.6	107.2	-47.6	155.5	116796.7
2014	293	1413885674	6.9	-155.4	102.9	-37.8	154.6	70647.4
2018	224	1534096475	47.9	141.7	125	-0.6	147.5	101397.8
2008	268	1222307719	49.8	140.5	287.8	1.6	141.1	21324.1
2019	117	1556436334	14.8	-32.6	275	-42.1	133.2	107370.7
2014	65	1394114269	58.5	47.3	340.6	12	132.3	65277.3
2017	361	1514425553	41.7	-30.5	107.8	-44.7	131.2	96084.6
2005	186	1120579594	57.3	155.7	45.8	-1.7	128.5	3117.6
2015	236	1440460829	20.1	-46.1	284.8	-48	124.4	77711.0
2008	18	1200700649	50.3	178.9	352.5	-20.8	124.4	16099.9
2016	26	1453874568	22.6	-14.6	175.6	-37.7	123	81177.2
2016	21	1453381745	13.8	-179.9	231.4	-34	122.5	81056.9
2011	26	1296108817	24.9	90.9	150.1	-10.4	116.6	39260.2
2016	68	1457496302	23.7	108.8	151.5	-12.6	115.8	82087
2015	**268**	**1443266386**	**77.2**	**-172**	**21.7**	**-13.8**	**113.3**	**78448.5**
2016	297	1477276760	49.5	104.5	352.1	13.2	111.7	86824.4
2020	66	1583535647	41.4	-20.5	133.6	-38.3	110.7	114595.1
2018	174	1529810463	42.7	4.3	300	-22.6	110.7	100244.0

Table 4.1: The twenty highest-energy events included in the dataset, displayed in the format with which they are published: Time of detection (Year, Julian day, UTC in seconds), local coordinates (zenith angle, azimuth angle), reconstructed arrival direction (right ascension and declination), energy, accumulated exposure at the time of detection. The highest energy events in the vertical and inclined subsamples are shown in bold.

The two most energetic events in each sample, shown in bold in 4.1, are described in more detail in figures 4.3 and 4.4. For each event, the figures show the ground array view, the footprint on the ground of the shower plane, the traces of the two SD stations with the highest signal, the LDF plot, and the time residuals. All the elements in this description are available for these two events in the Open Data Catalog of the 100 highest energy events recorded by Auger Phase One[1]. More details on these 100 events, which are all included in the dataset used here, can be found in [134].

The compatibility between the two independent vertical and inclined samples was checked by comparing the ratio of the number of events in the vertical and inclined samples:

$$N_{\text{incl}}/N_{\text{vert}} = 0.292 \pm 0.014$$

and the value predicted from the ratio of geometrical exposures, which takes into account the finite energy resolution of each data stream:

$$\frac{\omega_{\text{incl}}/c_{\text{incl}}(\geq 32\,\text{EeV})}{\omega_{\text{vert}}/c_{\text{vert}}(\geq 32\,\text{EeV})} = 0.278$$

Here ω is the geometrical exposure for each data set, which is independent of energy, and $c(\geq 32\,\text{EeV})$ represents the net spillover of events from low to higher energies; this is an effect due to the much higher probability of overestimating rather than underestimating the energy due to the steeply inclined spectrum.
The event- and exposure-computed ratios are consistent at the 1σ C.L., demonstrating the compatibility of the vertical and inclined samples. When in the following analyses simulated data sets were generated above any energy threshold, I used the ratio of events seen above 32 EeV as the expected exposure ratio in order to keep the analysis as data-driven as possible.
However, we noticed an energy dependence in the ratio of the number of inclined and vertical events. At the highest threshold considered in the analyses, i.e. 80 EeV, 10 events with $\theta > 60^\circ$ are found and 86 are found with $\theta < 60^\circ$, which corresponds to a ratio of

$$N_{\text{incl}}/N_{\text{vert}} = 0.116 \pm 0.039$$

[1] https://opendata.auger.org/catalog/

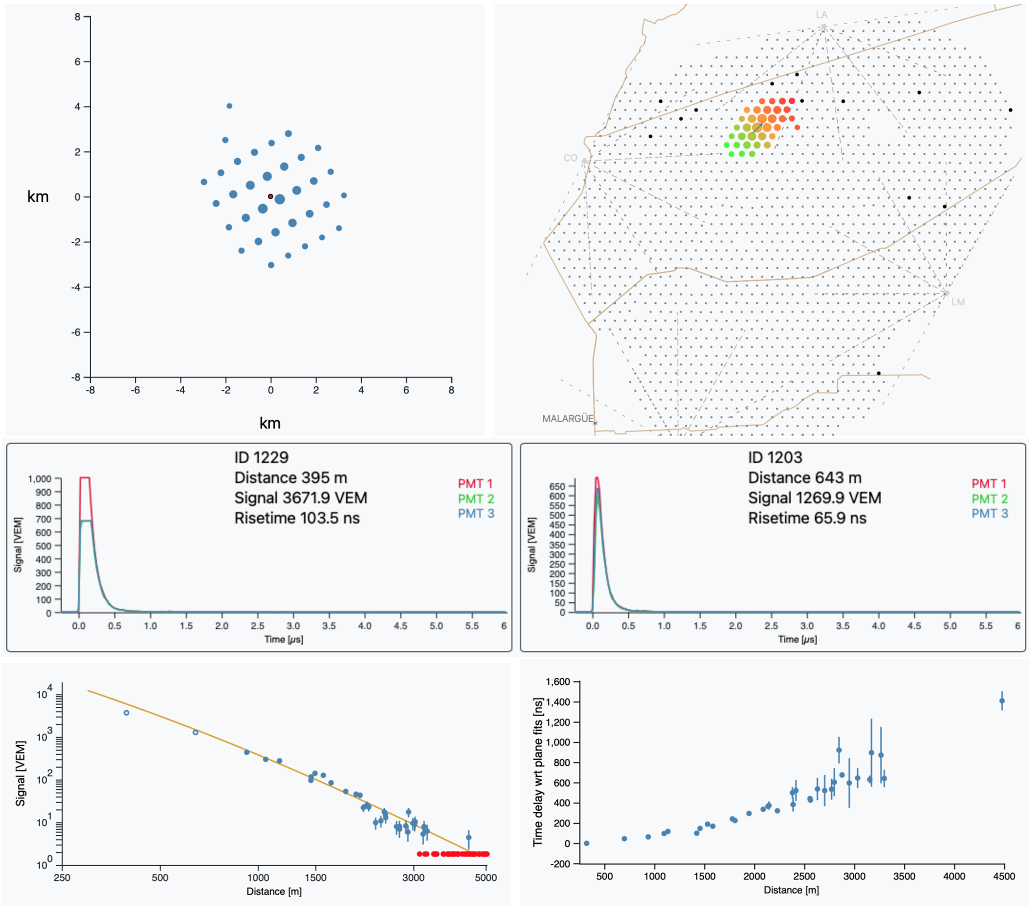

Figure 4.3: Plots describing the highest-energy vertical event recorded in Phase One. Top panel, left: footprint on the ground array, with larger circles representing stations with more signal. Top panel, right: view of the SD, with triggered stations colored from green to red representing early and late triggers. Middle panel: signal traces in all 3 PMTs of the two SD stations with the most signal. Bottom panel left: LDF functions and signal in the tanks ordered by distance from the reconstructed shower core (non-triggered stations in red). Bottom panel right: time residuals of the stations ordered by distance from the reconstructed shower core.

When penalized for a search as a function of energy, the deficit of inclined events is most significant above 90 EeV, which yields a post-trial significance (under the assumption of isotropy) at the level of 2.5 σ. We cannot rule out that the observed deficit is due to a statistical fluctuation in the number of

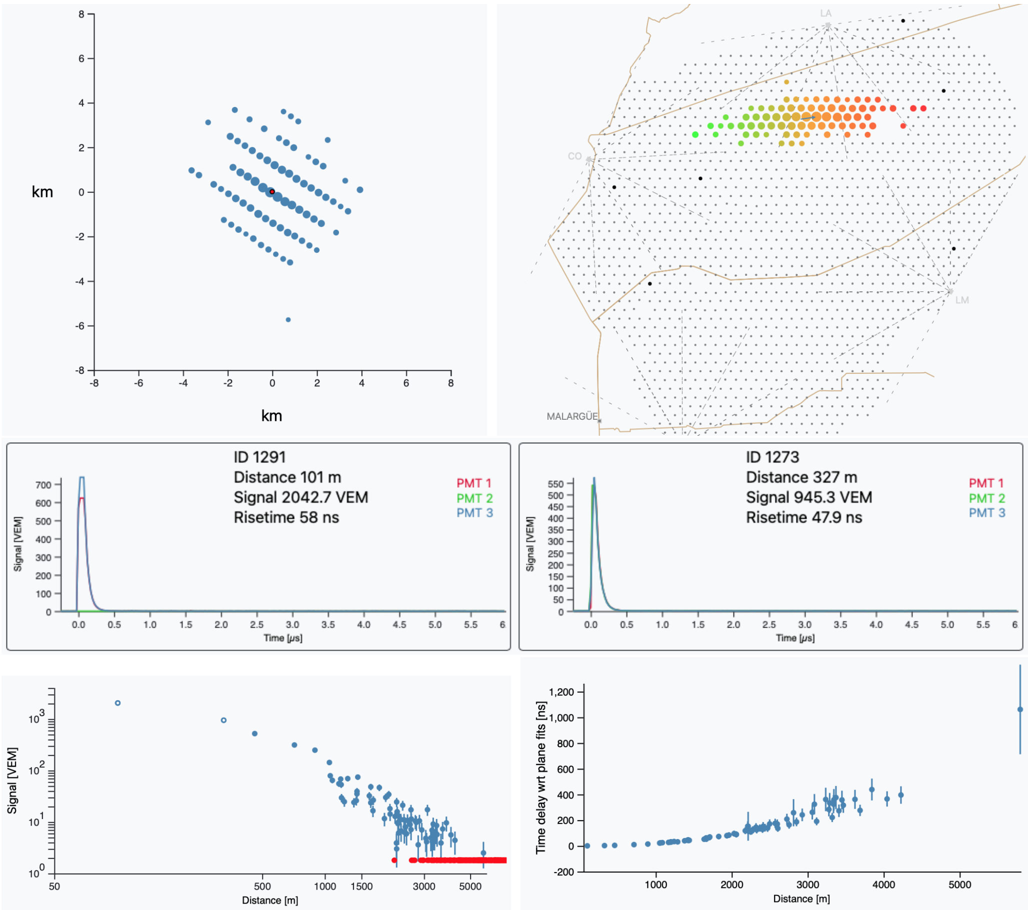

Figure 4.4: Plots describing the highest-energy inclined event recorded in Phase One. Top panel, left: footprint on the ground array, with larger circles representing stations with more signal. Top panel, right: view of the SD, with triggered stations colored from green to red representing early and late triggers. Middle panel: signal traces in all 3 PMTs of the two SD stations with the most signal. Bottom panel left: LDF functions and signal in the tanks ordered by distance from the reconstructed shower core (non-triggered stations in red). Bottom panel right: time residuals of the stations ordered by distance from the reconstructed shower core.

occurrences in each of the two data streams, as the local significance over the search range (32-80 EeV) does not surpass 2σ.

The following are a few plots showing the distribution of data in reconstructed arrival direction (R.A., Dec) in figure 4.5, zenith angle in figure 4.6, the azimuth angle in figure 4.7, energy in figure 4.8 and time in figure 4.9.

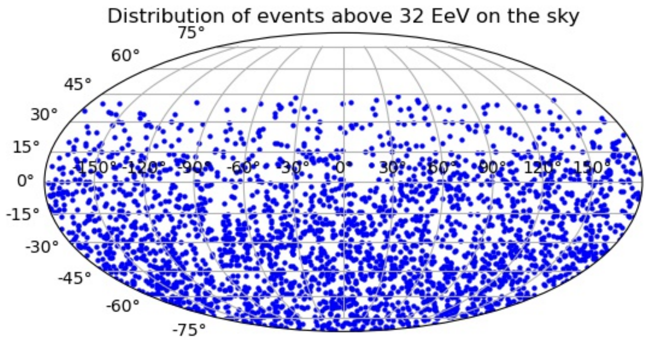

Figure 4.5: Distribution of the events in the sky in equatorial coordinates.

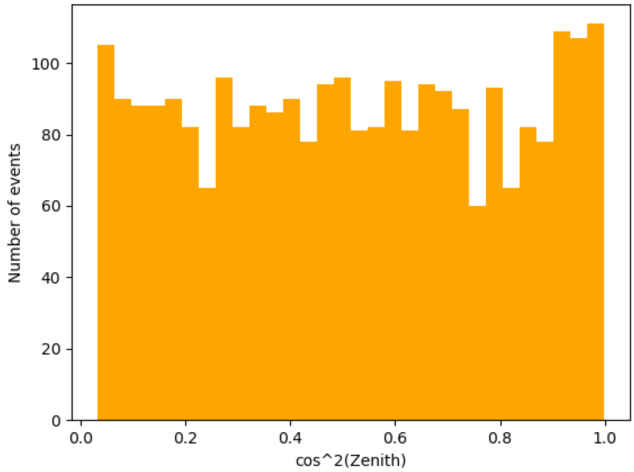

Figure 4.6: Distribution of the events in $\cos^2(\theta)$.

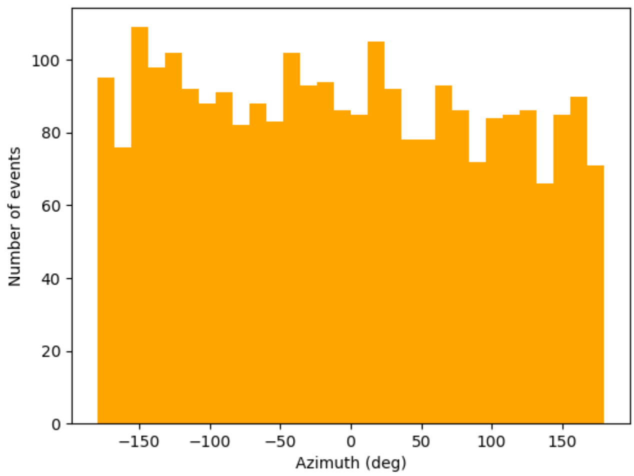

Figure 4.7: Distribution of the events in azimuth angle ϕ, showing the expected uniform distribution.

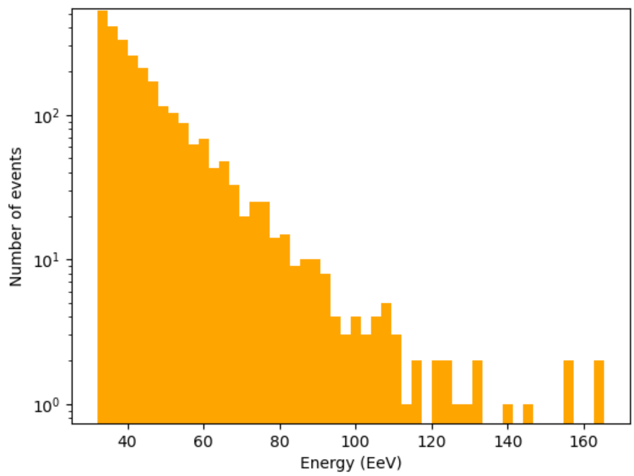

Figure 4.8: Distribution of the events in energy. The logarithmic scale on the y-axis clearly shows the power-law distribution.

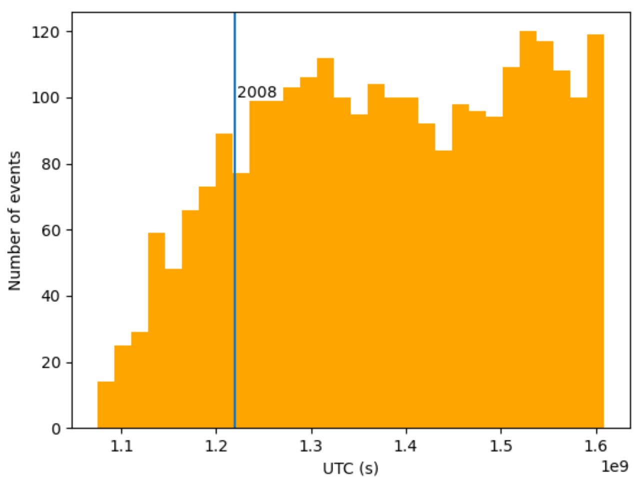

Figure 4.9: Distribution of the events in time. The increasing exposure in the first phase of data taking, while the Observatory was being completed, is visible together with the plateau in the distribution after the completion of the SD in 2008, shown as a blue vertical line.

Another intuitive visualization of the distribution of events in the sky is displayed in figure 4.10, a flux map computed with the events above 32 EeV in circular windows of top-hat smoothing radius $\Psi = 25°$.

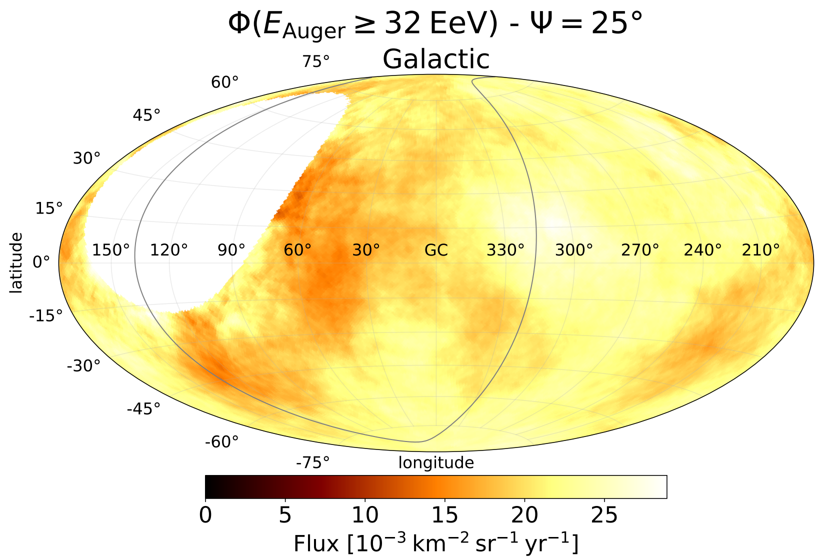

Figure 4.10: Flux map at energies above 32 EeV with a top-hat smoothing radius $\Psi = 25°$ in Galactic coordinates. The supergalactic plane is shown as a gray line. The blank area is outside the field of view of the Pierre Auger Observatory

Chapter 5

Searches for intermediate and small scale anisotropies at the highest energies

As presented in the previous chapters, since they are almost all charged particles and are therefore deflected by the magnetic fields permeating the interstellar, intra-halo, and intergalactic media [135], the search for the sources of ultra-high energy cosmic rays (UHECRs) with energies exceeding a few EeV is difficult. These magnetic fields are challenging to investigate, and our understanding of them through modeling and observation of their tracers is incomplete. However, at a few tens of EeV, the deflections might be negligible enough for cosmic rays to continue carrying some directional information about the location of their sources, at least for those with a charge that is small enough [136]. Previous results from the Pierre Auger Observatory, also reported in previous chapters, limit the cosmological volume in which the sources of UHECRs must be searched: the dipolar structure observed in the large-scale distribution of events with energy above 8 EeV points to an extragalactic origin [137], while the reported *cut-off* of the UHECR spectrum at the highest energy is a possible confirmation of propagation effects, such as the GZK effect, that constrain the distance of the sources inside a bubble of the local universe.

Using the unprecedentedly large UHECR dataset collected by the Pierre Auger Observatory during its Phase One and described in the previous chapter, we updated previous searches [133][138] for intermediate scale anisotropies on the sky at the highest energies. By comparing the expected and observed numbers of events within the window, searches for localized excesses in top-hat windows of angular radius Ψ across the entire field of view of the Observatory, or around the Galactic center, Centaurus A. Similar investigations along the Galactic and supergalactic planes were carried out by counting the number of events that were within angular distance Ψ from these structures, and an autocorrelation analysis took use of the number of pairs of events that were Ψ apart. Additionally, a likelihood-ratio test of correlation between the dataset and catalogs of candidate sources was distilled from multi-wavelength surveys of galaxies. The methods employed in these analyses and the obtained results are reported in the following sections.

A preliminary update of the searches for neutral particle-induced small-scale anisotropies is also offered, by correlating the arrival directions of events with energy above 0.1 EeV to catalogs of Galactic objects. This update uses a new and improved dataset, comprising vertical events but also for the first time for this analysis, inclined events and events from the infill array; moreover, a new method for correlating events and objects will be presented. The results discussed here are also made public in [130], together with the dataset used for the analyses, which was discussed in the previous chapter, and the code to reproduce the results, available at `https://doi.org/10.5281/zenodo.6504276`.

The work described in this chapter has been performed as a member of the high energy flux distribution working group of the arrival directions task of the Pierre Auger Collaboration.

5.1 Search for localized excesses and correlation with structures

This section is a report of the results from the search for localized excesses, the autocorrelation analysis, and the searches for excesses around relevant structures in the Galaxy and local universe, in particular the Galactic center, Galactic plane, and supergalactic plane. All the analyses were repeated above energy thresholds ranging from 32 to 80 EeV in 1 EeV step.

5.1.1 Search for localized excesses

The first study presented is a blind search for excesses over the portion of the sky visible to the Observatory. The number of UHECRs observed in circular sky windows (N_{obs}) is compared to the number of UHECRs predicted by an isotropic distribution of events (N_{exp}) for the same window. The radius Ψ of the search windows is varied, ranging from 1° to 30° in 1° steps. To perform

the search in a rational way over the whole sky, I employed a `HEALPix` grid [139], with parameter `nSide` = 64, which determines the size of the pixels to be of the order of the Observatory's angular resolution, of O(1°). The search windows were centered on each pixel.
I calculated the binomial probability of randomly receiving N_{obs} or more events from an isotropic data distribution for each angular window and energy threshold. N_{exp} is obtained by simulating events with coordinates distributed in accordance with the sum of the vertical and inclined exposures, weighted in proportion to the observed number of events at energies over 32 EeV. The number of events is the same as what is observed over the field of view for each realization of the simulated data collection. Having obtained the *local* p-value in this way, I had to consider the trial factors needed to account for the *look elsewhere effect* that arises from having tested different directions, radii, and energy thresholds. To do so, I repeated the whole analysis on a set of simulated datasets, considering as *post-trial* p-value the fraction of these with a local p-value equal or lower than the best one obtained with the observed dataset.
The most significant excess for this analysis, with 5.4σ local significance, is found at $(\alpha, \delta) = (196.3°, -46.6°)$, corresponding to Galactic coordinates $(l, b) = (305.4°, 16.2°)$, at an energy threshold $E_{th} = 41$ EeV and top-hat radius $\Psi = 24°$. In this parameter space point, 153 events are observed while 97.7 are expected from isotropy. The local p-value is 3.7×10^{-8}, resulting in a global p-value of 0.03.
I also computed the local Li-Ma significance [140] for each point in the sky, which is defined as

$$S = \sqrt{2}\left(N_{on} \ln \frac{1+\alpha}{\alpha}\left(\frac{N_{on}}{N_{on}+N_{off}}\right) + N_{off} \ln\left(1+\alpha\right)\left(\frac{N_{off}}{N_{on}+N_{off}}\right)\right)^{1/2}$$

in which the ψ-sized top-hat disk centered on each pixel of the `HEALPix` grid was considered the ON region and the rest of the field of view the OFF region and α is defined as the ratio between the exposure in the ON region and the OFF region. The significance map is visible in figure 5.1.

5.1.2 Autocorrelation

The search for autocorrelation consists in counting the pairs of events separated by a given angular distance. It is another model-independent approach

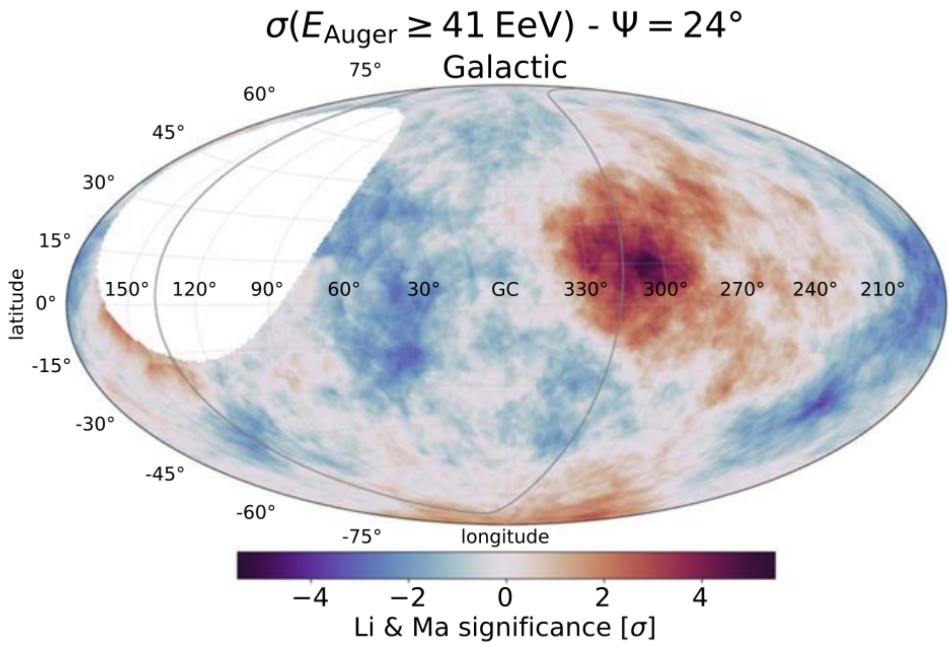

Figure 5.1: Local Li–Ma significance map at energies above 41 EeV and within a top-hat search angle of $\psi = 24°$ in Galactic coordinates. The supergalactic plane is shown in grey. The white area indicates the portion of the sky not visible to the Observatory.

to searching for clusters of events and of assessing the typical clustering angular size for a data set. It is a robust analysis in the case of multiple areas in the sky of similar size containing clusters of events.

I report the results of the count of observed event pairs N_{obs}, above energy thresholds ranging from 32 to 80 EeV, with the events in the pair separated by an angular distance ψ; the parameter ψ was scanned from 1° to 30° with steps of 0.25° up to 5°, and steps of 1° above. The distribution of the expected number of pairs N_{exp} was obtained by performing the same analysis on simulated isotropic data sets of the same size as the observed one. For each E_{th} and ψ combination, the local p-value was obtained as the fraction of simulated data sets for which $N_{exp} \geq N_{obs}$. The global post-trial p-value is obtained in the same way as the blind search. The most significant point in parameter space is found at $E_{th} = 62$, $\psi = 3.75°$, where 93 pairs are observed while 66.4 are expected from isotropy, for a local p-value of 2.5×10^{-3} corresponding to a global significance of 0.24.

5.1.3 Correlation with structures

Results from the searches for large-scale anisotropies by the Collaboration decidedly disfavor a Galactic origin for UHECRs with energies above 8 EeV, as reported in section 3.10.4. However, along with the search for an excess in the vicinity of the supergalactic plane, I performed a similar search for the Galactic plane and Galactic center, with the intent of updating previous publications by the Collaboration [133]. The analysis is conducted in a similar way to the previous section, with N_{obs} and N_{exp}, in this case, being the number of observed and expected events within an angle ψ from the structure. For the Galactic and supergalactic plane this translates into selecting events with latitude smaller than ψ in the respective coordinate system, the Galactic and the supergalactic, while for the Galactic center, the search is conducted in the same way as for each pixel of the previously discussed search for localized excesses. The most significant excess is found for angles $\psi \geq 20°$ for all three structures. Detailed results are in table 5.1, where the result from the autocorrelation analysis is also reported for comparison. No significant departures from isotropy are found.

Search	$E_{\rm th}$ [EeV]	Angle, Ψ [deg]	$N_{\rm obs}$	$N_{\rm exp}$	Local p-value, $f_{\rm min}$	Post-trial p-value
Autocorrelation	62	3.75	93	66.4	2.5×10^{-3}	0.24
Supergalactic plane	44	20	394	349.1	1.8×10^{-3}	0.13
Galactic plane	58	20	151	129.8	1.4×10^{-2}	0.44
Galactic center	63	18	17	10.1	2.6×10^{-2}	0.57

Table 5.1: The results of the search for autocorrelation and correlation with astrophysical structures. The energy threshold, $E_{\rm th}$, and the search angle, Ψ, minimize the local p-value, based on the number of observed and expected events/pairs. The post-trial p-value accounts for the scan in energy threshold and search angle, Ψ.

5.2 Likelihood analysis with catalogs of candidate host galaxies

In [133] the Collaboration performed a cross-correlation study between high energy events and three flux-limited catalogs of galaxies: the 2MASS Redshift Survey of near-infrared galaxies [141], the hard X-ray *Swift*-BAT 70-month catalog of AGNs [142] and a catalog of radio-emitting galaxies [143].

While that publication followed a *standard candle approach* by presuming that all galaxies under study have the same weight, this was successively considered a limitation and updated in the subsequent paper [138] through a likelihood-ratio test, which took into account the UHECR flux's inverse-square law or its attenuation due to energy losses brought on by propagation. In the same publication, two more catalogs based on Fermi-LAT gamma-ray data were also evaluated. Star-forming galaxies and jetted AGNs are the primary sources of the extragalactic gamma-ray background at GeV energy, according to the Fermi-LAT full-sky gamma-ray survey, however, their relative contributions are still unknown [144][145].

5.2.1 Galaxy catalogs

In the following a description of the four galaxy catalogs used for updating past publications is presented. The final catalogs (or excerpts in the case of long samples) are shown in tables 5.2, 5.3, 5.4 and 5.5.

Near infrared

We started by looking for correlations with the large-scale distribution of matter using the Two Micron All-Sky Survey [146]. With this scenario, we suppose that the UHECR luminosity is proportional to star mass, and the expected UHECR flux is traced by infrared K-band measurements at 2.16 μm. We only include galaxies with a K-band brightness of up to 11.75 mag in the analysis, which matches the flux limit for more than 90% of the 2MASS Redshift Survey. We confirmed that all of the selected objects are galaxies using the HyperLEDA database[1][147]. It is to be noted that AGNs were kept in the final sample even though their infrared emission is likely to be contaminated by non-thermal emission. More than 40000 objects are contained in the final catalog.

Radio and far infrared

A sample of *starburst* galaxies, i.e. galaxies with a very high star formation rate was distilled from the Lunardini-19 catalog of local objects [148], which

[1] `http://leda.univ-lyon1.fr/`

already is a synthesis of the IRAS all-sky survey in the far infrared [149], flux-limited to objects brighter than 60 Jy at 60 μm, with the NVSS [150] and Parkes surveys [151] in radio, limited to objects brighter than 20 mJy at 1.4 GHz. We further eliminated objects by imposing the ratio between far infrared and radio emission to be between 30 and 1000, eliminating jetted AGNs and dwarf galaxies; in particular the Magellanic Clouds are clear outliers in the flux distribution. Furthermore, we added the Circinus galaxy, which, being at Galactic latitude $-3.8°$, was excluded from the original sample by Lunardini et al. together with all the areas close to the Galactic plane. This galaxy satisfies all the selection conditions for being added to the sample, and it is added to it using the flux tabulated in the 1996 Parkes catalog [152]. In this case, UHECR luminosity is thought to be proportional to the star-forming rate of the galaxy, giving UHECR emission traced by the measured radio flux. The final catalog contains 44 galaxies.

Hard X-rays

Observations in hard X-rays with the Swift-BAT satellite compiled in their 105 months catalog [153] provided a tracer for AGN activity in general. Sources with a flux in the 14-195 keV band larger than 8.4×10^{-12} erg cm^{-2} s^{-1} were selected. All objects identified as AGNs, be they jetted, non-jetted, Seyferts, or other species of Active Galaxies, were retained from the sample. We assumed that in this scenario the UHECR luminosity would be driven by accretion onto supermassive black holes, taking the X-ray flux as a direct tracer of the UHECR flux. However, it has to be taken into account that the hard X-ray flux in jetted AGNs such as blazars is thought to be dominated by jet activity rather than by accretion. The final catalog contains 523 galaxies.

Gamma rays

A second AGN sample contained only the γ-ray selected galaxies as observed by the Fermi-LAT instrument and tabulated in the 3FHL catalog [154]. We selected radio galaxies and jetted AGNs with integral flux larger than 3.3×10^{-11} cm^{-2} s^{-1} in the 10 GeV - 1 TeV band. Above this value, the 3FHL catalog is flux-limited over 90% of the sky (97% for Galactic latitudes

$|b| > 5°$). In this case, the UHECR emission is supposed to be proportional to the γ emission in the jets protruding from the central black hole of the galaxies. The final catalog contains 26 galaxies.

PGC	Counterpart	Object Type	R.A. °	Dec °	$(m-M)$ mag	$\sigma(m-M)$ mag	d_{L} Mpc	$\sigma(d_{\mathrm{L}})/d_{\mathrm{L}}$	$\mathrm{K_t}$ mag	$\sigma(\mathrm{K_t})$ mag
29128	NGC3109	G	150.78	-26.16	25.56	0.02	1.29	0.007	9.57	0.4
29653	PGC029653	G	152.75	-4.69	25.59	0.03	1.31	0.013	11.31	0.56
28913	UGC05373	G	150.0	5.33	25.79	0.01	1.44	0.006	10.76	0.23
100169	PGC100169	G	31.52	69.0	26.15	0.2	1.7	0.092	9.69	0.24
67908	IC5152	G	330.67	-51.3	26.46	0.03	1.96	0.012	9.05	0.36
3238	NGC0300	G	13.72	-37.68	26.53	0.02	2.03	0.007	6.58	0.36
1014	NGC0055	G	3.72	-39.2	26.62	0.01	2.11	0.006	6.34	0.18
9140	PGC009140	G	36.18	-73.51	26.63	0.07	2.12	0.032	10.83	0.1
13115	UGC02773	G	53.03	47.79	26.69	0.2	2.18	0.092	9.8	0.1
39573	IC3104	G	184.69	-79.73	26.86	0.02	2.36	0.007	9.24	0.14
60849	IC4662	G	266.79	-64.64	27.03	0.01	2.55	0.006	9.45	0.21
47495	UGC08508	G	202.68	54.91	27.07	0.02	2.6	0.011	11.51	0.1
40904	UGC07577	G	186.92	43.5	27.08	0.02	2.6	0.011	10.45	0.2
54392	ESO274-001	G	228.56	-46.81	27.24	0.06	2.8	0.026	8.3	0.39
51472	UGC09240	G	216.18	44.53	27.25	0.02	2.82	0.008	10.89	0.13
39023	NGC4190	G	183.44	36.63	27.26	0.04	2.83	0.02	11.4	0.77
14241	PGC014241	G	59.96	67.14	27.37	0.03	2.98	0.012	8.24	0.16
4126	NGC0404	G	17.36	35.72	27.37	0.02	2.98	0.007	7.53	0.02
39225	NGC4214	G	183.91	36.33	27.37	0.01	2.98	0.002	8.09	0.21
38881	NGC4163	G	183.04	36.17	27.38	0.02	2.99	0.007	10.92	0.08
15488	NGC1560	G	68.2	71.88	27.38	0.1	2.99	0.046	9.07	0.22
49050	ESO383-087	G	207.32	-36.06	27.52	0.02	3.19	0.007	9.91	0.14
15439	PGC015439	G	68.01	63.62	27.53	0.05	3.2	0.024	10.97	0.17
21396	NGC2403	G	114.21	65.6	27.53	0.01	3.2	0.004	6.24	0.14
47762	NGC5206	G	203.43	-48.15	27.53	0.01	3.21	0.005	8.39	0.25
...	...	...	...	...	...	...	...	...	...	...
127001	PGC127001	G	67.39	-61.25	36.99	0.07	249.7	0.03	11.72	0.18

Table 5.2: Galaxies (2MASS(K<11.75) × HyperLEDA)44,113 entries within 250 Mpc. 17,143 entries at $d_{\mathrm{L}} <$ 100 Mpc, 39,563 at $d_{\mathrm{L}} < 200$ Mpc.

Lunardi Name	Counterpart	Host Type	R.A. °	Dec °	$(m-M)$ mag	$\sigma(m-M)$ mag	d_L Mpc	$0\sigma(d_\mathrm{L})/d_\mathrm{L}$	$\Phi(1.4\,\mathrm{GHz})$ Jy	flag: in Aab+ '18? (No/Yes/Xcheck)
NGC0055	NGC0055	SBm	3.72	-39.2	26.62	0.01	2.11	0.005	0.37	N
NGC1569	NGC1569	IB	67.7	64.85	27.53	0.05	3.21	0.023	0.4	X
NGC2403	NGC2403	SABc	114.21	65.6	27.53	0.01	3.21	0.005	0.39	X
IC342	IC342	SABc	56.7	68.1	27.68	0.03	3.44	0.014	2.25	Y
NGC4945	NGC4945	Sbc	196.37	-49.47	27.7	0.02	3.47	0.009	6.6	Y
NGC3034(M82)	M82	S?	148.97	69.68	27.79	0.01	3.61	0.005	7.29	Y
NGC0253	NGC253	SABc	11.89	-25.29	27.84	0.02	3.7	0.009	6.0	Y
N/A	Circinus	Sb	213.29	-65.34	28.12	0.36	4.21	0.166	1.5	Y
NGC5236(M83)	M83	Sc	204.25	-29.87	28.45	0.02	4.9	0.009	2.44	Y
Maffei2	Maffei2	Sbc	40.48	59.6	28.79	0.12	5.73	0.055	1.01	X
NGC6946	NGC6946	SABc	308.72	60.15	29.14	0.05	6.73	0.023	1.4	Y
NGC4631	NGC4631	SBcd	190.53	32.54	29.33	0.02	7.35	0.009	1.12	Y
NGC5194(M51)	M51	SABb	202.48	47.2	29.67	0.02	8.59	0.009	1.31	Y
NGC5055(M63)	NGC5055	Sbc	198.96	42.03	29.78	0.01	9.04	0.005	0.35	Y
NGC2903	NGC2903	Sbc	143.04	21.5	29.85	0.11	9.33	0.051	0.44	Y
NGC891	NGC891	Sb	35.64	42.35	29.94	1.72	9.73	0.792	0.7	Y
NGC1068	NGC1068	Sb	40.66	0.0	30.12	0.34	10.6	0.157	4.85	Y
NGC3628	NGC3628	SBb	170.07	13.59	30.21	0.34	11.0	0.157	0.47	Y
NGC4818	NGC4818	SABa	194.2	-8.53	30.27	0.33	11.3	0.152	0.45	N
NGC3627	NGC3627	Sb	170.06	12.99	30.3	0.04	11.5	0.018	0.46	Y
NGC1808	NGC1808	Sa	76.93	-37.51	30.45	0.36	12.3	0.166	0.5	X
NGC4303	M61	Sbc	185.48	4.47	30.45	0.1	12.3	0.046	0.44	X
NGC3521	NGC3521	SABb	166.45	-0.04	30.47	0.29	12.4	0.134	0.35	N
NGC0660	NGC660	Sa	25.76	13.65	30.5	1.31	12.6	0.603	0.37	Y
NGC4254	NGC4254	Sc	184.71	14.42	30.77	1.13	14.3	0.52	0.37	N
...	...	...	...	...	...	...	...	...	...	...
NGC6240	NGC6240	S0-a	253.26	2.4	35.18	0.15	108.6	0.069	0.65	Y

Table 5.3: Starburst galaxies (Lunardini+ '19). 44 entries within 250 Mpc. 43 entries at $d_\mathrm{L} < 100$ Mpc, 44 at $d_\mathrm{L} < 200$ Mpc.

BAT105 Name	Counterpart	AGN Type	R.A.	Dec	$(m-M)$	$\sigma(m-M)$	$d_{\rm L}$	$\sigma(d_{\rm L})/d_{\rm L}$	$\Phi(14-195\,{\rm keV})$
			$^\circ$	$^\circ$	mag	mag	Mpc		$10^{-12}\,{\rm erg\,cm^{-2}\,s^{-1}}$
J1305.4-4928	NGC4945	Sy2	196.37	-49.47	27.7	0.02	3.47	0.009	282.1
J0955.5+6907	M81	Sy1.9	148.94	69.06	27.78	0.01	3.6	0.005	20.3
J1325.4-4301	CenA	BeamedAGN	201.37	-43.02	27.83	0.03	3.68	0.014	1346.3
J1412.9-6522	Circinus	Sy2	213.29	-65.34	28.12	0.36	4.21	0.166	273.2
J1210.5+3924	NGC4151	Sy1.5	182.64	39.41	28.39	1.65	4.76	0.76	618.9
J1202.5+3332	NGC4395	Sy2	186.45	33.53	28.39	0.01	4.76	0.005	27.5
J0420.0-5457	NGC1566	Sy1.5	64.96	-54.94	29.13	1.16	6.7	0.534	19.5
J1219.4+4720	M106	Sy1.9	184.75	47.29	29.41	0.01	7.62	0.005	23.0
J1329.9+4719	M51	Sy2	202.48	47.2	29.67	0.02	8.59	0.009	13.3
J0242.6+0000	NGC1068	Sy1.9	40.66	0.0	30.12	0.34	10.6	0.157	37.9
J1717.1-6249	NGC6300	Sy2	259.25	-62.83	30.15	0.09	10.7	0.041	96.4
J1203.0+4433	NGC4051	Sy1.5	180.78	44.52	30.28	0.35	11.4	0.161	42.5
J1652.0-5915B	NGC6221	Sy2	253.18	-59.23	30.34	0.62	11.7	0.286	22.4
J1209.4+4340	NGC4138	Sy2	182.35	43.7	30.7	0.25	13.8	0.115	24.4
J1157.8+5529	NGC3998	Sy1.9	179.46	55.44	30.73	0.19	14.0	0.087	13.2
J2235.9-2602	NGC7314	Sy1.9	338.95	-26.05	31.03	0.25	16.1	0.115	57.4
J1432.8-4412	NGC5643	Sy2	218.19	-44.15	31.03	1.0	16.1	0.461	16.8
J1001.7+5543	NGC3079	Sy2	150.46	55.67	31.16	0.32	17.1	0.147	36.7
J1341.9+3537	NGC5273	Sy1.5	205.47	35.66	31.16	0.12	17.1	0.055	16.0
J1207.8+4311	NGC4117	Sy2	181.95	43.12	31.18	0.94	17.2	0.433	12.9
J0333.6-3607	NGC1365	Sy2	53.39	-36.14	31.19	0.02	17.3	0.009	63.5
J0241.3-0816	NGC1052	BeamedAGN	40.29	-8.24	31.22	0.11	17.5	0.051	31.4
J1132.7+5301	NGC3718	Sy1.9	173.22	53.02	31.25	0.89	17.8	0.41	12.2
J1206.2+5243	NGC4102	Sy2	181.59	52.71	31.29	0.25	18.1	0.115	32.1
J2318.4-4223	NGC7582	Sy2	349.6	-42.37	31.41	0.1	19.1	0.046	82.3
...	...	...	...	...	...	...	...	...	...
J0534.8-6026	2MASXJ05343093-6016153	Sy1	83.7	-60.27	36.98	0.06	248.9	0.028	10.7

Table 5.4: Jetted and non-jetted AGNs (*Swift*-BAT 105 months). 523 entries within 250 Mpc. 201 entries at $d_{\rm L} < 100$ Mpc, 458 at $d_{\rm L} < 200$ Mpc.

3FHL Name	Counterpart	Jetted AGN Type	R.A.	Dec	$(m-M)$	$\sigma(m-M)$	$d_{\rm L}$	$\sigma(d_{\rm L})/d_{\rm L}$	$\Phi(0.01-1\,{\rm TeV})$	$\sigma(\Phi)$	flag: in Aab+ '18?
			$^\circ$	$^\circ$	mag	mag	Mpc		10^{-10} cm^{-2} s^{-1}	10^{-10} cm^{-2} s^{-1}	(No/Yes)
J1325.5-4300	CenA	RDG	201.37	-43.02	27.83	0.03	3.68	0.014	1.54	0.25	Y
J1230.8+1223	M87	RDG	187.71	12.39	31.12	0.06	16.7	0.028	0.98	0.2	Y
J0322.6-3712e	FornaxA	RDG	50.67	-37.21	31.55	0.03	20.4	0.014	0.48	0.16	N
J1346.2-6026	CenB	RDG	206.7	-60.41	33.71	0.29	55.2	0.134	0.64	0.18	N
J0319.8+4130	NGC1275	RDG	49.95	41.51	34.46	0.08	78.0	0.037	14.17	0.67	Y
J0316.6+4120	IC310	RDG	49.18	41.32	34.6	0.19	83.2	0.087	0.43	0.13	Y
J0153.5+7115	TXS0149+710	BCU	28.36	71.25	35.07	0.15	103.3	0.069	0.44	0.12	Y
J0308.4+0408	NGC1218	RDG	47.11	4.11	35.48	0.13	124.7	0.06	0.54	0.16	N
J1104.4+3812	Mkn421	BLL	166.1	38.21	35.63	0.12	133.7	0.055	59.35	1.38	Y
J1653.8+3945	Mkn501	BLL	253.47	39.76	35.91	0.1	152.1	0.046	19.17	0.76	Y
J0131.1+5546	TXS0128+554	BCU	22.81	55.75	36.06	0.1	162.9	0.046	0.33	0.12	N
J1543.6+0452	CGCG050-083	BCU	235.89	4.87	36.26	0.09	178.6	0.041	0.69	0.17	N
J0223.0-1119	1RXSJ022314.6-111741	BLL	35.81	-11.29	36.31	0.09	182.8	0.041	0.4	0.13	N
J2347.0+5142	1ES2344+514	BLL	356.76	51.69	36.47	0.08	196.8	0.037	3.32	0.31	Y
J0816.4-1311	PMNJ0816-1311	BLL	124.11	-13.2	36.51	0.08	200.4	0.037	2.71	0.33	N
J1136.5+7009	Mkn180	BLL	174.11	70.16	36.54	0.08	203.2	0.037	1.74	0.21	Y
J1959.9+6508	1ES1959+650	BLL	299.97	65.16	36.63	0.08	211.8	0.037	8.43	0.46	Y
J1647.6+4950	SBS1646+499	BLL	251.9	49.83	36.64	0.08	212.8	0.037	0.48	0.12	N
J1517.6-2422	APLibrae	BLL	229.42	-24.37	36.68	0.07	216.8	0.032	3.76	0.37	Y
J0214.5+5145	TXS0210+515	BLL	33.55	51.77	36.7	0.11	218.8	0.051	0.42	0.12	Y
J1806.8+6950	3C371	BLL	271.71	69.82	36.77	0.07	225.9	0.032	1.3	0.18	N
J1353.0-4413	PKS1349-439	BLL	208.24	-44.21	36.79	0.07	228.0	0.032	0.33	0.12	N
J0200.1-4109	1RXSJ020021.0-410936	BLL	30.09	-41.16	36.85	0.07	234.4	0.032	0.51	0.14	N
J0627.1-3528	PKS0625-35	BLL	96.78	-35.49	36.89	0.07	238.8	0.032	1.81	0.26	Y
J2039.4+5219	1ES2037+521	BLL	309.85	52.33	36.89	0.07	238.8	0.032	0.58	0.15	N
J0523.0-3627	PKS0521-36	BLL	80.76	-36.46	36.91	0.07	241.0	0.032	1.17	0.21	N

Table 5.5: Jetted AGNs (*Fermi*-LAT 3FHL). 26 entries within 250 Mpc. 6 entries at $d_{\rm L} < 100$ Mpc, 14 at $d_{\rm L} < 200$ Mpc.

5.2.2 UHECR sky models

Little absorption occurs in the host galaxy and along the line of sight for the bands used to trace UHECR emission, but as propagation time increases, UHECRs experience increasing energy losses and photo-dissociation. To take into consideration the attenuation of their respective UHECR flux above a certain energy threshold, reliable estimations of the luminosity distances of host galaxies are required. In particular, taking the estimation of the distance from the spectroscopic redshift could induce mistakes for possible local sources, within a few tens of Mpc from the Milky Way, which could have a significant influence on intermediate-scale UHECR anisotropies while their host galaxies are not in the Hubble flow.

Galaxies in the Local Group were excluded with a cut at 1 Mpc, as otherwise, they would dominate the models. As a maximum distance, the value of 250 Mpc was taken for all catalogs except the starburst galaxy sample, for which a smaller horizon of 130 Mpc is taken due to the selection in the original catalog [148]. It is to be noted that no or very few starburst galaxies between 130 and 250 Mpc are expected to pass the flux-based selection in radio and far infrared. The best distance estimate and associated uncertainty were taken from the HyperLEDA database (`modbest` field), which accounts for peculiar motion and exploit cosmic-distance-ladder estimates whenever available, correcting the possible skews introduced by local sources, not in the Hubble flow.

All 26 jetted AGNs and 44 starburst galaxies in our sample are included in HyperLEDA. The apparent total K-band magnitude available in HyperLEDA (`Kt` field) enables a straightforward selection of 44,113 2MASS galaxies. A simple selection of 44,113 2MASS galaxies can be made thanks to the apparent total K-band magnitude present in the HyperLEDA (`Kt` field). Among 523 host galaxies, we found 23 Swift-BAT AGN without a tabulated HyperLEDA distance that still displays compatible redshift estimates ($|\Delta z|0.002$) in NED [2] and SIMBAD [3]. These 23 galaxies' distances are determined from their NED spectroscopic redshifts (corrected for the Local-Group infall to the Virgo cluster).

Based on the best-fit model of the spectrum and composition data acquired at the Pierre Auger Observatory [155], in particular the first minimum

[2]doi:`https://ned.ipac.caltech.edu/10.26132/NED1`

[3]`http://simbad.u-strasbg.fr`

obtained with the EPOS-LHC hadronic interaction model, we expect the UHECR flux from each host galaxy to be increasingly attenuated with increasing luminosity distance, d_L. For the three catalogs with fewer than 1,000 galaxies, the attenuation weights, $a(d_L)$, are marginalized over distance uncertainty, with little effect on the final sky models. The fourth sample, which consists of more than 44,000 near-infrared galaxies, is not marginalized over distance uncertainty in order to reduce the computational intensity, with barely any effect on the outcomes.
From an astronomical standpoint, each of the four sky models represents a major advance over the ones examined in 2018 [138]. Quantitatively, the increased sky coverage and depth of the surveys result in an increase in the number of jetted AGNs from 17 to 26 items, the number of starburst galaxies from 23 to 44, the total number of AGNs from 330 to 523, and the number of near-infrared galaxies from 41,129 to 44,113. In comparison to the study described in 2018, the calculation of distance uncertainty also offers a qualitative improvement. It should be observed, however, that the results are hardly impacted by these enhancements, suggesting that our earlier study adequately accounted for surveys from the perspective of astroparticles.
The best-fit sky models above 40 EeV obtained with the four catalogs are shown in figures 5.2 and 5.3. The models shown are based on the UHECR flux expected from each galaxy in proportion to its electromagnetic flux. These sky maps do not include any isotropic component and display only the flux expected from galaxies included in the catalogs, which is smeared on the best-fit Fisher angular scale above 40 EeV obtained with each catalog. A further top-hat smoothing on an angular scale $\Psi = 25°$ is performed for the sake of comparison with figure 4.10.

5.2.3 Likelihood-ratio analysis

A likelihood-ratio analysis is used to compare the correlation between UHECR arrival directions and the flux pattern predicted from the catalogs against isotropy. Using `HEALPix` with parameter `nSide = 64`, the model is produced on the sphere in equal-area bins as a function of direction u.

The null hypothesis under investigation, H_0, is that of an isotropic flux distribution. Accounting for the directional exposure of the array, $\omega(u)$, the isotropic model for the UHECR count density is

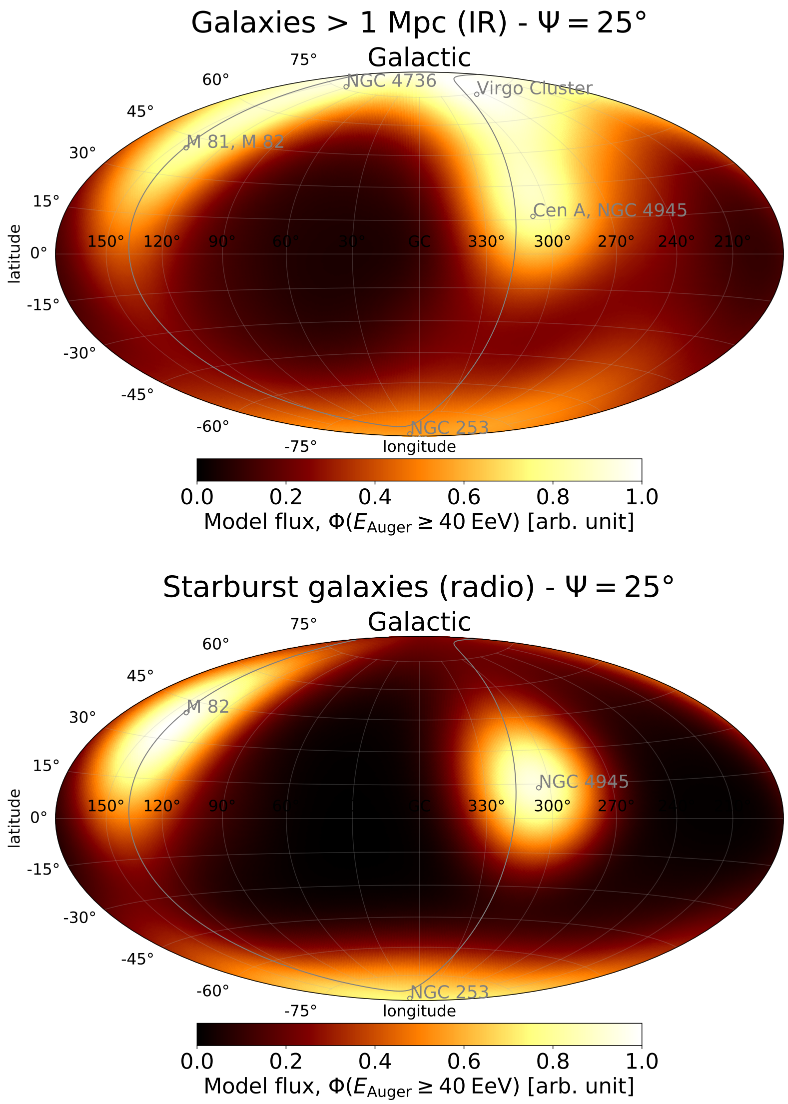

Figure 5.2: Best-fit UHECR infrared and radio source models above 40 EeV with a top-hat smoothing radius $\Psi = 25^\circ$ in Galactic coordinates. The supergalactic plane is shown as a gray line. Prominent sources in each of the catalogs are marked with gray circles.

$$n^{H_0}((u)) = \frac{\omega(u)}{\sum_i \omega(u_i)},$$

which normalizes to 1 summing over the `HEALPix` pixels indexed over i

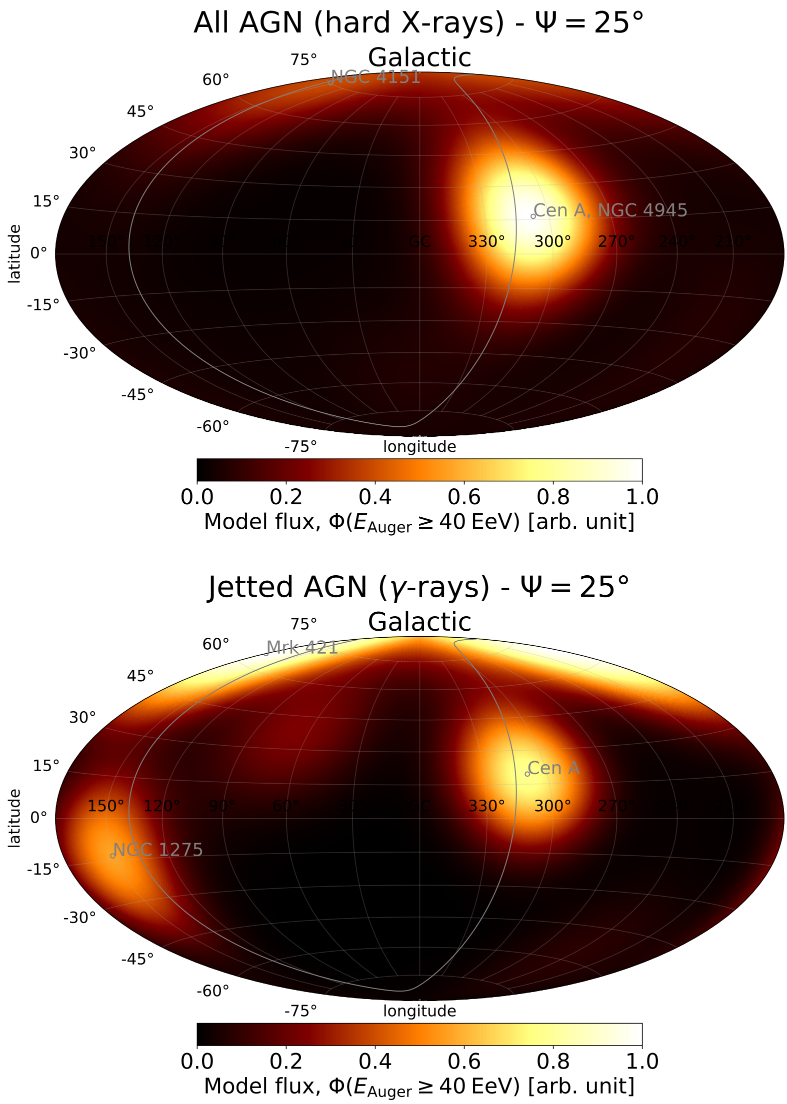

Figure 5.3: Best-fit UHECR X-ray and γ-ray source models above 40 EeV with a top-hat smoothing radius $\Psi = 25°$ in Galactic coordinates. The supergalactic plane is shown as a gray line. Prominent sources in each of the catalogs are marked with gray circles.

and of direction u_i.

The alternative hypothesis, H_1, in which H_0 is nested, is the sum of an isotropic component and a component derived from the tested catalog. The second component's amplitude is a variable signal fraction called α. The isotropic residual explains the absence of small or far-off galaxies from the catalogs as well as the deflection of a heavy nuclear component on large angular scales. The model for the UHECR count density under H_1 is as follows:

$$n^{H_1}(u) = (1-\alpha) \times n^{H_0}(u)) + \alpha \times \frac{\sum_j s_j(u;\theta)}{\sum_i \sum_j s_j((u_i);\theta)},$$

where the index j runs over the galaxies in the catalog. The von Mises-Fisher distribution with a smearing angle of θ is used to represent each galaxy's contribution to the UHECR flux, denoted as $s_j(u;Theta)$. Taking into consideration attenuation as a function of luminosity distance, $a(d_j)$, the amplitude of its contribution is proportional to the galaxy's electromagnetic flux, ϕ_j, so that

$$s_j(u;\theta) = \omega(u) \times \phi_j a(d_j) \times \exp\left(\frac{u \cdot u_j}{2(1-\cos\theta)}\right).$$

The von Mises-Fisher distribution is highest in the direction of the target galaxy, u_j. For all galaxies in a given catalog, it is assumed that the smearing angle θ, which corresponds to the 2D Gaussian extent in the small-angle limit, is the same. The average angular dispersion in intervening magnetic fields is accounted for by this parameter. The von Mises-Fisher distribution normalization is not included in the equation since it is the same for all galaxies and because the total anisotropic component is normalized on the sphere.

The likelihood-ratio test between H_0 and H_1 defines the test statistic

$$\mathrm{TS} = 2\ln(\mathcal{L}_1/\mathcal{L}_0)$$

where the product over the events of the models n^{H_0} and n^{H_1} yields the likelihood scores of the null and alternative hypotheses, $\mathcal{L}_0$ and $\mathcal{L}_1$, respectively. The evaluation of the test statistic is performed by grouping events in pixels. The test statistic for an observed event count in the direction u_i equal to k_i is computed as

$$\mathrm{TS} = 2\sum_i k_i \times \ln\frac{n^{H_1}(u_i)}{n^{H_0}(u_i)}.$$

The test statistic is maximized as a function of the two free parameters in the analysis (the signal fraction, α, and the search radius, θ) above consecutive energy thresholds. The optimization is achieved by scanning the 2D parameter space, making incremental changes to the signal fraction and search radius of 0.2 percent and 0.2° respectively. This method offers an accurate estimate that is independent of the chosen maximization strategy. The `Minuit` package, on the other hand, offers a rapid estimate for simulated data sets with accuracy on TS better than 0.1 units for event counts greater than 100. Monte Carlo simulations show that, under the null hypothesis, the test statistic follows a χ^2 distribution with two degrees of freedom above a specified energy threshold. The 1 and 2 σ C.L. on the best-fit parameters are determined by iso-TS contours that deviate by 2.3 and 6.2 units from the highest TS value, respectively.
A penalty factor that is well-approximated by a linear function of TS differentiates the post-trial p-value, which takes into account the energy scan, from the local p-value predicted by Wilks' theorem: pen $= 1 + (0.30 \pm 0.01)$TS [156]. This empirical penalty factor, just as done in previously reported analyses, is calculated using simulated isotropic data sets that have been evaluated against each catalog, and the linear coefficient's uncertainty is obtained by using the variance of the four tested catalogs. The penalty factor reaches a value of $\approx$10 for TS = 30.

5.2.4 Results

The search radius and signal fraction maximizing the test statistic above fixed energy thresholds ranging in 32–80 EeV are displayed in the four catalogs. The test statistic trend as a function of threshold energy shows two local maxima, with a first peak at energies above $\sim$ 40 EeV and a second peak at energies above $\sim$ 60 EeV. The first peak corresponds to the global TS maximum for all catalogs; the corresponding signal fractions range between 6 and 16%. The second peak is associated with the maximum signal fraction, ranging from 11 to 19%. As seen in the top axis of figure 5.4, the first peak's four times greater number of events (1,387 above 40:EeV vs. 331 above 60:EeV) results in a more significant departure from isotropy above 40 EeV.
As illustrated in figure 5.5, the statistical uncertainty on these parameters can be compared against the amplitude of fluctuations of the best-fit pa-

Catalog	$E_{\rm th}$ [EeV]	Fisher search radius, θ [deg]	Signal fraction, α [%]	$\rm TS_{max}$	Post-trial p-value
All galaxies (IR)	40	16^{+11}_{-6}	16^{+10}_{-7}	18.0	7.9×10^{-4}
Starbursts (radio)	38	15^{+8}_{-4}	9^{+6}_{-4}	25.0	3.2×10^{-5}
All AGNs (X-rays)	39	16^{+8}_{-5}	7^{+5}_{-3}	19.4	4.2×10^{-4}
Jetted AGNs (γ-rays)	39	14^{+6}_{-4}	6^{+4}_{-3}	17.9	8.3×10^{-4}
All galaxies (IR)	58	14^{+9}_{-5}	18^{+13}_{-10}	9.8	2.9×10^{-2}
Starbursts (radio)	58	18^{+11}_{-6}	19^{+20}_{-9}	17.7	9.0×10^{-4}
All AGNs (X-rays)	58	16^{+8}_{-6}	11^{+7}_{-6}	14.9	3.2×10^{-3}
Jetted AGNs (γ-rays)	58	17^{+8}_{-5}	12^{+8}_{-6}	17.4	1.0×10^{-3}

Table 5.6: The best-fit results obtained with the four catalogs at the global (upper) and secondary (lower) maximum.The energy threshold, $E_{\rm th}$, Fisher search radius, θ, and signal fraction, α, which maximize the test statistic, $\rm TS_{max}$, for each of the catalogs. The post-trial p-value accounts for the energy scan and search over α and θ.

rameters as a function of energy threshold. Consecutive energy bins have a non-negligible overlap as the search is conducted above successive energy thresholds in steps of 1 EeV. By finding the sequential reference energy thresholds at which the number of events is less than half that above the prior reference energy, we estimate that there are a total of five to six independent energy bins. This method proposes reference energy thresholds at $E \sim 32, 40, 50, 60, 70, 80$ EeV, with boundaries separated by more than $\Delta \log_{10} E = 0.06$, which corresponds to the energy resolution of $\pm 7\%$ relevant in the range described [157].

I listed the best-fit parameters and maximum test statistic that were obtained above the energy thresholds corresponding to the global maximum at $E \sim 40$ EeV in the upper part of table 5.6 and the secondary maximum identified at $E \sim 60$ EeV in the lower part of the same table. The most significant departure from isotropy is identified for all four catalogs at energy thresholds in the range 38–40 EeV, with post-trial p-values of 8.3×10^{-4}, 7.9×10^{-4}, 4.2×10^{-4} and 3.2×10^{-5} for jetted AGNs traced by their γ-ray emission, galaxies traced by their near-infrared emission, all AGNs traced by their X-ray emission and starburst galaxies traced by their radio emission, respectively. I did not penalize for the test of the four catalogs, which all offer comparable UHECR flux patterns, as in 2018 [138]. It should be noted that only the jetted AGN and starburst catalogs can be regarded as strictly different galaxy samples, with the infrared sample of galaxies containing a significant portion (more than 75%) of each of the other three catalogs.

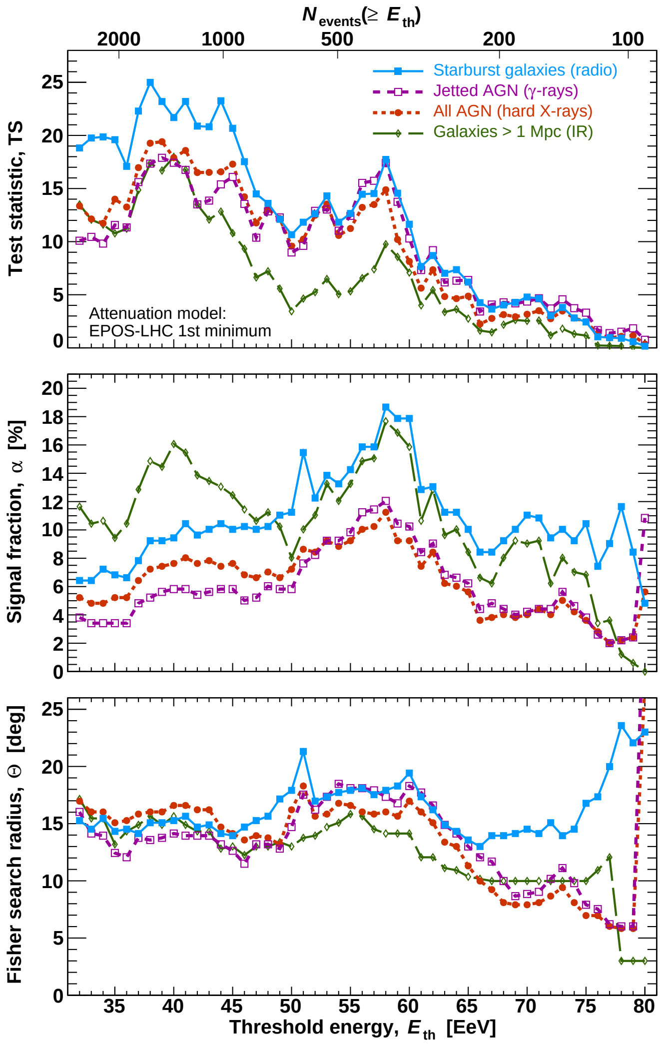

Figure 5.4: The test statistic (top), a signal fraction (center), and Fisher search radius (bottom) that maximize the deviation from isotropy as a function of energy threshold. The results obtained with each of the four catalogs are displayed with varying colors and line styles, as labeled in the figure. The uncertainties on the parameters, which are correlated above successive energy thresholds, are not displayed for the sake of readability.

As discussed in, all four sky models tested here are based on improved versions of the catalogs used in [138], although with a mild impact on the significance of the results and no noticeable change in the best-fit parameters. The maximum test statistic is obtained at the same point of the

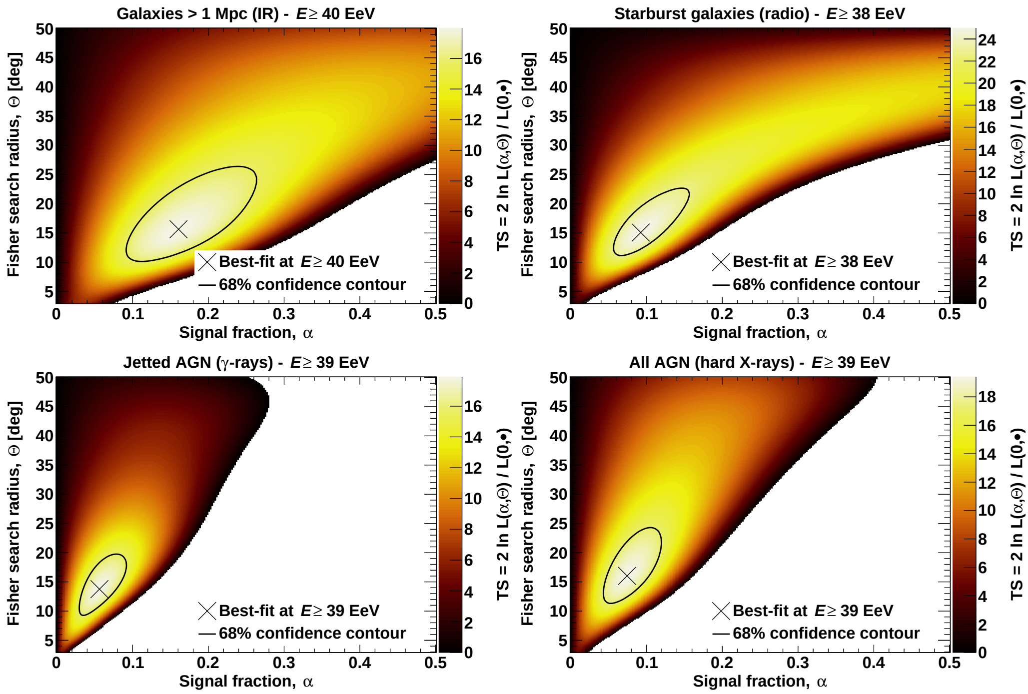

Figure 5.5: The test statistic as a function of signal fraction and search radius for the four tested catalogs, as labeled in the figure. The reference best-fit parameters obtained above the energy threshold that maximizes the departure from isotropy are marked with a cross. The 68% C.L. contour is displayed as a black line.

parameter space using the catalogs of infrared galaxies, starburst galaxies, and X-ray AGNs from [138], with TS values of 16.0, 23.1, and 18.0, respectively, differing by less than 2 units from the results in table 5.6. The most important change is observed for the gamma-ray catalog of jetted AGNs: the maximum TS (13.5) is obtained above ~ 60 EeV with the earlier catalog version based on the 2FHL catalog (which had a higher threshold on the photon energy of $E_\gamma > 50$ GeV), while it is obtained above ~ 40 EeV with the current version based on the 3FHL catalog (which has a threshold on the photon energy of $E_\gamma > 10$ GeV). The change can be understood from the lower energy threshold of the 3FHL catalog, which reduces the relative flux of blazars beyond 100 Mpc (Mkn 421, Mkn 501) with respect to the flux of local radio galaxies (Cen A, NGC 1275, M 87) combined with a stable excess of events in the surrounding region of Cen A (which will be discussed more in-depth in the next section).

A visual comparison of the sky models displayed in figures 5.2 and 5.3 reveals the primary similarity across the four catalogs: a hotspot predicted in the Auger field of view toward the group of galaxies composed of the radio galaxy Centaurus A, the Seyfert galaxy NGC4945, and the starburst galaxy M83. At a distance of around 4 Mpc, these three galaxies make up one of the pillars of the so-called Council of Giants [158], which surrounds the Milky Way and the Andromeda galaxy. The two AGN models, tracing accretion through X-ray emission and jet activity through *gamma*-ray emission, do not indicate bright secondary hotspots in other sky regions at the highest energies ($E \sim 60\,\mathrm{EeV}$), as the attenuation of the UHECR flux significantly reduces the contribution from more distant galaxies. On the other hand, both the infrared model of stellar mass and the radio model of enhanced starforming activity suggest hotspots in the directions of other Council of Giants members: the starburst galaxies NGC253 and M82, which are the only two starburst galaxies currently detected at TeV energies[4]. While M82 is located in the Pierre Auger Observatory's blind zone and can only be detected with the Telescope Array [159], NGC253's contribution is what causes the starburst model's higher deviation from isotropy when compared, for instance, to the X-ray AGN model. Instead, compared to both the X-ray AGN and the starburst models, the infrared model produces a lower test statistic. In fact, in contrast to the UHECR observations, the infrared model predicts that the Virgo cluster region (located at $d \sim 20$:Mpc) would be brighter than the Centaurus region.

To find out which of the four models the data favors over the others, I quantitatively compared each of them against the others. The infrared, X-ray and γ-ray models fit the data at $E \geq 38 - 40\,\mathrm{EeV}$ worse than the starburst model with C.L. close to 3σ. No firm evidence for a catalog preference is identified.

[4]`http://tevcat2.uchicago.edu/`

5.3 The Centaurus Region

A hotspot in the Centaurus area is what's responsible for the deviation from isotropy individuated with all four galaxy catalogs. All four sky models exhibit an elevated flux in this location, with the two AGN models mostly originating from Centaurus A, the starburst model originating from NGC4945, and the infrared model originating from both galaxies. The primary contributor to the starburst model, NGC4945, and the main contributor to the AGN models, Centaurus A, are located 2.9° and 5.1°, respectively, distant from the peak direction of the UHECR hotspot, as determined by the blind search for excesses.

Since more than ten years ago, the Pierre Auger Collaboration has focused its searches for UHECR excess on Centaurus A [160], the nearest radio galaxy at 3.68 ± 0.05 Mpc. I update these searches by choosing Centaurus A (α, δ)=(201.4°,-43.0°) as our target and carrying out the same analysis as in section 5.1.1. Figure 5.6 displays the map of the local p-values as a function of energy threshold and top-hat search angle. The largest excess is seen at E_{th}=38 EeV in a circle with top-hat radius $\Psi = 27°$, where there are $N_{obs} = 215$ observed events compared to $N_{exp} = 152.0$ predicted by isotropy. The minimum local p-value is calculated as in section 5.1.1. from the binomial probability to see N_{obs} or more events from an isotropic distribution, and it is 2.1×10^{-7}. The post-trial p-value is 4.5×10^{-5} after accounting for the scan in energy and search angle, which is comparable to the result of the likelihood-ratio test for starburst galaxies versus isotropy.

5.4 Discussion of results

5.4.1 Additional checks on the compatibility of the vertical and inclined samples

As reported in the previous chapter, we noticed an energy dependence in the ratio between the number of inclined and vertical events; this dependence at the highest energies ($>$ 80 EeV) results in a deficit of inclined events, which could be explained by a statistical fluctuation in the two different samples. The discrepancies in the energy calibration of the two data streams, which are based on separate sets of hybrid events, offer another possible explana-

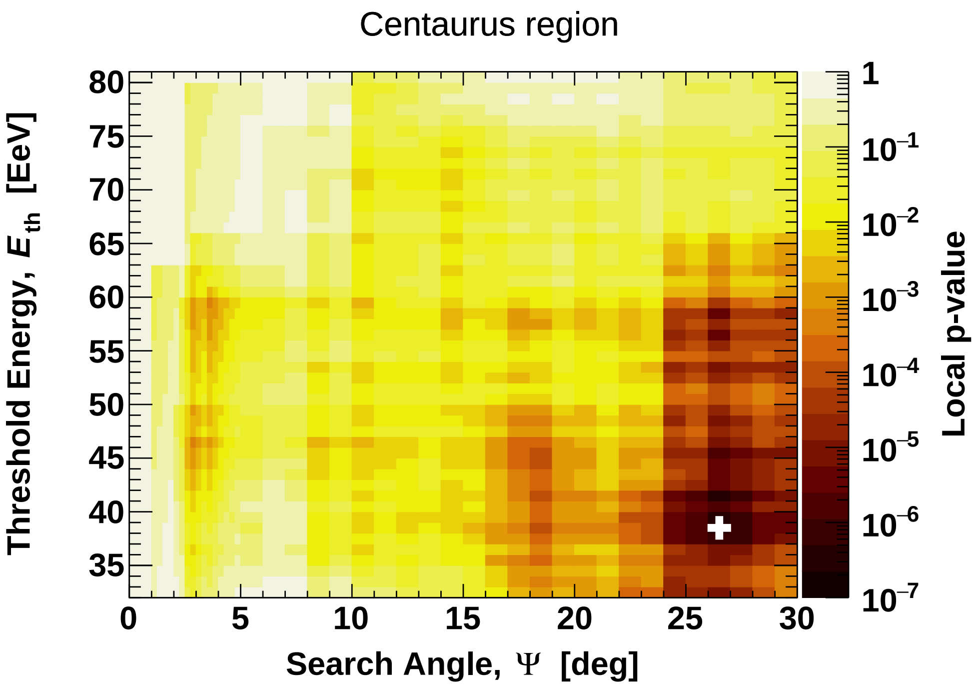

Figure 5.6: The local p-value for an excess in the Centaurus region as a function of top-hat search angle and energy threshold. The minimum p-value, obtained for the best-fit parameters, is marked with a white cross.

tion for the deficit of inclined events at the highest energies. By choosing the events with zenith angles between $57° < \theta < 63°$ that are reconstructed by both the vertical and inclined reconstructions and for which six active stations surround the one closest to the core position (6T5 condition), I empirically tested the effect of the difference in the two energy reconstructions. I found 161 common events this way, and I fit a power-law relation of the form $E_{\mathrm{vert}} = A \cdot E_{\mathrm{incl}}^{B}$ to extract the parameters (A, B) that would convert the energies obtained from the inclined reconstruction to the energies obtained from the vertical reconstruction. I applied the same adjustment to the energy of all the events in the inclined data set and, as a cross-check, I conducted the likelihood analysis with the starburst catalog and the Centaurus region search. In the case of the former, I discovered a maximum test statistic of 24.6 (as opposed to 24.9 with the standard data set) at the same location in the parameter space. The minimal local p-value for the Centaurus region is 1.9×10^{-7} (vs. 1.8×10^{-7} for the standard data set), and the same values of energy threshold and search radius are discovered for the test data set as with the standard one. This cross-check shows that the results given in this study are unaffected by any potential systematic uncertainties brought on by the different energy calibrations of the vertical and inclined reconstructions.

5.4.2 Comparison between analyses

Unsurprisingly, the blind search and the search in the direction of Centaurus A have comparable best-fit parameters. The direction being determined *a priori*, as suggested by the early searches from the Pierre Auger Collaboration [160][161], is the cause of the lower post-trial p-value compared to the blind search. The Fisher search radius obtained from catalog-based searches can be compared to the top-hat angular scale inferred from the blind search and from the search at the point of Centaurus A using the relation $\Psi = 1.59\theta$. or a Fisher radius $\theta \ll 1\,\mathrm{rad}$, this relation provides the top-hat radius Ψ that maximizes the signal-to-noise ratio, where the noise is $\propto \sqrt{1 - \cos\Psi}$ and the signal is $\propto \exp(k) - \exp(k\cos\Psi)$, with the concentration parameter $k = [2(1 - \cos\theta)]^{-1}$. The results of the catalog-based searches are $\theta = 14 - 16°$, which equates to $\Psi = 22 - 25°$, or a range of values that are congruent with those deduced from the other searches.

5.4.3 Interpretation of the evolution of the signal with energy

Searches in the Centaurus region and catalog-based searches both indicate a most significant signal at an energy threshold close to 40 EeV. The flux suppression of the energy spectrum above the toe is included in this energy range, at $E_{34} = 46 \pm 3 \pm 6$ EeV (where the first error is statistical and the second systematic) [119]. The distribution of events in the Centaurus region appears to be the primary factor driving the development of the signal with energy. Profiling the local p-value against the search radius and penalizing for this free parameter results in the pre-trial p-value for the Centaurus region. The test statistic of the starburst catalog is compared to the profile as a function of the energy threshold. The latter is used as an illustration, and it is noted that data from other catalogs demonstrate a similar dependence on energy threshold (figure 5.4). A currently well-supported hypothesis is that UHECRs are accelerated in proportion to their charge following so-called Peters' cycles, as suggested by constraints from maximal shower depths up to a few tens of EeV and the broad-band spectrum above the ankle energy [155] [119]. The UHECRs near a maximum magnetic rigidity, R_{cut}, is thus anticipated to dominate the cosmic-ray composition above the toe in the energy spectrum. With the aid of our reference model, we deduced in [155] that the maximum rigidity is $\log_{10}(R_{\rm cut}/{\rm V}) = 18.72^{+0.04}_{-0.03}$ while also accounting for systematic uncertainty on the energy and maximum shower-depth scales. As shown in the top axis of figure 5.7, a lower constraint on the charge of the bulk of UHECRs beyond a specific energy threshold can be calculated using this value as the typical rigidity of UHECRs above the toe: $Z_{\rm min} = E_{\rm th}/R_{\rm cut}$. The uncertainty on the points is those at the scenario's maximum rigidity. It should be noted that the composition at the higher energies is currently conjectured from a model-dependent approach as Phase One data on this parameter remains poorly constrained.

[136] suggests that UHECR propagation in the Milky Way magnetic field transitions into a semi-ballistic regime at rigidities close to $R_{\rm cut} = 5\,{\rm EV}$, i.e. $\log_{10}(R_{\rm cut}/{\rm V}) \approx 18.7$. Excesses found in the UHECR sky might thus be used to restrict the configuration and intensity of the Galactic magnetic field as well as to track back potential sources. The average angular dispersion predicted in the Milky Way of the Auger mix of nuclear species is supported by the angular scale determined from the catalog-based search, as well as that from the blind search and search in the Centaurus region. Nevertheless, the identification of the host galaxies of UHECR accelerators and UHECR constraints on the Galactic magnetic field is still restricted by the absence of a discernible preference for a particular class of galaxies and the strength of the anisotropy signal, which at best post-trial p-values of $(3-5)\times 10^{-5}$. Even though the most notable departure from isotropy is observed at energies around 40 EeV for practically all studies, the excess is also hinted at for all catalogs and the Centaurus area at energies around 60 EeV. In fact, early Auger data revealed the first sign of anisotropy in this higher energy range. An interpretation of the energy development of the signal on intermediate angular scales might be made in terms of the maximum energy attained for higher-charge nuclei. A Peters' cycle model, such as that presented in the

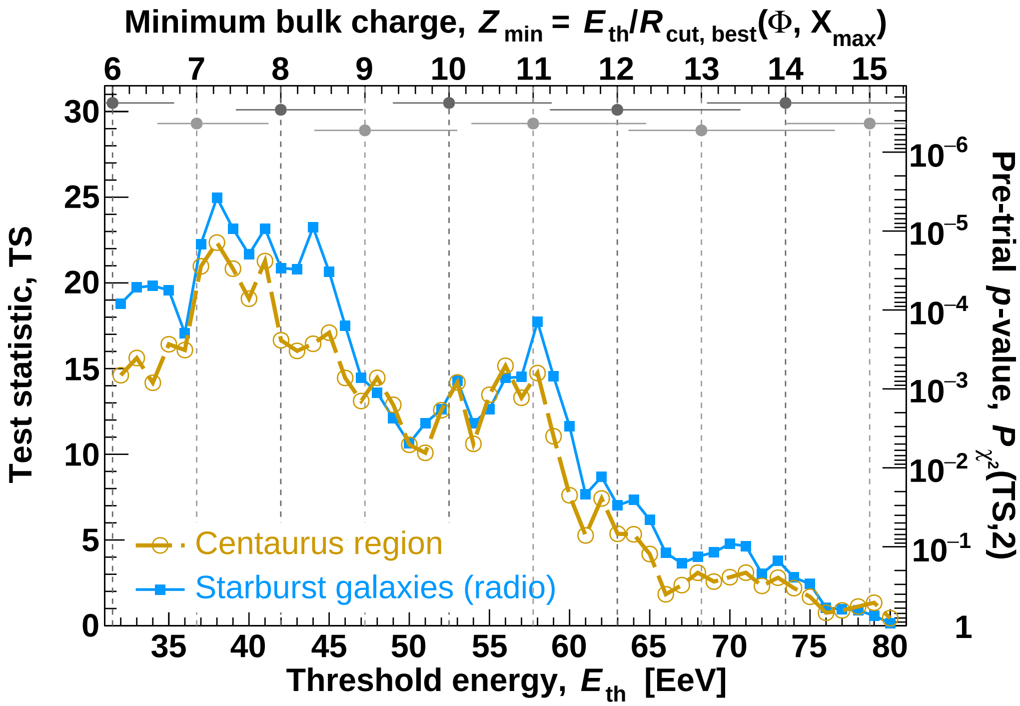

Figure 5.7: The test statistic and pre-trial p-value, after profiling against the search radius and penalization for this free parameter, as a function of energy threshold. The gray points along the top axis figure the estimate of a lower bound on the bulk charge of UHECRs above a given energy threshold, under the assumption of an energy-to-charge ratio close to the maximum rigidity inferred by jointly modeling the energy spectrum and composition observables [155]

previous section, would interpret the evidence for anisotropy above 40 EeV as coming from CNO nuclei, which would imply that $Z \approx 10 - 12$ nuclei are responsible for the departure from isotropy above 60 EeV. The estimate of maximum rigidity used here is based on the combined fit of the spectrum and depth of shower maximum performed in [155]. We will be able to examine this scenario when arrival-direction information will be directly included in such analyses.

If this scenario of local extragalactic sources is extrapolated to lower energies, one could expect a contribution from He nuclei in the energy range where a significant dipole, but no significant quadrupole has been reported using data from the Observatory. The strength of such an anisotropic con-

tribution could nonetheless be further diluted in the contribution from more distant sources.
We foresee that an in-depth comparison could be drawn by studying the evolution of the large-scale dipolar and quadrupolar components as a function of energy. I checked that no significant large-scale deviation from isotropy can be inferred from arrival-direction data in the energy range covered here, with constraints on the dipolar and quadrupolar components not in tension with those expected from best-fit catalog-based models.

5.4.4 Future reachability of the discovery threshold

The Phase One high-energy data set only provides fragments of evidence for intermediate-scale anisotropy, but prolonged array operation may allow for the crossing of the 5 σ detection threshold. The latter corresponds to a post-trial p-value of 2.9×10^{-7} or 5.7×10^{-7} depending on whether excesses and deficits are sought (2-sided test) or only excesses (1-sided test). Figure 5.8 shows the development of the test statistic of the starburst model as a function of cumulative exposure, as well as the increase of the signal in the Centaurus region, as measured by the excess of events with respect to the isotropic expectation. These analyses yield post-trial significances of 3.9-4.2 σ for a 1- or 2-sided test applied to the Phase One high-energy data set. Both the test statistic and the excess of events should increase linearly with exposure, and any oscillations seen around such a pattern are in keeping with what may be predicted from simulations. The most reliable method for predicting the signal's development is the model-independent search in the Centaurus area due to the small fluctuations. Assuming a fixed top-hat angular scale $\Psi = 27°$, the 5σ (1-sided) discovery threshold would be expected for a total accumulated exposure of $165{,}000 \pm 15{,}000\,\mathrm{km}^2\,\mathrm{yr\,sr}$ (68% C.L.), which would be achievable by the end of 2025 (± 2 calendar years) if a strategy similar to that developed in the present study was used.

Additionally, I performed a test to simulate the significance of the Centaurus region analysis accounting for the possibility of excluding the heaviest component of the dataset in the framework of AugerPrime. The test was conducted in a very simple manner: I assigned to each event a probability P of being rejected, except to $N_{obs} - N_{exp} = 63$ excess events within $\Psi = 27°$ of CentaurusA, which are given $P/2$ of being rejected, hypothesizing the warm-

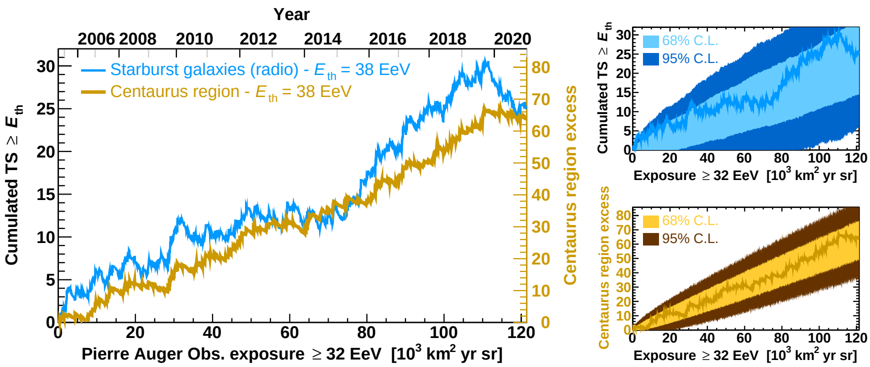

Figure 5.8: Test statistic of the starburst model and excess in the Centaurus region above the best energy threshold as a function of exposure accumulated by the Pierre Auger Observatory. The fluctuations around the expected linear behavior are consistent with those expected from signal simulations, as illustrated in the right-most panels.

spot to contain the lighter, less deflected component. A 5σ significance is obtained with a P of 22%. This shows that, even with current statistics, reaching a significant result should not require a precise estimation of the mass of the primary but simply an estimation of the heaviest elements in the dataset.

5.4.5 Flux and spectral index in the Centaurus region

It is possible to calculate the average flux above 40 EeV in a 25° top-hat area (for comparison with the flux map shown in figure 4.10) centered on Centaurus A as $\Phi_{\rm Cen}(\geq 40\,{\rm EeV}, \Psi = 25°) = (15.9 \pm 1.3) \times 10^{-3}\,{\rm km}^{-2}\,{\rm yr}^{-1}\,{\rm sr}^{-1}$. For comparison, regions centered on the Virgo cluster and the starburst galaxy NGC253 have fluxes of $\Phi_{\rm Virgo}(\geq 40\,{\rm EeV}, \Psi = 25°) = (12.2 \pm 1.8) \times 10^{-3}\,{\rm km}^{-2}\,{\rm yr}^{-1}\,{\rm sr}^{-1}$ and $\Phi_{\rm NGC\,253}(\geq 40\,{\rm EeV}, \Psi = 25°) = (12.8 \pm 1.2) \times 10^{-3}\,{\rm km}^{-2}\,{\rm yr}^{-1}\,{\rm sr}^{-1}$. The areas of NGC253 and the Virgo cluster could be expected to be as luminous as and brighter than the Centaurus region, respectively, if the UHECR emission rate was simply tracked by star-formation rate and stellar mass, as shown by the model sky maps. There is currently no clear preference for correlation with particular classes of galaxies, despite the fact that the starburst catalog may identify the most significant divergence from isotropy (4.2σ) and the jetted AGN catalog the least significant

deviation (3.3σ). Additionally, it should be noted that such a preferred correlation would not necessarily imply causation in the sense of pinpointing the source of UHECRs, as the regular and turbulent magnetic fields that these charged particles could travel through could change the anisotropic pattern seen on Earth.
Computing the raw energy spectrum in the Centaurus region, defined as the top-hat circle of radius 27° centered on Centaurus A found in the respective analysis, I found a discrepancy when compared to the spectrum obtained in the whole sky with the dataset. More precisely, the flux inside the warm-spot region is stronger in the higher energy bins, resulting in a flatter spectrum overall. The two spectra, obtained only with vertical events to exclude complications arising from the combination of the two samples, are compared in figure 5.9.

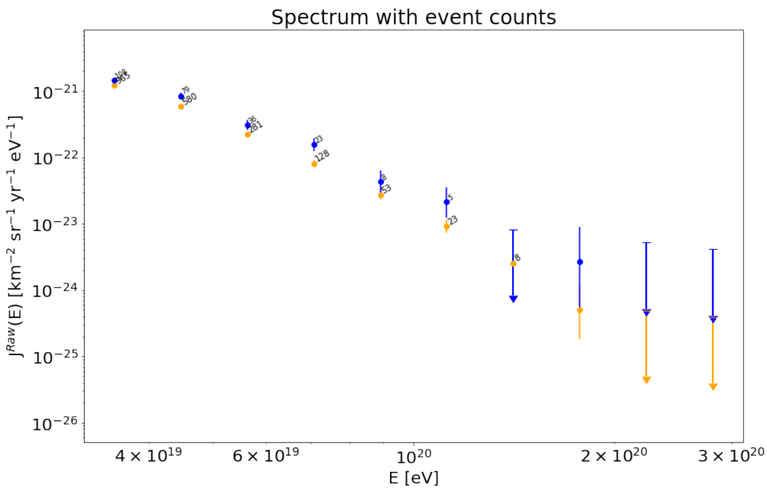

Figure 5.9: Vertical raw energy spectrum obtained in the whole sky, in orange, and only in the Centaurus region of top-hat radius 27°, in blue. The number of events in each energy bin is reported above each point. In the empty energy bins, the upper limits to the flux were computed. The spectra are obtained with the same method as [157], which however used a 6T5 selection instead of the 4T5 selection used here.

Simplifying the description of the two spectra as single power laws results in a spectral index of -3.8 ± 0.2 for the whole sky and -2.9 ± 0.1 for the Centaurus region. It is to be noted that this result is not unexpected, as the dedicated analysis finds a maximum significance for the excess in the region

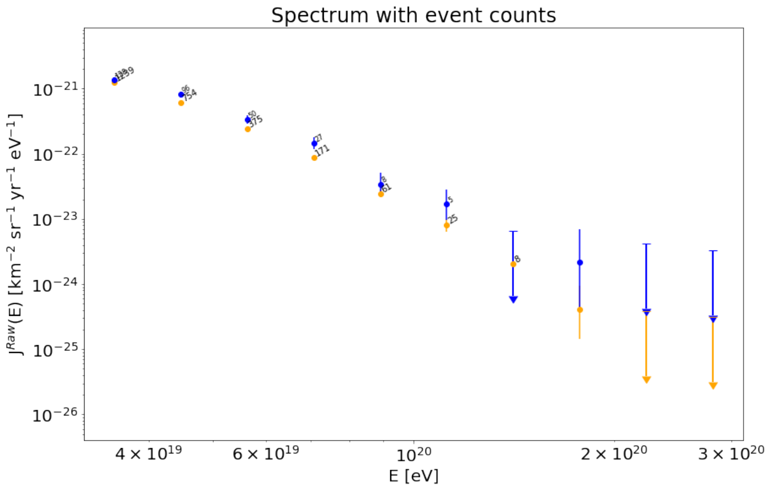

Figure 5.10: Vertical and inclined combined raw energy spectrum obtained in the whole sky, in orange, and only in the Centaurus region of top-hat radius 27°, in blue. The number of events in each energy bin is reported above each point. In the empty energy bins, the upper limits to the flux were computed.

at $E_{th} = 38$ EeV, and a second maximum of around 60 EeV. If the excess did not modify the spectral index when compared to the whole sky, the threshold for maximum significance would have been 32 EeV. For reference and completeness, I include in figure 5.10 also the results obtained with the two combined samples, vertical and inclined.

5.4.6 Conclusion

Making definite statements about the origins of the highest energy particles known to exist in the Universe at this time is not possible. This is partly caused by the magnetic field deflection they experience. It is true that determining the origins of UHECRs and determining the characteristics of the Galactic and extragalactic magnetic fields are related, and limitations on one of these will improve our comprehension of the other. By including composition-sensitive observables in arrival direction investigations, a significant advance will be made. This will be accomplished either by looking for anisotropy in the moments of such composition observables or by using them to narrow the field of candidates for light nuclei event by event.

Future studies utilizing the Observatory offer the possibility to achieve this with the AugerPrime improvement, which will improve mass discrimination with the surface detector operating at 100% duty cycle.

5.5 Searches for neutrons in small-scale anisotropies

As described in section 3.10.3, in the past the Collaboration has performed searches for neutral particles, and in particular neutrons in its dataset by looking at small-scale anisotropies, both with a blind approach [127] and in a targeted approach [128]. Neutrons are produced by protons or nuclei in interactions with material surrounding the sources and, having no charge, are not deflected by magnetic fields, and point directly to their production point. The targeted search strategy in particular focused on Galactic objects, as neutrons are unstable particles in their free state and thus decay with a mean path length l = 9.2 kpc × (E/EeV), a horizon which includes the Galactic Center for neutrons with energy above the EeV and most of the Galactic disk at higher energy thresholds, but would require unobserved energies to reach other galaxies. In this section, the preliminary results for the upcoming update of the targeted search for point sources of neutrons are presented.

5.5.1 The dataset

Compared to the previous publication, the largest effort for the upgrade consisted of a more in-depth study of the angular resolution and the addition of two samples to the dataset, which originally consisted only of vertical showers detected by the main SD array: the inclined sample and the infill dataset.

The inclined sample contains 353227 events above 1 EeV with a zenith angle between 60° and 80°. The main advantage of analyzing inclined events is the extended field of view visible by the Observatory, with the maximum declination increasing from 25° to 45°. In particular, this extension brings the Crab nebula, one of the most thoroughly studied astrophysical sources of γ rays, into the field of view.

The infill dataset contains 2235796 events above 0.1 EeV with a zenith angle between 0° and 55°. As other results published by the Collaboration point to an extragalactic origin for UHECRs above 8 EeV and, as discussed in section

1.1, many models describing the UHECR spectrum point to the transition between the Galactic and extragalactic cosmic ray flux components as being between the *second knee* around 0.1 EeV and the ankle at 4 EeV. Adding lower energy events enables the analyses to contribute more broadly to the studies involving the transition between the Galactic and extragalactic flux and to investigate regions of the parameter space where Galactic sources could have more influence. Conversely, lowering the energy threshold makes the horizon imposed by the decay length of neutrons shrink: at 0.1 EeV only sources at a distance of ≈1 kpc are reliably reachable.
The updated vertical dataset contains 2535932 events. All three subsamples contain events recorded from 1 January 2004 to 31 July 2022.
Due to the small scales investigated in this kind of analysis, of the order of 1 degree, it is of utmost importance to estimate correctly the angular resolution of the events. The angular resolution η depends on the errors $d\theta, d\phi$ on the reconstructed arrival direction in local coordinates θ, ϕ:

$$\eta = \sqrt{-\ln(0.32)(d\theta^2 + \sin^2(\theta)d\phi^2)}$$

It is not generally considered reliable with the requested precision on an event-by-event basis, and for this reason, it was decided to study the distribution of reconstructed angular resolutions of events in the dataset and take the average η in bins of θ and multiplicity (i.e. the number of triggered stations) for use in the analysis. Previously the average angular resolution for each target, obtained from a fit in declination of the 1000 closest events to each candidate, was used in the analyses.

5.5.2 The target catalogs

The Galactic objects considered in the analysis were classified in 9 catalogs, plus the Galactic Center which was considered separately. If a source was present in more than one set, it was assigned to the more exclusive one. The sources are tabulated together with their position in the sky and, when available, distance and electromagnetic flux in the reference band. In the case of multiple sources close to each other, such as a group of pulsars in a cluster, an average position is taken as a reference together with the total flux from the region. The catalogs, divided according to the non-thermal emission taken into account, are:

- γ-emitters in the TeV band, subdivided into unidentified sources, pulsar wind nebulae, and other identified objects. The flux of these objects is given in Crab units, i.e. normalized to the flux of the Crab nebula, which is taken as a prototype TeV γ-ray emitter. Distance information is not available for unidentified objects. The samples are taken from TeVCat [5].

- γ-emitting pulsars observed by Fermi-LAT in the 100 MeV - 100 GeV band and tabulated in the 4FGL catalog [162].

- X-ray emitters of two classes: X-ray binary systems, further subdivided in Low Mass X-ray binaries [163], High Mass X-ray binaries [164] and microquasars, and Magnetars. The former are binary systems composed of a neutron star or black hole accreting matter from a companion star, which can be lighter than the compact object (LMXB) or heavier (HMXB); if the compact object in the system is a black hole, in some cases relativistic jets are present in addition to the accretion disk (microquasar).
  Magnetars are peculiar neutron stars with enormous magnetic fields, with orders of magnitudes reaching $10^{14} - 10^{16}$ G. These objects can experience outbursts, during which their luminosities in the X band increase up to a factor 1000 very quickly before decreasing slowly [165][166].

- Millisecond pulsars, detected from their radio emission [167][6]. These are pulsars with a rotation period between 1 and 10 ms, in the early stage of their lives.

The considered catalogs are analogs to the ones considered in [128], with updated source numbers and new information, especially in the TeV emitters category, which previously was populated only by sources detected by H.E.S.S., while the modern TeVCat also contains observations from LHAASO, MAGIC, VERITAS, and HAWC.

[5] http://tevcat2.uchicago.edu/

[6] Updated version from https://www.atnf.csiro.au/research/pulsar/psrcat/

5.5.3 Analysis methods

Another substantial update presented here in comparison with previous publications on searches for neutrons is the analysis method. Previously, a simple counting of events within the angular resolution assigned to the source based on its declination was employed. Conversely, we proposed a more complex method, which consists in assigning, for each candidate source, a weight to each event in the dataset based on the value of a gaussian centered on the reconstructed arrival direction and with $\sigma = \eta$, where η was extracted based on the θ and multiplicity of the event, as described previously. The weights relative to each candidate source are then summed. The p-value associated with each source was obtained by repeating the analysis using simulated isotropic datasets and counting the number of times the sum of weights from simulations is higher than the observed one. The simulated datasets are obtained using the *scrambling* technique, consisting in generating a new dataset by randomly mixing the time, energy, and reconstructed arrival direction information; this technique is necessary as the energies included in the dataset are in some cases below full efficiency for the SD array, and as such analytically generating an isotropic dataset from the exposure is not possible. The local p-value is penalized for each catalog, as in [128] by taking $p^* = 1 - (1-p)^N$ as global p-value. From these results, we can also compute the upper limit on the flux of neutrons from each source, which is derived as $\phi_{UL} = 1.39 s_{UL}/\omega_{dir}$, where s_{UL} is the signal upper limit and ω_{dir} is the directional exposure [128].
The analysis is repeated in different energy bins: for the vertical and inclined SD-1500 datasets, the bins are 1 EeV $<$ E $<$ 2 EeV, 2 EeV $<$ E $<$ 3 EeV, E $>$ 3 EeV and E $>$ 1 EeV (full dataset); for the infill dataset, the bins are 0.1 EeV $<$ E $<$ 0.2 EeV, 0.2 EeV $<$ E $<$ 0.3 EeV, E $>$ 0.3 EeV and E $>$ 0.1 EeV (full dataset).

5.5.4 Preliminary results

The analysis did not produce significant results for any singular object or object catalog. The most significant excess, at $p^* = 0.0066$ is found in the PWN TeV catalog using the infill dataset in the 0.2 EeV $<$ E $<$ 0.3 EeV range; this corresponds to a flux upper limit of 0.96 km^{-2} yr^{-1}. This result is not surprising, as previous results for this type of search, as well as the indications on the Galactic cosmic ray flux in this energy range disfavor the presence of sources in the close surroundings of the Solar System. These preliminary results will be presented in more detail and expanded upon in future publications by the Collaboration. In the future, the addition of mass information using AugerPrime to select the lightest components from the dataset and the possibility of adding a temporal analysis to study variability in the candidates could bring more significant results.

Chapter 6

Paleo-detectors for astroparticle physics

As sketched in chapter 2, natural minerals are used in the paleo-detector technique as solid state track detectors (SSTDs) for cosmic messengers including neutrinos, dark matter, and, as I proposed in this thesis, ultra-high energy cosmic rays (UHECRs). The method is based on phenomena where fast heavy ions can damage portions of solid materials, whether they are crystalline or amorphous, leaving tracks that are typically cylindrical in shape and with lengths varying from the nm to the mm based on the ion energy. The fast heavy ions in the case of paleo-detectors are the atoms making up the solid themselves: energetic penetrating particles can interact with them both elastically and inelastically, making them recoil or fragmenting them, and damaging the solid structure. These imperfections, which I shall refer to as *tracks* from now on, are of a semi-permanent nature and are only removed by an event that structurally alters the mineral, such as mechanical breakdowns or changes brought on by high temperatures or pressure. The two main hypotheses about the formation of the tracks are the *thermal spike* model and the *ion explosion* model (figure 6.2); nevertheless, the precise process is still not fully understood. The method has been used for a very long time [168], mostly for the observation of natural and induced fission tracks [169], generated by energetic ions produced by the fission of uranium, a frequent contaminant in minerals, rather than for the observation of cosmic messengers; these fission tracks are commonly observed in Obsidian and Apatite, as shown in figure 6.1, after a chemical process called *etching*, which enlarges and highlights structural defects.

The idea of using natural minerals as SSTDs in the hunt for exotic particles and interactions is an idea that by now has accrued a sizeable history,

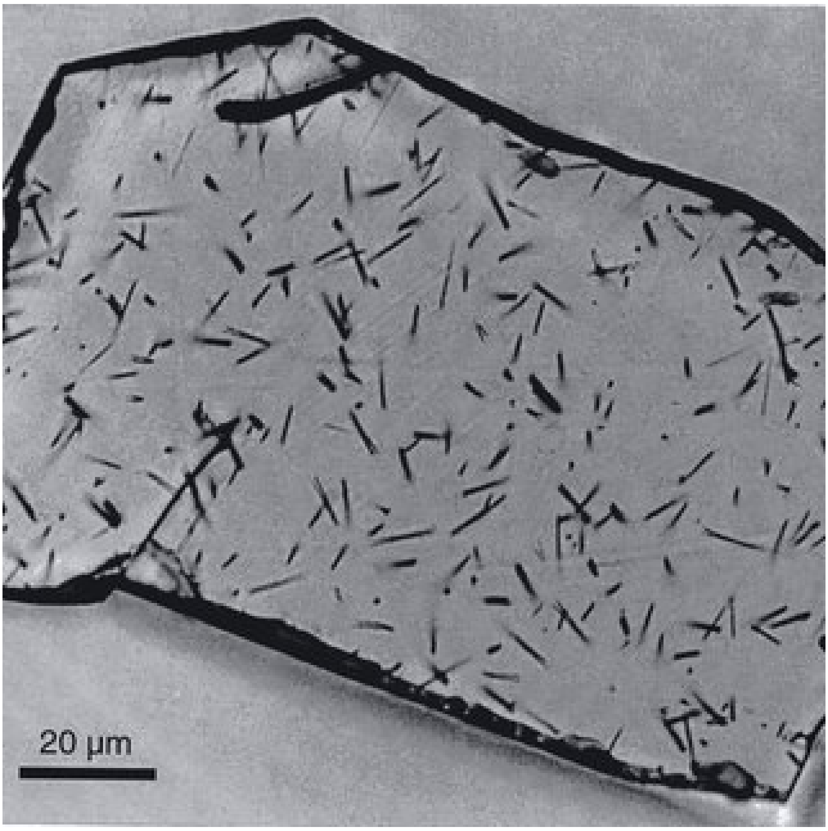

Figure 6.1: Etched fission tracks in an apatite grain from the Grassy Granodiorite of King Island, southeastern Australia. The tracks show their characteristic appearance as randomly oriented, straight-line etch channels up to a maximum length of around 16μm. From [170]

at least as a proposal. The initial mentions, which date back to the 1960s, suggested the possibility of looking for magnetic monopoles that had been trapped and accumulated over Myr timeframes in ferromagnetic materials [173][174]. Following publications in the same area of study and time frame present a different strategy, and for the first time, they discuss tracks — in that case, those left by throughgoing monopoles [175]. Similar theories suggested looking for Fullerenes [176] produced by ionizing particles in geological materials, or radioactive and rare isotopes produced by supernovae and other catastrophic cosmic events. Snowden et al. published the original proposal of observing WIMP-induced tracks [177], using muscovite mica as a target sample. With significant advancements in read-out technology

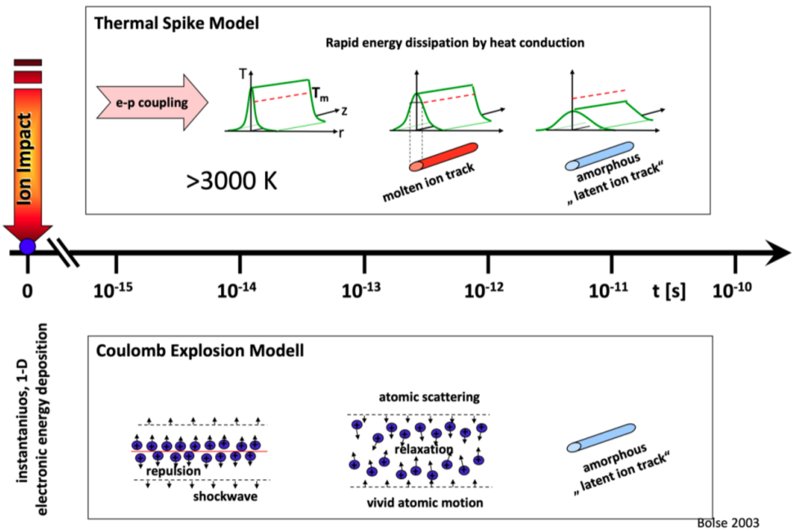

Figure 6.2: Two different models for the formation of tracks in condensed matter. Upper from [171], lower from [172].

as well as in the theoretical and practical understanding of potential messengers, the paleo-detector technique is experiencing a revival of proposals, starting from the 2019 paper [107], and subsequent works proposing it for the search for DM and other rare interactions [178][179][108][180][181][182]. The interactions from many different cosmic messengers, even though they are rare, pile-up over time accumulating an impressive exposure that can be equivalent to that of man-made experiments intended to detect the same particles or interactions. The primary caution still relates to identifying and/or finding samples sufficiently shielded against backgrounds that might obscure the preferred signal.

In the following chapter I will describe some possible read-out techniques, the main signals proposed for paleo-detectors and their common backgrounds, as well as an original proposal for the utilization of these minerals for UHECR indirect detection.

6.1 Choice of candidate minerals: generalities and common backgrounds

Specific criteria for identifying suitable minerals are necessary in order to develop mineral detection methods. In order to build a mineral detection method for dark matter and neutrinos, we must first have access to a substantial quantity of mineral grain for experimentation. Additionally, during experimentation, including sample preparation, minerals must be stable. The mineral should also be datable, with a precision that varies based on the application. Finally, it should be mentioned that heterogeneity is a characteristic of real samples. Chemical heterogeneity in minerals, such as that found in solid solutions, often manifests as zonal structure. They might also have fluids and other mineral phases included in them. It's possible to find cracks and dislocations as well. When creating readout techniques, it is important to distinguish between artifacts caused by heterogeneity and cosmogenic signals.

Another aspect to be considered when selecting the mineral is the presence of radiogenic contaminants, namely ^{238}U, ^{235}U, and ^{232}Th. Due to the relative abundance at this point in Earth's history, the most important decay progenitor at the moment is ^{238}U. These isotopes can spontaneously undergo fission decay, each fission event producing two daughter nuclei that travel in the opposite direction, resulting in a single trail of damage with the length depending on the energy loss (typically O(keV/nm))of the fragments in the condensed matter along their trajectory. As the initial kinetic energy distribution averages around 170 MeV (figure 6.4), tracks are generally O(10) nm in diameter and O(10) μm in length.

Unstable isotopes can also undergo different decay phenomena, namely α,β and γ decays. While β and γ particles are too light to leave tracks themselves and don't cause enough recoil in the originating nuclei to cause damage, α particles, being He nuclei, are heavy enough to have an impact on the structure of matter around them. The most relevant α contaminant is ^{238}U. Recalling its decay chain, shown in figure 6.3,the half-life of its initial event is comparable to the integration time of paleo-detectors, while the remaining half-lives are much quicker. As a result, nearly all of the ^{238}U nuclei that underwent initial decay will have progressed further down the decay chain to stable ^{206}Pb. These events will show up in the material as a series of eight spatially related recoils of the heavy decay chain nuclei followed by eight α tracks. It should be noted that in the target minerals of interest, the usual range of an α with energies of order MeV is greater than a few μm. Even under the pessimistic premise that the damage track from the α-particles does not generate sufficient damage in the target material to be resolved when reading out the material, the distinctive pattern of nuclear recoil tracks can be effectively employed to minimize ^{238}U decay events.

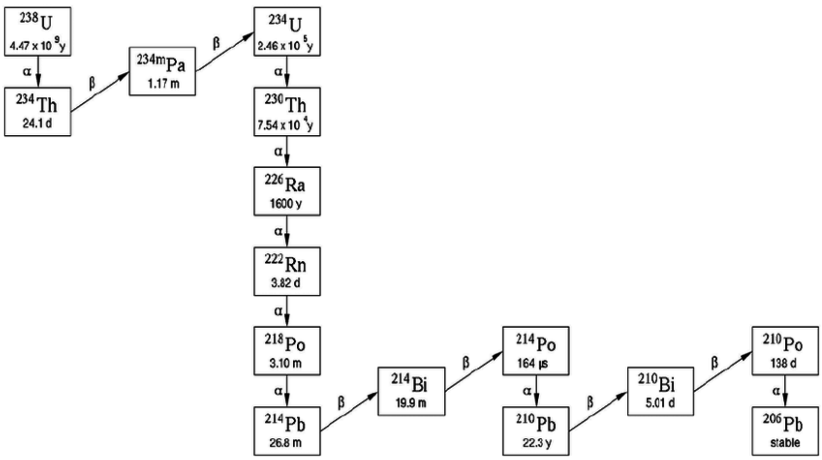

Figure 6.3: Schematics of the decay chain of ^{238}U. From [183]

Another common background comes from neutrons. Neutrons are produced in (α, N) interactions and spontaneous fission. Depending on the composition of the target material one of the components dominates the other: in general, the lighter the composing nuclei, the stronger the (α, N) contribution is. Neutrons lose only a tiny portion of their energy while elastically scattering off heavy nuclei because of the scattering kinematics. However, energy transmission is significantly more effective when scattering off light targets. In particular, fast neutrons will efficiently scatter off hydrogen in a target and lose a significant amount of energy in each interaction because the neutron and proton (i.e., H nuclei) masses are kinematically matched and because the neutron-hydrogen elastic scattering cross section is larger than that of the majority of heavier nuclei. Even while hydrogen only makes up a minor portion of the target molecules, this substantially lowers the amount of intense neutron-induced nuclear recoils, in particular recoils of nuclei heavier than hydrogen. In addition, the hydrogen recoils themselves do not produce detectable tracks depending on the target material and read-out technique.

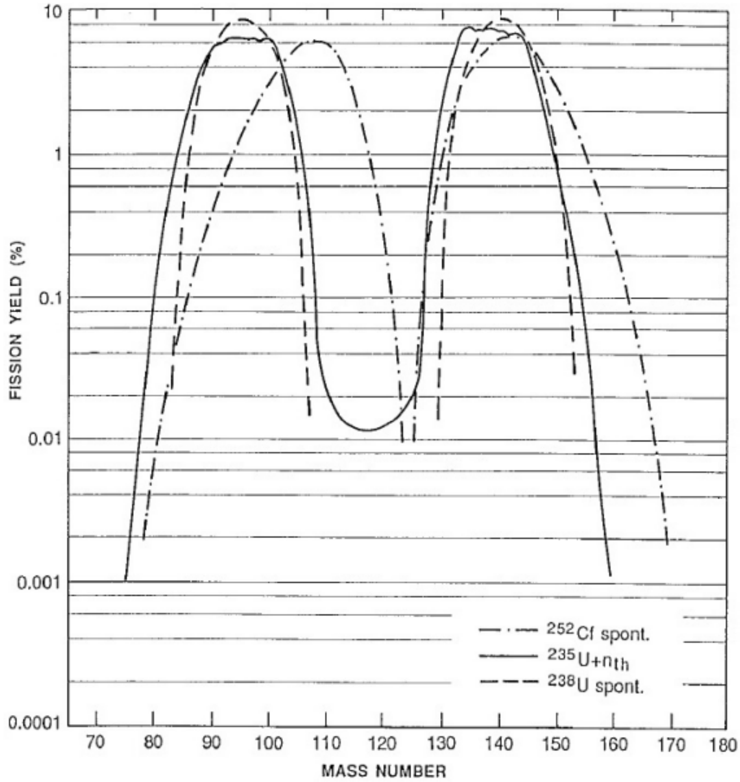

Figure 6.4: Mass distribution of spontaneous fission fragments for ^{238}U and ^{252}Cf, as well as neutron induced fission of ^{235}U. From [184]

Taking into account the considerations made on radioactive contamination, geological history, and composition, some particular minerals were proposed as paleo-detector candidates [179][107]: nchwangite ($Mn_2SiO_3(OH)_2H_2O$), halite (NaCl), epsomite ($MgSO_47(H_2O)$), nickelbischofite ($NiCl_26(H_2O)$), olivine ($(Mg, Fe)_2SiO_4$)) and sinjarite ($CaCl_22(H_2O)$). In this thesis, I also add as a promising candidate the mineral morenosite ($NiSO_47(H_2O)$), which is similar to epsomite with nickel in place of magnesium. Morenosite is one of the minerals frequently present in the Sudbury basin, a region in Canada with peculiar local geology resulting from an asteroid impact occurring 1.85 Gyr ago. The region is famous for its nickel mines and, especially in the scientific community, for hosting SNOLAB, the world's deepest scientific laboratory and site of many pioneering experiments for neutrino and dark matter physics.

6.2 Read-out techniques

Numerous microscopy methods, such as X-ray, electronic, Helium-ion beam, and optical microscopy, have been proposed, or already used to detect the damage caused by nuclear recoils in crystals. The throughput of current microscopy techniques must be increased to enable the effective readout of larger-sized samples in order to fully realize the potential of mineral detectors as detectors for neutrinos and Dark Matter. To illustrate the difficulty, remember that interactions between reactor, solar, or supernova neutrinos as well as from canonical Weakly Interacting Massive Particle (WIMP)-like Dark Matter particles in the mass range of 0.1-10^4 GeV would result in O(0.1-100) keV nuclear recoils. Such nuclear recoils cause damage features in minerals that are O(1)–O(100) nm long. Interactions from atmospheric neutrinos, which generally are of higher energy, could leave longer tracks, O(10) nm -O(100) μm. It is obvious that scanning O(1) kg of material—corresponding to a volume with linear dimensions of order 10 cm—with the necessary spatial resolution is a huge undertaking that will call for the fusion of a variety of microscopy techniques. Furtherly, resolving such size of material with a precision of 1 nm would result in more than a zettabyte of data.

6.2.1 Optical and fluorescence microscopy

The key benefits of optical imaging are its speed and low cost per volume imaged. The resolution and scan speed of microscope techniques also widely vary. While traditional optical microscopy is unable to provide information about sub-micrometer tracks or defects caused by low-energy events, fluorescence microscopy can be utilized to examine nm-sized dislocations; the fastest scan speeds are attained by widefield fluorescence and selective plane-illumination microscopy (SPIM). This technique could also be used in searches for color centers, a phenomenon occurring in certain materials in the presence of tracks.

Traditional optical microscopy could be employed in the search for longer tracks left by the passage of higher energy particles, such as atmospheric neutrinos and muons. In this case, the tracks could be observed in their natural state or etched using chemical solvents, such as fluorhydric acid (HF), to highlight and widen them. The advantage of standard optical microscopy in this case is the low cost and wide range of options, as well as the enormous expertise available, even in the case of more sophisticated technology for automatic scanning.

6.2.2 X-ray

Two main classes of X-ray techniques have been proposed for the detection of the signal contained in paleo-detectors: *imaging* techniques such as coherent diffractive X-ray imaging (CDXI) and *scattering* techniques such as small angle X-ray scattering (SAXS).
X-ray imaging methods may enable fast 2D and 3D reconstruction of samples, much quicker than optical o electronic microscopy. At present-day synchrotron radiation sources, optically opaque samples can be seen with great spatial resolution using proven techniques like hard X-ray radiography. The phase contrast imaging (PCI) technique in particular requires a coherent light source but greatly enhances the visibility of defects too small or faint to be detectable by traditional absorption-based radiography. Currently, available techniques provide a precision of $\approx$ 200 nm. X-ray pictographic microscopy, in which the sample is scanned with a raster pattern by an X-ray source in overlapping regions, and the diffraction pattern is recorded. The main disadvantage of the technique is the extreme precision needed in the motors that direct the illumination beam, increasing time and cost. Another version of CXDI is X-ray holography, in which the phase information is encoded by interference with a reference. The imaging process consists of two diffraction holes, behind one of which the sample is positioned, and a downstream detector that collects the interference between the two diffraction patterns.
In a SAXS device, a monochromatic beam of X-rays is directed at a sample, some of which scatter while the majority pass through the material unaffected. The light typically has a wavelength between 0.07 and 0.2 nm. A detector, often a 2-dimensional flat X-ray detector placed behind the sample perpendicular to the path of the primary beam that first struck the sample, is used to detect the scattering pattern created by the dispersed X-rays. The information about the sample's structure is contained in the scattering

pattern. Separating the weak scattered intensity from the powerful main beam is the main challenge facing SAXS instruments. This becomes more challenging the smaller the desired angle. Depending on the angular range in which the signal is clear, SAXS has a resolution between 1 and 100 nm. This technique is really intriguing for the study of paleo-detectors as the scattering pattern is directly the desired signal, i.e. the distribution of typical sizes of tracks inside the sample; however, it is unclear if the tracks have enough contrast to be detected reliably. An additional problem in scattering, when compared to imaging, is the missing information on the position of the tracks, which could limit the discrimination of the α background.

6.2.3 Helium Ion Beam Microscopy

With the use of helium ion beam microscopy (HIBM), it is possible to read out a slice of a sample that is around 100 nm thick with an impressive 1 nm resolution. By utilizing a laser beam to ablate each layer after readout, a 3D reconstruction of the sample is possible; this option however is only available for smaller samples and destroys the material.

6.3 Proposed signals in paleo-detectors

6.3.1 WIMP dark matter

Weakly interacting massive particles, or WIMPs, constitute the most credible dark matter candidate at this time, and they are also the most frequently employed target in DM direct detection experiments. With a potential signal consisting of an annual modulation, nuclear recoils caused by WIMPs are the focus of the largest ongoing experimental effort for the direct detection of DM.

The paleo-detector method would employ the same strategy as customary man-made experiments for DM detection, i.e., examining the impacts of nuclear recoils, the tracks [107][179][185]. Depending on the impacted atoms, recoils from interaction with WIMPs could have a typical energy between O(1) and O(100) keV, resulting in a track length of 1-100 nm. Therefore, an excess of tracks with these typical sizes would constitute the possible WIMP DM signature, with the precise distribution depending on the WIMP mass. The ability to examine rock samples with sufficient age allows for a large ex-

perimental exposure, which is one of the main benefits of mineral detectors. Even though just a modest sample mass can be analyzed, the O(Gyr) exposure times compensate for this. However, paleo-detectors are fundamentally passive and lack active background mitigation, in contrast to typical direct searches. Therefore, it is essential to comprehend various non-WIMP sources that might provide tracks with a similar length, in particular neutrinos, due to the fact that, like WIMPs, they easily penetrate any overburden and produce recoils of the same size.
Paleo-detector-based DM searches, thanks to their long integration time for the signal, could resolve two scenarios that could cause by current direct detection experiments [181]: variation in the flux with a timescale of O(yr) would be not detectable by man-made experiments, especially in the case of suppression of the signal due to the Earth traversing a region with low DM density, while this effect would be largely smoothed in mineral detectors; on the other hand, in the case of a super-heavy WIMP mass, at fixed DM mass density, the resulting extremely low flux of particles would lower substantially the probability of interactions inside "young" detectors, while paleo-detectors would not lose sensitivity.

6.3.2 Solar neutrinos

The number of elements heavier than helium in the Sun, known as the solar metallicity problem, is one of the most intriguing open questions in solar physics. The development of the Solar Standard Model (SSM) and the detection of various components of the Sun's neutrino emission [186], most recently the measurements by the Borexino experiments of neutrinos from the CNO cycle [187], have shed some light on the physics and conditions inside our star. However, a further understanding of the SSM and star evolution models could be gained by having access to information about the metallicity's evolution across geological time. The paleo-detector method is proposed as the only possible channel for exploring this information at the moment [180]. The most promising channel ^{8}B neutrinos, which have high energy (from 1 Mev to $\approx$ 10 MeV) and a strong dependence on the solar core temperature, making them easier to detect and providing more information about internal activities.

6.3.3 Supernova neutrinos

Over 99 % of the energy produced during core-collapse supernovae is in the form of neutrinos, which typically have energies in the MeV range. Supernova neutrino emission has only ever been investigated once, during the explosion of SN1987a [188], but further research has been rendered impossible by the lack of more recent explosions in the Milky Way or close by. Both Galactic events and the diffuse background of supernovae should be detectable by paleo-detectors [108].

If a Galactic supernova event occurred close to Earth, it may have left a mark that may be seen as an increase in the number of tracks in samples of older materials than the supernova. The technique can be used to extract data about the rate of supernovae in the Milky Way by measuring the absolute rate and its time variance in the last Gyr, which should reflect the rate of supernovae in the Milky Way. This can be used to look for the signature of a specific event, i.e., by taking material from two samples that are similar in age but with a CCSN happening between the formation of one and the other. Also, the extragalactic component of supernova neutrinos, also known as the diffuse Sn background, even if subdominant in flux, could be visible using paleo-detectors and its history and time evolution could give insight into star formation rate in cosmological terms.

6.3.4 Atmospheric neutrinos

As described in chapter 2, as a result of interactions between primary cosmic rays and molecules and atoms in the Earth's atmosphere, a cascade of particles known as EAS is created; it includes pions and kaons, whose decay products include neutrinos, called atmospheric neutrinos. The atmosphere and the top layer of soil primarily absorb the remaining shower's constituent particles, except for very energetic muons. Choosing samples with an overburden larger than ≈ 5 km should ensure shielding also from this component. The much more penetrating neutrinos, on the other hand, might provide paleo-detectors with a source of tracks at any depth. This fact could be used to learn more about the history and development of secondary cosmic ray flux evolution and, as a result, primary cosmic ray flux evolution [189].

Compared to solar or supernova neutrinos, atmospheric neutrinos have higher energy; their spectra peak in the GeV range and go well beyond. This makes it possible for deeper inelastic scattering reactions to transmit more energy to the target nucleus. In addition to recoils, lighter and more energetic pieces are also created. As a result, with estimated statistics of roughly 10^4 tracks/100 g/Gyr, long tracks from atmospheric neutrinos can be separated from radiogenic backgrounds while still delivering a background-free sample. The fact that atmospheric neutrinos serve as one of the main backgrounds for other neutrino analyses provides yet another compelling reason to investigate their effects.

6.3.5 Secondary muons from cosmic rays

Apart from atmospheric neutrinos, high energy muons is the EAS component that penetrates the atmosphere the most, followed by a small number of neutrons and pions that make it to the ground. These elements are a background for all other paleo-detector signals because they can initiate recoils that result in tracks. In fact, they are the main justification offered by the majority of paleo-detector searches for DM or neutrinos that suggest taking samples from beneath significant rock overburdens. Thus for searches focusing on cosmic rays, minerals with vastly different geological histories than the ones selected for neutrino or DM studies must be selected.
As extensively reported in the rest of this thesis cosmic rays are easily observable in the present, hence the usage of paleo-detectors in this context is more interesting for the detection of the evolution of their flux in the past than in measuring the flux itself. The use of paleo-detectors to investigate the flux of cosmic rays necessitates a very thorough understanding of the sample's exposure to secondary cosmic rays. The best-suited samples, in particular, are those that are formed, exposed for a known period of time, and then covered with an overburden of material that blocked the bulk of secondary cosmic rays up to the present. The Halite (NaCl) salt deposits that were created by the temporary partial desiccation of the Mediterranean sea during the so-called *Messinian salinity crisis* [190] are an example of minerals satisfying these conditions, as they were created by precipitation during the evaporation of seawater 6 Myr ago, exposed for a time period of ≈500 kyr and covered in the span of O(10 yr) during the *Zanclean flood* event, which restored the Mediterranean sea and shielded these deposits with several km of water. The usage of these minerals as paleo-detectors will be discussed in

more depth in the next section.

Alternative, comparable conditions may be attained by datable volcanic eruptions buried by subsequent eruptions, which leaves a window for the exposure of the eruption's own minerals or of xenoliths brought to the surface during the volcanic event.

The production of very large (tens, hundreds of μm) tracks is possible because high-energy muons can cause nuclear recoils up to energies of hundreds of keV or more. There are not many of these particles because the muon spectrum decays steeply with energy. Nevertheless, due to the low background present in this region, only composed by spontaneous fission products, the track length range above the μm is highly interesting for observing cosmic ray-induced tracks.

6.4 Case study: neutrinos from local Galactic supernovae

As introduced in the previous section, neutrinos from Galactic or close-by supernova events could be a possible signal source for paleo-detectors. In contrast to extragalactic supernovae, for which a continuous neutrino flux, the DSNB, can be defined, Galactic events are viewed as particle bursts. It is then simple to imagine that a mineral that was formed and stable prior to the supernova was affected by the neutrino burst, resulting in the formation of tracks. A younger sample of the same mineral, on the other hand, will not have the same tracks. In this manner, by comparing the track counts in the length region of interest in two samples of similar but not equal age, ideally one formed just before and one formed just after the event, one could identify the presence of the supernova.

6.4.1 Simulation of the track spectrum

The only available measurement of the neutrino spectrum from a single supernova comes from SN1987a, the only supernova event in the vicinity of the solar system in the last century. The event occurred in the Large Magellanic Cloud, a satellite galaxy of the Milky Way, at a distance of 1.68×10^5 ly (51.4 kpc) and was detected by Kamiokande II, IMB, and Baksan (figure 6.5).

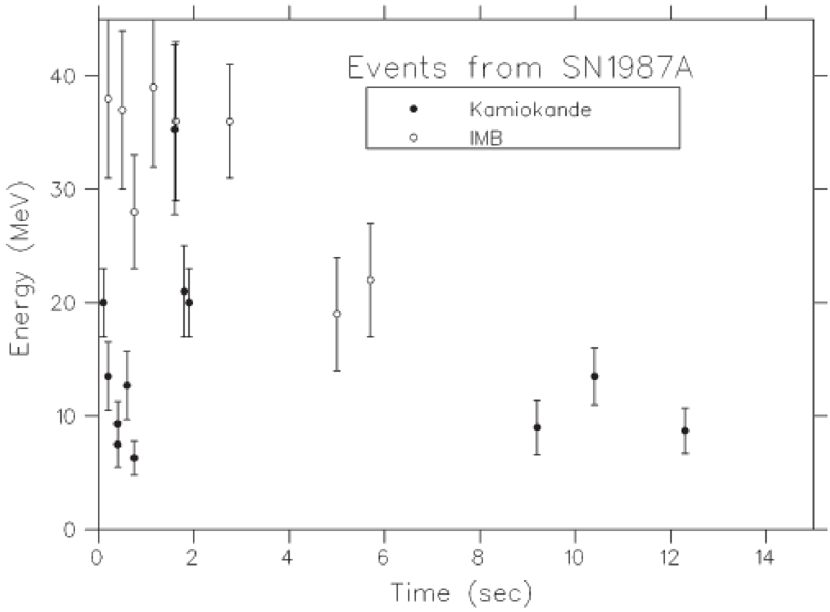

Figure 6.5: The energies and arrival times of the neutrino events from SN 1987A detected in the IMB and Kamiokande detectors. From [191]

To evaluate between historical supernovae which are the best candidates to be detected by paleo-detectors, two main parameters must be taken into account: the age of the supernova and its distance. The distance decreases the flux with the usual $1/r^2$ dependence, while the age of the supernova determines how much the steady fluxes from other sources, such as solar or atmospheric neutrinos, or radiogenic backgrounds, blurs and overcomes the signal from the supernova event. A collection of close and young supernovae is reported in table 6.1, with the associated suppression factor that combines the time suppression of the burst signal and the scaling factor due to distance.

The best candidate selected with this discrimination technique is the supernova remnant RX J0852.04622, also known as *Vela Junior* due to its apparent location inside the larger *Vela Remnant*. This object, at a measured distance around 650-750 ly [192], is one of the closest recorded supernova remnants and with an age of only 800 years, also one of the youngest. I simulated the expected track spectrum from Vela Jr using the dedicated `python` package `paleopy`[193]. As a target mineral I selected morenosite for its favorable background rejection.

Name	Age (yr)	Distance (ly)	Time factor	Distance	Total
SN1987A	34	1.68×10^5	9.3×10^{-9}	1	9.3×10^{-9}
Vela Jr	800	7×10^2	4×10^{-10}	5.8×10^4	2.3×10^{-5}
Geminga	3×10^5	8.15×10^2	9.3×10^{-13}	4.3×10^4	4×10^{-8}
Vela	1.1×10^4	8.15×10^2	2.8×10^{-11}	4.3×10^4	1.2×10^{-6}
Crab	967	6.3×10^3	3.3×10^{-10}	7.1×10^2	2.3×10^{-7}
SN1572	449	7.5×10^3	7.1×10^{-10}	5×10^2	3.5×10^{-7}
SN1006	1×10^3	7.2×10^3	3.1×10^{-10}	5.4×10^2	1.7×10^{-7}

Table 6.1: Local supernova events and their related suppression factors compared to steady sources. The time factor column concerns the ratio between the duration of the event and the time elapsed since. The distance column shows a $1/r^2$ factor. The total column is a combination of the time and distance factors.

6.4.2 Results

Integrating the spectrum in the best-case scenario, i.e. a sample born just before the supernova 800 years ago, shows that there is indeed a region of track length, between 100 nm and 300 nm, in which the signal could dominate over the backgrounds, as visible in figure 6.6. However, the overall normalization shows that the expected number of tracks is exceedingly low, $O(10^{-2})$ per 100 g of material in the area of interest; as such an effective search for this signal would require a huge volume of mineral to be scanned, orders of magnitude greater than feasible with current techniques. The very low number of expected tracks affects also the possibility of reducing the background with the observation of a younger sample, due to the added volume that would need to be analyzed and the high impact of statistical variations.

6.5 Case study: the Messinian Salinity Crisis

A sequence of tectonic processes during the end of the Miocene, specifically between 5.97 and 5.33 Ma, drastically altered the Mediterranean Basin by blocking the entrance to waters from the Atlantic Ocean and turning it into a massive saline basin (figure 6.7). This event is known as the Messinian Salinity Crisis [190] for the impact it had on the salinity of the seas world-

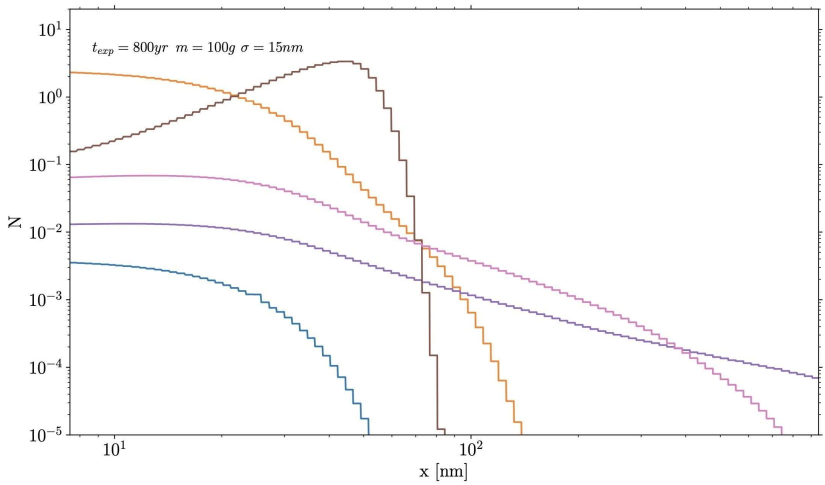

Figure 6.6: Integrated number of tracks from neutrinos coming from the Vela Jr supernova and sources of background for a sample of 100 g of Morenosite formed 800 years ago. Geoneutrinos in blue, solar neutrinos in yellow, thorium decay background in brown, neutron reaction background in purple, Possible signal from a local supernova in pink. The region of track length between 100 and 300 nm shows the highest signal-to-noise ratio.

wide. In the relatively short period of 700 years that water evaporated, salts and minerals that were diluted in it started to coalesce and form crystalline aggregates known as evaporites. Gypsum ($CaSO_4 2(H_2O)$) and halite (NaCl) were the two main evaporite minerals produced during this process. The Zanclean Flood, which occurred at 5.33 Ma in the early Lower Pliocene, covered the evaporites over a period of around 10 years when the Strait of Gibraltar reopened and flooded the basin, in some cases with enough force to drag the deposits to the deepest parts of the Mediterranean, between Sicily and Greece. As previously said, this is precisely the type of environment that is optimal for a paleo-detector search for the signal left by secondary muons and other particles of extensive air showers.

6.5.1 Simulation of muon-induced tracks

For this preliminary explorative work, I focused on the effects of secondary muons on the minerals, as they are by far the most important penetrating component of the showers in terms both of the number and energy content at ground level. Halite was selected as a target, as it was already proposed

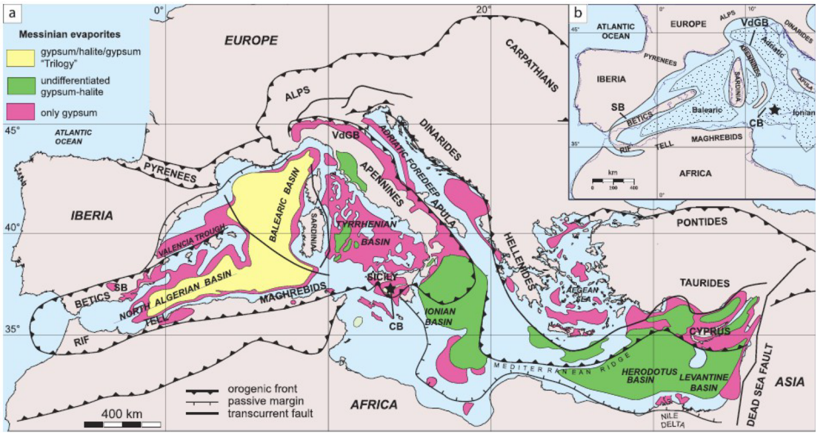

Figure 6.7: A) Map of the Messinian evaporites in the Mediterranean. The term “trilogy” indicates the threefold deeper succession of Western Mediterranean that includes a halite unit sandwiched between two gypsum units. B) Paleoceanographic map of the Western Mediterranean basins during the Messinian salinity crisis, showing the main evaporite depocentres (dotted areas). Emerged areas are in gray. The dotted line is the modern coastline. From [190]

for usage as a paleo-detector, especially because of its typically low radioactive contamination. I started from the measured spectrum of atmospheric muons at earth reported in [194]. The resulting recoil spectra of Na, Cl, and lighter fragments dislocated as an effect of the interactions with muons were obtained using `Geant4` [195], a simulation software for particle matter interactions. This spectrum was then used as an input for `paleopy`, which in turn gave as output the track length spectrum, visible in figure 6.8. As the plot shows the contribution from muons to the track length spectrum is dominant in basically all the regions, and in particular above the μm in length.

6.5.2 Simulation of secondary muon excesses in the past

As current measurements of the secondary cosmic radiation, at sea level or in balloons, cannot give information on its evolution in time for more than, at most, the last 100 years, I have no information on the long-time variations of the atmospheric muon flux and the intensity of cosmic radiation that bombarded the halite sediments that were exposed during the

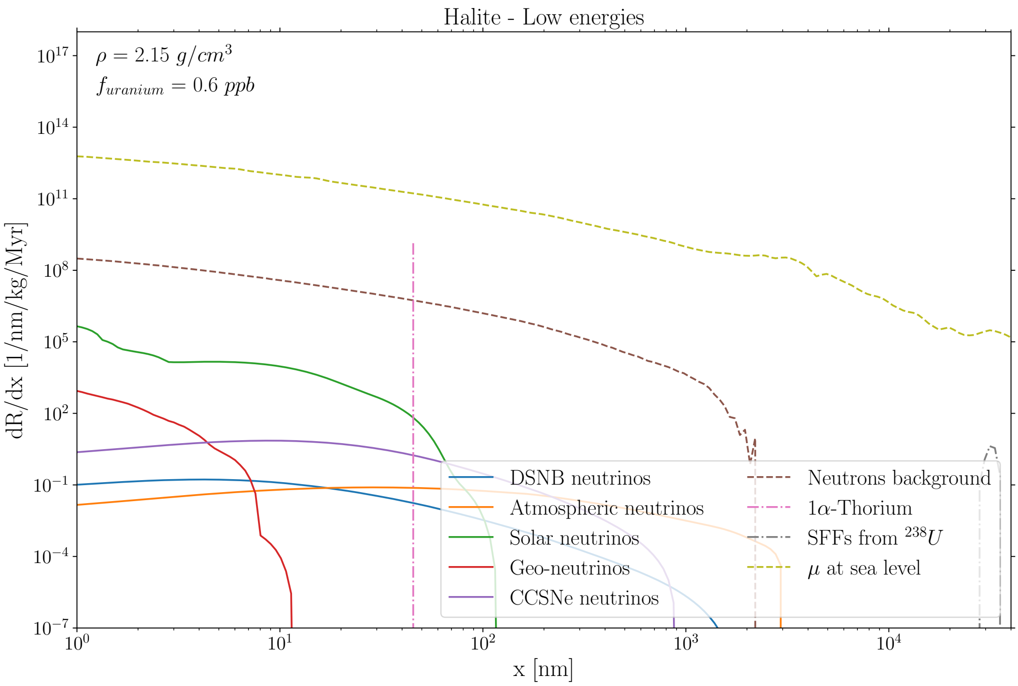

Figure 6.8: Differential track length spectra in halite for all the sources of background and the signal from the spectrum of atmospheric muons reported in [194]

Messinian. It is then of interest to repeat the simulations reported above using different muon spectra. The results of such simulations, in which the flux shape was modified by hardening the spectrum curve with two different spectral indexes, are reported in figure 6.9. From the plot, it is visible that a very strong modification of the muon spectrum is necessary to change the observed track length distribution in the mineral. This effect is mostly due to the dominance of low and medium-energy muons, present in much higher numbers when compared to high-energy ones.

It is to be noted that the plots were obtained by simulating halite deposits in a completely exposed state. It is possible however that the deposits could have been covered by a shallow depth of water (as visible by the map of emerging land in the epoch shown as panel B of figure 6.7), providing enough shielding to affect the lower energy component of the muon spectrum but not the higher energies. Adding a layer of 100 m of water on top of the halite in the `Geant4` simulation shows more discriminating power between

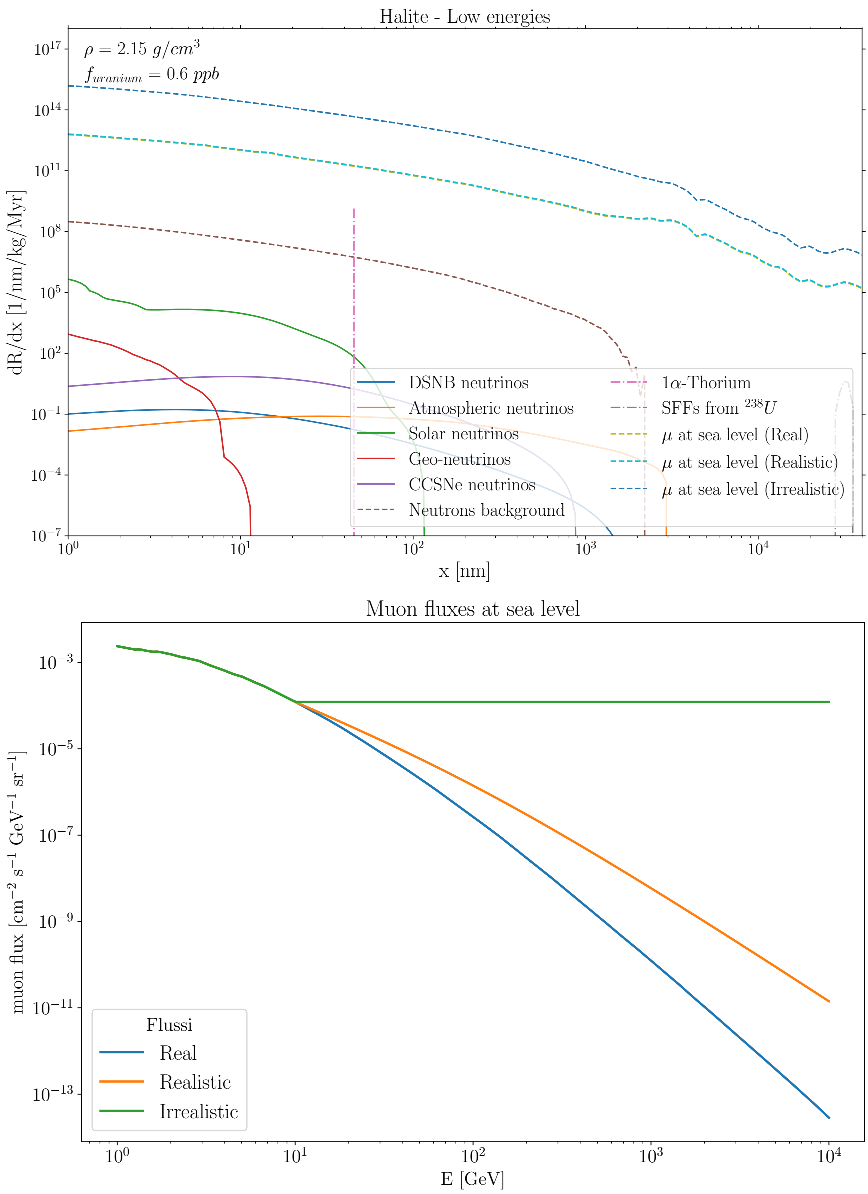

Figure 6.9: Top panel: Differential track length spectra in halite for all the sources of background and the signal from the spectrum of atmospheric muons in three scenarios - currently observed spectrum, harder spectrum ("realistic"), flat spectrum at higher energies ("irrealistic"). Bottom panel: the 3 muon spectra at sea level used to produce the top panel.

the three different simulated spectra, as shown by figure 6.10, at the cost of a lower signal overall. However, while the region of track length under the μm is affected by backgrounds, above that threshold the signal is almost background-free, except for fission tracks.

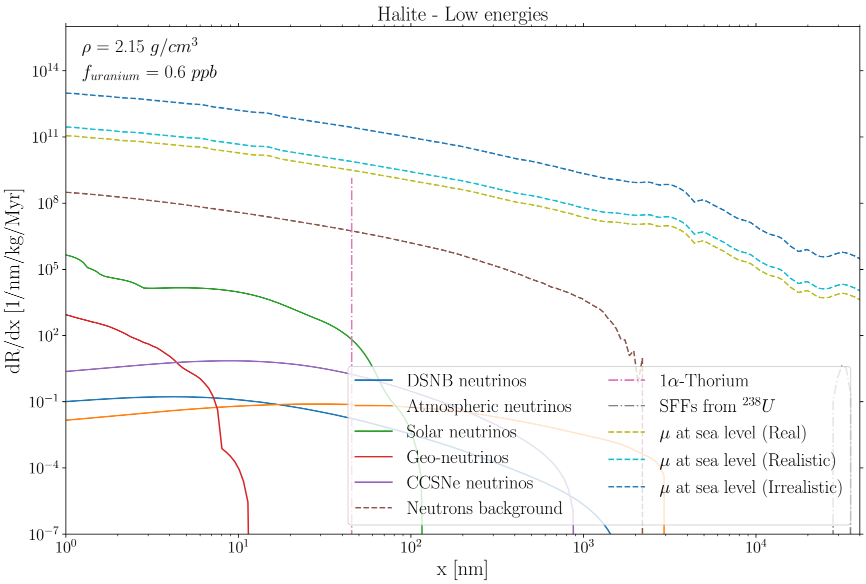

Figure 6.10: Differential track length spectra in halite shielded by 100 m of water, for all the sources of background and the signal from the spectrum of atmospheric muons in three scenarios - currently observed spectrum, harder spectrum ("realistic"), flat spectrum at higher energies ("irrealistic").

Excesses of high-energy muons used to produce the previous plots are of particular interest as they could arise from different atmospheric properties, but also from the presence of an excess in the primary high and ultra-high energy cosmic ray spectrum when compared to the present one. In this optic, I draw attention to the fact that the period of time corresponding to the Messinian Salinity Crisis is serendipitously coincident to the proposed age of the Fermi Bubbles, two large lobes of magnetized plasma observed in γ and X-rays by the Fermi [196] and ROSAT/eRosita satellites [197] [198] respectively. These Galactic structures could be explained as the signature of past AGN-like activity of the Milky Way [199]. If indeed this activity was present in the first period after the creation of these lobes, its effect on Earth could be seen as an increase in the primary cosmic ray spectrum, especially at the highest energies since low energy particles would be trapped by the

Galactic magnetic fields and arrive on Earth with enough delay that the crisis event could already have ended; as a consequence, an increase in the high energy muon flux could be observed at sea level.

Even if further, more precise studies on the water overburden exclude the possibility of observing a variation in the secondary cosmic ray spectrum using halite from the Messinian Salinity Crisis as a paleo-detector, it could still be of great interest to study this particular material for its peculiar geological history and the great opportunity it offers to measure with a novel technique the influx of cosmogenic particles on Earth millions of years ago.

Bibliography

[1] A. A. Penzias and R. W. Wilson. "A Measurement of Excess Antenna Temperature at 4080 Mc/s." In: *Astrophys. J.* 142 (July 1965), pp. 419–421. DOI: 10.1086/148307.

[2] K. Greisen. "End to the cosmic ray spectrum?" In: *Phys. Rev. Lett.* 16 (1966), pp. 748–750. DOI: 10.1103/PhysRevLett.16.748.

[3] G. T. Zatsepin and V. A. Kuzmin. "Upper limit of the spectrum of cosmic rays". In: *JETP Lett.* 4 (1966), pp. 78–80.

[4] High Resolution Fly's Eye Collaboration. "First Observation of the Greisen-Zatsepin-Kuzmin Suppression". In: *Phys. Rev. Lett.* 100 (10 Mar. 2008), p. 101101. DOI: 10.1103/PhysRevLett.100.101101. URL: https://link.aps.org/doi/10.1103/PhysRevLett.100.101101.

[5] URL: https://www.auger.org.

[6] The Pierre Auger Collaboration. "Observation of the Suppression of the Flux of Cosmic Rays above 4 × 10 19 eV". In: *Phys. Rev. Lett.* 101 (Sept. 2008), p. 061101. DOI: 10.1103/PhysRevLett.101.061101.

[7] M. Dova. "Ultra-High Energy Cosmic Rays". In: (Apr. 2016). DOI: 10.5170/CERN-2015-001.169.

[8] T. Abu-Zayyad et al. "The Knee and the Second Knee of the Cosmic-Ray Energy Spectrum". In: (Mar. 2018).

[9] D. De Marco and T. Stanev. "On the shape of the ultrahigh energy cosmic ray spectrum". In: *Phys. Rev. D* 72 (8 Oct. 2005), p. 081301. DOI: 10.1103/PhysRevD.72.081301. URL: https://link.aps.org/doi/10.1103/PhysRevD.72.081301.

[10] R. Aloisio et al. "Signatures of the transition from galactic to extragalactic cosmic rays". In: *Phys. Rev. D* 77 (July 2007). DOI: 10.1103/PHYSREVD.77.025007.

[11] G. Farrar, M. Unger, and L. Anchordoqui. "The origin of the ankle in the UHECR spectrum, and of the extragalactic protons below it". In: *PoS* ICRC2015 (2016), p. 513. DOI: 10.22323/1.236.0513. arXiv: 1512.00484 [astro-ph.HE].

[12] M. Unger, G. Farrar, and L. Anchordoqui. "Origin of the ankle in the ultra-high energy cosmic ray spectrum and of the extragalactic protons below it". In: *Phys. Rev. D* 92 (May 2015). DOI: 10.1103/PhysRevD.92.123001.

[13] M. Unger. "Cosmic Rays above the Knee". In: (Dec. 2008). arXiv: 0812.2763 [astro-ph].

[14] URL: https://ams02.space.

[15] URL: http://dpnc.unige.ch/dampe/.

[16] Y. Asaoka et al. "The CALorimetric Electron Telescope (CALET) on the International Space Station: Results from the First Two Years On Orbit". In: *J. Phys. Conf. Ser.* 1181.1 (2019). Ed. by Anatoly Lagutin, Igor Moskalenko, and M. Panasyuk, p. 012003. DOI: 10.1088/1742-6596/1181/1/012003. arXiv: 1903.07271 [astro-ph.HE].

[17] URL: https://www.iap.kit.edu/kascade/english/index.php.

[18] R. Abbasi et al. "IceTop: The surface component of IceCube". In: *Nucl. Instrum. Meth. A* 700 (2013), pp. 188–220. DOI: 10.1016/j.nima.2012.10.067. arXiv: 1207.6326 [astro-ph.IM].

[19] URL: http://www.telescopearray.org.

[20] M. E. Bertaina. "Cosmic rays from the knee to the ankle". In: *Comptes Rendus Physique* 15.4 (2014). Ultra-high-energy cosmic rays: From the ankle to the tip of the spectrum, pp. 300–308. ISSN: 1631-0705. DOI: https://doi.org/10.1016/j.crhy.2014.03.001. URL: https://www.sciencedirect.com/science/article/pii/S163107051400044

[21] Y. Shirasaki et al. "Chemical composition of primary cosmic rays with energies from 1015 to 1016.5 eV". In: *Astropart. Phys.* 15.4 (2001), pp. 357–381. DOI: 10.1016/S0927-6505(00)00166-3.

[22] S. Ogio et al. "The energy spectrum and the chemical composition of primary cosmic rays with energies from 10**14-eV to 10**16-eV". In: *Astrophys. J.* 612 (2004), pp. 268–275. DOI: 10.1086/422510.

[23] M. Amenomori et al. "Are protons still dominant at the knee of the cosmic-ray energy spectrum?" In: *Phys. Lett. B* 632 (2006), pp. 58–64. DOI: 10.1016/j.physletb.2005.10.048. arXiv: astro-ph/0511469.

[24] W. D. Apel. "Energy Spectra of Elemental Groups of Cosmic Rays: Update on the KASCADE Unfolding Analysis". In: *Astropart. Phys.* 31 (2009), pp. 86–91. DOI: 10.1016/j.astropartphys.2008.11.008. arXiv: 0812.0322 [astro-ph].

[25] The Pierre Auger Collaboration. "Inferences on Mass Composition and Tests of Hadronic Interactions from 0.3 to 100 EeV using the water-Cherenkov Detectors of the Pierre Auger Observatory". In: (Oct. 2017).

[26] R. Abbasi et al. "Mass composition of ultrahigh-energy cosmic rays with the Telescope Array Surface Detector data". In: *Phys. Rev. D* 99.2 (2019), p. 022002. DOI: 10.1103/PhysRevD.99.022002. arXiv: 1808.03680 [astro-ph.HE].

[27] Y. Tsunesada et al. "New air Cherenkov light detectors to study mass composition of cosmic rays with energies above knee region". In: *NUCL INSTRUM METH A* 763 (2014), pp. 320–328. ISSN: 0168-9002. DOI: https://doi.org/10.1016/j.nima.2014.06.054. URL: https://www.sciencedirect.com/science/article/pii/S0168900214007967.

[28] Pijushpani Bhattacharjee and Günter Sigl. "Origin and propagation of extremely high-energy cosmic rays". In: *Physics Reports* 327.3 (2000), pp. 109–247. ISSN: 0370-1573. DOI: https://doi.org/10.1016/S0370-1573(99)00101-5. URL: https://www.sciencedirect.com/science/article/pii/S0370157399001015.

[29] J.-L. Han et al. "The Large - scale galactic magnetic field structure and pulsar rotation measures". In: *ASP Conf. Ser.* 302 (2003). Ed. by Matthew Bailes, D. J. Nice, and Stephen E. Thorsett, p. 253. arXiv: astro-ph/0211197.

[30] URL: https://map.gsfc.nasa.gov.

[31] URL: https://www.cosmos.esa.int/web/planck.

[32] Jansson R. and Farrar G. "A New Model of the Galactic Magnetic Field". In: *Astrophys. J.* 757 (Apr. 2012). DOI: 10.1088/0004-637X/757/1/14.

[33] M. Pshirkov et al. "Deriving global structure of the Galactic Magnetic Field from Faraday Rotation Measures of extragalactic sources". In: *Astrophys. J.* 738 (Mar. 2011). DOI: 10.1088/0004-637X/738/2/192.

[34] Ruth Durrer and Andrii Neronov. "Cosmological Magnetic Fields: Their Generation, Evolution and Observation". In: *Astron. Astrophys. Rev.* 21 (2013), p. 62. DOI: 10.1007/s00159-013-0062-7. arXiv: 1303.7121 [astro-ph.CO].

[35] S. Brown et al. "Limiting Magnetic Fields in the Cosmic Web with Diffuse Radio Emission". In: *Mon. Not. Roy. Astron. Soc.* 468.4 (2017), pp. 4246–4253. DOI: 10.1093/mnras/stx746. arXiv: 1703.07829 [astro-ph.CO].

[36] Takuya Akahori, Dongsu Ryu, and B. M. Gaensler. "Fast Radio Bursts as Probes of Magnetic Fields in the Intergalactic Medium". In: *Astrophys. J.* 824.2 (2016), p. 105. DOI: 10.3847/0004-637X/824/2/105. arXiv: 1602.03235 [astro-ph.CO].

[37] F. Tavecchio et al. "Extreme TeV blazars and the intergalactic magnetic field". In: *Mon. Not. Roy. Astron. Soc.* 414 (2011), p. 3566. DOI: 10.1111/j.1365-2966.2011.18657.x. arXiv: 1009.1048 [astro-ph.HE].

[38] J. D. Bray and A. M. M. Scaife. "An upper limit on the strength of the extragalactic magnetic field from ultra-high-energy cosmic-ray anisotropy". In: *Astrophys. J.* 861.1 (2018), p. 3. DOI: 10.3847/1538-4357/aac777. arXiv: 1805.07995 [astro-ph.CO].

[39] A. Letessier-Selvon and T. Stanev. "Ultrahigh Energy Cosmic Rays". In: *Reviews of Modern Physics* 83 (Feb. 2011). DOI: 10.1103/RevModPhys.83.907.

[40] D. J. Fixsen et al. "The Cosmic Microwave Background spectrum from the full COBE FIRAS data set". In: *Astrophys. J.* 473 (1996), p. 576. DOI: 10.1086/178173. arXiv: astro-ph/9605054.

[41] Jean-Loup Puget, Floyd Stecker, and J. Bredekamp. "Photonuclear interactions of ultrahigh energy cosmic rays and their astrophysical consequences. [Cross sections, Monte Carlo calculations]". In: *The Astrophysical Journal* 205 (May 1976). DOI: 10.1086/154321.

[42] D. Harari. "The flux suppression at the highest energies". In: *Comptes Rendus Physique* 15 (Apr. 2014). DOI: 10.1016/j.crhy.2014.02.011.

[43] D. Allard. "Extragalactic propagation of ultrahigh energy cosmic-rays". In: *Astropart. Phys.* 39-40 (2012), pp. 33–43. DOI: 10.1016/j.astropartphys.2011.10.011. arXiv: 1111.3290 [astro-ph.HE].

[44] A. de Angelis, G. Galanti, and M. Roncadelli. "Transparency of the Universe to gamma rays". In: *Monthly Notices of the Royal Astronomical Society* 432 (Feb. 2013). DOI: 10.1093/mnras/stt684.

[45] G. Gelmini, Oleg E. Kalashev, and D. V. Semikoz. "GZK photons as ultra high energy cosmic rays". In: *J. Exp. Theor. Phys.* 106 (2008), pp. 1061–1082. DOI: 10.1134/S106377610806006X. arXiv: astro-ph/0506128.

[46] the Pierre Auger Collaboration. "Search for photons with energies above 10^{18} eV using the hybrid detector of the Pierre Auger Observatory". In: *J COSMOL ASTROPART P* 04 (2017). [Erratum: JCAP 09, E02 (2020)], p. 009. DOI: 10.1088/1475-7516/2017/04/009. arXiv: 1612.01517 [astro-ph.HE].

[47] L. Yacobi, D. Guetta, and E. Behar. "Implication of the Non-detection of gzk Neutrinos". In: *Astrophys. J.* 823.2 (2016), p. 89. DOI: 10.3847/0004-637X/823/2/89. arXiv: 1510.01244 [astro-ph.HE].

[48] the Pierre Auger Collaboration. "Limits on point-like sources of ultra-high-energy neutrinos with the Pierre Auger Observatory". In: *J COSMOL ASTROPART P* 11 (2019), p. 004. DOI: 10.1088/1475-7516/2019/11/004. arXiv: 1906.07419 [astro-ph.HE].

[49] URL: https://grand.cnrs.fr.

[50] R. Iuppa. "Anisotropy in the cosmic radiation at TeV energy". In: *Frascati Phys. Ser.* 55 (2012), pp. 61–66. arXiv: 1302.7184 [astro-ph.HE].

[51] M. Amenomori et al. "Anisotropy and Corotation of Galactic Cosmic Rays". In: *Science* 314.5798 (2006), pp. 439–443. DOI: 10.1126/science.1131702. eprint: https://www.science.org/doi/pdf/10.1126/science.1131702. URL: https://www.science.org/doi/abs/10.1126/science.1131702.

[52] A. Abdo et al. "The Large-Scale Cosmic-Ray Anisotropy as Observed with Milagro". In: *Astrophys. J.* 698 (June 2009), p. 2121. DOI: 10.1088/0004-637X/698/2/2121.

[53] P. Desiati. "Observation of TeV-PeV cosmic ray anisotropy with IceCube, IceTop and AMANDA". In: *NUCL INSTRUM METH A* 742 (Aug. 2013). DOI: 10.1016/j.nima.2013.12.028.

[54] A. U. Abeysekara et al. "Observation of Anisotropy of TeV Cosmic Rays with Two Years of HAWC". In: *Astrophys. J.* 865.1 (2018), p. 57. DOI: 10.3847/1538-4357/aad90c. arXiv: 1805.01847 [astro-ph.HE].

[55] A. Chiavassa et al. "Studies of the cosmic ray spectrum and large scale anisotropies with the KASCADE-Grande experiment". In: *J Phys: Conference Series* 531 (Aug. 2014), p. 012001. DOI: 10.1088/1742-6596/531/1/012001.

[56] the Pierre Auger Collaboration. "Observation of a Large-scale Anisotropy in the Arrival Directions of Cosmic Rays above 8×10^{18} eV". In: *Science* 357.6537 (2017), pp. 1266–1270. DOI: 10.1126/science.aan4338. arXiv: 1709.07321 [astro-ph.HE].

[57] A. M. Hillas. "The Origin of Ultra-High-Energy Cosmic Rays". In: *Annual Review of Astronomy and Astrophysics* 22.1 (1984), pp. 425–444. DOI: 10.1146/annurev.aa.22.090184.002233. eprint: https://doi.org/10.1146/annurev.aa.22.090184.002233. URL: https://doi.org/10.1146/annurev.aa.22.090184.002233.

[58] E. Fermi. "On the Origin of the Cosmic Radiation". In: *Phys. Rev.* 75 (8 Apr. 1949), pp. 1169–1174. DOI: `10.1103/PhysRev.75.1169`. URL: `https://link.aps.org/doi/10.1103/PhysRev.75.1169`.

[59] M. Ackermann et al. "Detection of the Characteristic Pion-Decay Signature in Supernova Remnants". In: *Science* 339 (2013), p. 807. DOI: `10.1126/science.1231160`. arXiv: `1302.3307 [astro-ph.HE]`.

[60] Z. Cao et al. "Ultrahigh-energy photons up to 1.4 petaelectronvolts from 12 γ-ray Galactic sources". In: *Nature* 594 (June 2021). DOI: `10.1038/s41586-021-03498-z`.

[61] E. Amato. "The origin of galactic cosmic rays". In: *International Journal of Modern Physics D* 23 (June 2014). DOI: `10.1142/S0218271814300134`

[62] F. Halzen and E. Zas. "Neutrino fluxes from active galaxies: A Model independent estimate". In: *Astrophys. J.* 488 (1997), pp. 669–674. DOI: `10.1086/304741`. arXiv: `astro-ph/9702193`.

[63] V Beckmann and C SHRADER. "The AGN phenomenon: open issues". In: July 2013, p. 069. DOI: `10.22323/1.176.0069`.

[64] B. Fanaroff and J. Riley. "The Morphology of Extragalactic Radio Sources of High and Low Luminosity". In: *Monthly Notices of the Royal Astronomical Society* 167 (Apr. 1974), 31P–36P. DOI: `10.1093/mnras/167.1.31P`.

[65] G. E. Romero, A. L. Müller, and M. Roth. "Particle acceleration in the superwinds of starburst galaxies". In: *Astron. Astrophys.* 616 (2018), A57. DOI: `10.1051/0004-6361/201832666`. arXiv: `1801.06483 [astro-ph.HE]`.

[66] L. A. Anchordoqui and J. F. Soriano. "Evidence for UHECR origin in starburst galaxies". In: *PoS* ICRC2019.255 (2021), p. 255. DOI: `10.22323/1.358.0255`. arXiv: `1905.13243 [astro-ph.HE]`.

[67] D. Strickland et al. "Starburst Galaxies: Outflows of Metals and Energy into the IGM". In: (Mar. 2009).

[68] B. P. Abbott, R. Abbott, and T. D. Abbott et al. "Multi-messenger Observations of a Binary Neutron Star Merger". In: *Astrophys. J. Lett.* 848.2 (Oct. 2017), p. L12. DOI: `10.3847/2041-8213/aa91c9`. URL: `https://dx.doi.org/10.3847/2041-8213/aa91c9`.

[69] K. Kotera and A. V. Olinto. “The Astrophysics of Ultrahigh-Energy Cosmic Rays”. In: *Annual Review of Astronomy and Astrophysics* 49 (2011), pp. 119–153.

[70] G. Ghisellini et al. “Ultra-High Energy Cosmic Rays, Spiral galaxies and Magnetars”. In: *Mon. Not. Roy. Astron. Soc.* 390 (2008), pp. L88–L92. DOI: `10.1111/j.1745-3933.2008.00547.x`. arXiv: `0806.2393 [astro-ph]`.

[71] W. Heitler. *The quantum theory of radiation.* Vol. 5. International Series of Monographs on Physics. Oxford: Oxford University Press, 1936.

[72] J. Matthews. “A Heitler model of extensive air showers”. In: *Astroparticle Physics* 22.5 (2005), pp. 387–397. ISSN: 0927-6505. DOI: `https://doi.org/10.1016/j.astropartphys.2004.09.003`. URL: `https://www.sciencedirect.com/science/article/pii/S0927650504001598`.

[73] S. Messina. “Extension to lower energies of the cosmic-ray energy window at the Pierre Auger Observatory”. English. PhD thesis. University of Groningen, 2016. ISBN: 978-94-028-0286-3.

[74] R. Engel, D. Heck, and T. Pierog. “Extensive air showers and hadronic interactions at high energy”. In: *Ann. Rev. Nucl. Part. Sci.* 61 (2011), pp. 467–489. DOI: `10.1146/annurev.nucl.012809.104544`.

[75] D. Heck et al. “CORSIKA: A Monte C. code to simulate extensive air showers”. In: (Feb. 1998).

[76] G. Battistoni et al. “The FLUKA code: An accurate simulation tool for particle therapy”. In: *Frontiers in Oncology* 6 (May 2016). DOI: `10.3389/fonc.2016.00116`.

[77] H. Fesefeldt. “The Simulation of Hadronic Showers: Physics and Applications”. In: (Dec. 1985).

[78] H. Petersen et al. “UrQMD v2.3: Changes and Comparisons”. In: (May 2008). arXiv: `0805.0567 [hep-ph]`.

[79] S. Ostapchenko. “QGSJET-III model: physics and preliminary results”. In: *EPJ Web Conf.* 208 (2019). Ed. by B. Pattison et al., p. 11001. DOI: `10.1051/epjconf/201920811001`.

[80] T. Pierog et al. "EPOS LHC : test of collective hadronization with LHC data". In: *Phys. Rev. C* 92 (June 2013). DOI: 10.1103/PhysRevC.92.034906.

[81] F. Riehn et al. "Hadronic interaction model Sibyll 2.3d and extensive air showers". In: *Phys. Rev. D* 102.6 (2020), p. 063002. DOI: 10.1103/PhysRevD.102.063002. arXiv: 1912.03300 [hep-ph].

[82] J. Linsley. "Evidence for a primary cosmic-ray particle with energy 10**20-eV". In: *Phys. Rev. Lett.* 10 (1963), pp. 146–148. DOI: 10.1103/PhysRevLett.10.146.

[83] N. Chiba et al. "Akeno giant air shower array (AGASA) covering 100-km**2 area". In: *Nucl. Instrum. Meth. A* 311 (1992), pp. 338–349. DOI: 10.1016/0168-9002(92)90882-5.

[84] "Multicomponent EAS observations from EAS-TOP and LVD at Gran Sasso". In: *Nucl. Phys. B Proc. Suppl.* 35 (1994). Ed. by C. Arpesella, E. Bellotti, and A. Bottino, pp. 259–260. DOI: 10.1016/0920-5632(94)90256-9.

[85] G. Di Sciascio. "The LHAASO experiment: From Gamma-Ray Astronomy to Cosmic Rays". In: *Nuclear and Particle Physics Proceedings* 279-281 (2016). Proceedings of the 9th Cosmic Ray International Seminar, pp. 166–173. ISSN: 2405-6014. DOI: https://doi.org/10.1016/j.nuclphysbps.2016.10.024. URL: https://www.sciencedirect.com/science/article/pii/S240560141630205X.

[86] Gaurang B. Yodh. "The MILAGRO gamma ray observatory". In: *Nuclear Physics B - Proceedings Supplements* 52.3 (1997), pp. 264–268. ISSN: 0920-5632. DOI: https://doi.org/10.1016/S0920-5632(96)00902-4. URL: https://www.sciencedirect.com/science/article/pii/S0920563296009024.

[87] URL: https://www.hawc-observatory.org/.

[88] URL: https://www.swgo.org/SWGOWiki/doku.php.

[89] the Pierre Auger Collaboration. "AugerPrime: the Pierre Auger Observatory Upgrade". In: *EPJ Web Conf.* 210 (2019), p. 06002. DOI: 10.1051/epjconf/201921006002. arXiv: 1905.04472 [astro-ph.HE].

[90] D. Ferenc. “The MAGIC gamma-ray observatory”. In: *Nucl. Instrum. Meth. A* 553 (2005). Ed. by J. Engelfried and G. Paic, pp. 274–281. DOI: 10.1016/j.nima.2005.08.085.

[91] URL: https://www.mpi-hd.mpg.de/hfm/HESS/.

[92] J. A. Hinton. “The Status of the H.E.S.S. project”. In: *New Astron. Rev.* 48 (2004), pp. 331–337. DOI: 10.1016/j.newar.2003.12.004. arXiv: astro-ph/0403052.

[93] URL: https://www.cta-observatory.org/.

[94] G. Archbold et al. “Overview of the High Resolution Fly’s Eye Cosmic Ray Observatory”. In: (Jan. 2000).

[95] T. Huege. “Simulations and theory of radio emission from cosmic ray air showers”. In: *NUCL INSTRUM METH A* 604 (Mar. 2009). DOI: 10.1016/j.nima.2009.03.165.

[96] D. Ardouin et al. “Radioelectric Field Features of Extensive Air Showers Observed with CODALEMA”. In: *Astropart. Phys.* 26 (2006), pp. 341–350. DOI: 10.1016/j.astropartphys.2006.07.002. arXiv: astro-ph/0608550.

[97] T. Huege et al. “Radio detection of cosmic ray air showers with LOPES”. In: *Nuclear Physics B - Proceedings Supplements* 165 (Mar. 2007), pp. 341–348. DOI: 10.1016/j.nuclphysbps.2006.11.046.

[98] D. Kostunin et al. “Seven years of Tunka-Rex operation”. In: (Aug. 2019).

[99] J.L. Kelley and P. Auger. “AERA: The auger engineering radio array”. In: *Proceedings of the 32nd International Cosmic Ray Conference, ICRC 2011* 3 (Jan. 2011), pp. 112–115. DOI: 10.7529/ICRC2011/V03/0556.

[100] van Haarlem, M. P. et al. “LOFAR: The LOw-Frequency ARray”. In: *A&A* 556 (2013), A2. DOI: 10.1051/0004-6361/201220873. URL: https://doi.org/10.1051/0004-6361/201220873.

[101] URL: https://www.skao.int/.

[102] D. A. Glaser. “Some Effects of Ionizing Radiation on the Formation of Bubbles in Liquids”. In: *Phys. Rev.* (1952).

[103] URL: https://icecube.wisc.edu/.

[104] URL: https://www.km3net.org/.

[105] URL: https://baikalgvd.jinr.ru/.

[106] A. Albert et al. "ANTARES search for point-sources of neutrinos using astrophysical catalogs: a likelihood stacking analysis". In: (Dec. 2020).

[107] T. Edwards et al. "Digging for dark matter: Spectral analysis and discovery potential of paleo-detectors". In: *Phys. Rev. D.* 99 (2019). DOI: 10.1103/PhysRevD.99.043541..

[108] S. Baum et al. "Paleodetectors for Galactic supernova neutrinos". In: *Phys. Rev. D* 101.10 (2020), p. 103017. DOI: 10.1103/PhysRevD.101.103017. arXiv: 1906.05800 [astro-ph.GA].

[109] Pierre Auger Collaboration. "The Pierre Auger Cosmic Ray Observatory". In: *NUCL INSTRUM METH A* 798 (2015), pp. 172–213. ISSN: 0168-9002. DOI: https://doi.org/10.1016/j.nima.2015.06.058. URL: https://www.sciencedirect.com/science/article/pii/S0168900215008086.

[110] Pierre Auger Collaboration. "Trigger and aperture of the surface detector array of the Pierre Auger Observatory". In: *NUCL INSTRUM METH A* 613.1 (2010), pp. 29–39. ISSN: 0168-9002. DOI: https://doi.org/10.1016/j.nima.2009.11.018. URL: https://www.sciencedirect.com/science/article/pii/S0168900209021688.

[111] Pierre Auger Collaboration. "Reconstruction of inclined air showers detected with the Pierre Auger Observatory". In: *J COSMOL ASTROPART P* 2014.08 (Aug. 2014), pp. 019–019. DOI: 10.1088/1475-7516/2014/08/019. URL: https://doi.org/10.1088/1475-7516/2014/08/019.

[112] J. Nishimura K. Kamata. "The Lateral and the Angular Structure Functions of Electron Showers". In: *Progress of Theoretical Physics . . .* (1958).

[113] K. Greisen. In: *Progress in Cosmic Ray Physics* 3 (1956).

[114] the Pierre Auger Collaboration. "Reconstruction of events recorded with the surface detector of the Pierre Auger Observatory". In: *JINST* 15.10 (2020), P10021. DOI: 10.1088/1748-0221/15/10/P10021. arXiv: 2007.09035 [astro-ph.IM].

[115] the Pierre Auger Collaboration. "Energy spectrum of cosmic rays measured using the Pierre Auger Observatory". In: July 2021, p. 324. DOI: 10.22323/1.395.0324.

[116] T. K. Gaisser and A. M. Hillas. "Reliability of the method of constant intensity cuts for reconstructing the average development of vertical showers". In: 1977.

[117] the Pierre Auger Collaboration. "The Pierre Auger Observatory Upgrade - Preliminary Design Report". In: (Apr. 2016).

[118] the Pierre Auger Collaboration. "Energy spectrum of cosmic rays measured using the Pierre Auger Observatory". In: July 2021, p. 324. DOI: 10.22323/1.395.0324.

[119] Pierre Auger Collaboration. "Features of the Energy Spectrum of Cosmic Rays above 2.5×10^{18} eV Using the Pierre Auger Observatory". In: *Prl* 125 (12 Sept. 2020), p. 121106. DOI: 10.1103/PhysRevLett.125.121106. URL: https://link.aps.org/doi/10.1103/PhysRevLett.125.121106.

[120] Alexey Yushkov. "Mass Composition of Cosmic Rays with Energies above $10^{17.2}$ eV from the Hybrid Data of the Pierre Auger Observatory". In: *PoS* ICRC2019 (2020), p. 482. DOI: 10.22323/1.358.0482.

[121] C.s J. Todero Peixoto. "Estimating the Depth of Shower Maximum using the Surface Detectors of the Pierre Auger Observatory". In: *PoS* ICRC2019 (2019), p. 440. DOI: 10.22323/1.358.0440.

[122] P. Abreu et al. "The depth of the shower maximum of air showers measured with AERA". In: July 2021, p. 387. DOI: 10.22323/1.395.0387.

[123] the Pierre Auger Collaboration. "Combined fit of the energy spectrum and mass composition across the ankle with the data measured at the Pierre Auger Observatory". In: July 2021, p. 311. DOI: 10.22323/1.395.0311.

[124] the peirre Auger Collaboration. "Indication of a mass-dependent anisotropy above $10^{18.7}$ eV in the hybrid data of the Pierre Auger Observatory". In: *PoS* ICRC2021 (2021), p. 321. DOI: 10.22323/1.395.0321.

[125] the Pierre Auger Collaboration. "A search for ultra-high-energy photons at the Pierre Auger Observatory exploiting air-shower universality". In: *PoS* ICRC2021 (2021), p. 373. DOI: 10.22323/1.395.0373.

[126] the Pierre Auger Collaboration. "Probing the origin of ultra-high-energy cosmic rays with neutrinos in the EeV energy range using the Pierre Auger Observatory". In: *J COSMOL ASTROPART P* 10 (2019), p. 022. DOI: 10.1088/1475-7516/2019/10/022. arXiv: 1906.07422 [astro-ph.HE].

[127] the Pierre Auger Collaboration. "A Search for Point Sources of EeV Neutrons". In: *Astrophys. J.* 760 (2012), p. 148. DOI: 10.1088/0004-637X/760/2/148. arXiv: 1211.4901 [astro-ph.HE].

[128] The Pierre auger Collaboration. "A Targeted Search for Point Sources of EeV Neutrons". In: *Astrophys. J. Lett.* 789 (2014), p. L34. DOI: 10.1088/2041-8205/789/2/L34. arXiv: 1406.4038 [astro-ph.HE].

[129] R. Almeida et al. "Large-scale and multipolar anisotropies of cosmic rays detected at the Pierre Auger Observatory with energies above 4 EeV". In: July 2021, p. 335. DOI: 10.22323/1.395.0335.

[130] the Pierre Auger Collaboration. "Arrival Directions of Cosmic Rays above 32 EeV from Phase One of the Pierre Auger Observatory". In: *Astrophys. J.* 935.2 (2022), p. 170. DOI: 10.3847/1538-4357/ac7d4e. arXiv: 2206.13492 [astro-ph.HE].

[131] Pierre Auger Collaboration. "Reconstruction of events recorded with the surface detector of the Pierre Auger Observatory". In: *J. Instrum.* 15.10 (Oct. 2020), P10021. DOI: 10.1088/1748-0221/15/10/P10021. arXiv: 2007.09035 [astro-ph.IM].

[132] Paul Sommers. "Cosmic Ray Anisotropy Analysis with a Full-Sky Observatory". In: *Astroparticle Physics* 14 (Jan. 2001), pp. 271–286. DOI: 10.1016/S0927-6505(00)00130-4.

[133] Pierre Auger Collaboration. "Searches for Anisotropies in the Arrival Directions of the Highest Energy Cosmic Rays Detected by the Pierre Auger Observatory". In: *Astrophys. J.* 804.1, 15 (May 2015), p. 15. DOI: 10.1088/0004-637X/804/1/15. arXiv: 1411.6111 [astro-ph.HE].

[134] the Pierre Auger Collaboration. "A Catalog of the Highest-Energy Cosmic Rays Recorded During Phase I of Operation of the Pierre Auger Observatory". In: (Nov. 2022). arXiv: 2211.16020 [astro-ph.HE].

[135] Rafael Alves Batista et al. "Open questions in cosmic-ray research at ultrahigh energies". In: *Frontiers in Astronomy and Space Sciences* 6, 23 (June 2019), p. 23. DOI: 10.3389/fspas.2019.00023. arXiv: 1903.06714 [astro-ph.HE].

[136] M. Erdmann et al. "The nuclear window to the extragalactic universe". In: *Astropart. Phys.* 85 (Dec. 2016), pp. 54–64. DOI: 10.1016/j.astropartphys.2016.10.002. arXiv: 1607.01645 [astro-ph.HE].

[137] Pierre Auger Collaboration. "Observation of a large-scale anisotropy in the arrival directions of cosmic rays above 8 &#xd7, 10¡sup¿18¡/sup¿ eV". In: *Science* 357.6357 (2017), pp. 1266–1270. DOI: 10.1126/science.aan4338. eprint: https://www.science.org/doi/pdf/10.1126/science.aan4338. URL: https://www.science.org/doi/abs/10.1126/science.aan4338.

[138] Pierre Auger Collaboration. "An Indication of Anisotropy in Arrival Directions of Ultra-high-energy Cosmic Rays through Comparison to the Flux Pattern of Extragalactic Gamma-Ray Sources". In: *Astrophys. J. Lett.* 853.2, L29 (Feb. 2018), p. L29. DOI: 10.3847/2041-8213/aaa66d. arXiv: 1801.06160 [astro-ph.HE].

[139] K. M. Górski et al. "HEALPix: A Framework for High-Resolution Discretization and Fast Analysis of Data Distributed on the Sphere". In: *Astrophys. J.* 622.2 (Apr. 2005), pp. 759–771. DOI: 10.1086/427976. arXiv: astro-ph/0409513 [astro-ph].

[140] T. -P. Li and Y. -Q. Ma. "Analysis methods for results in gamma-ray astronomy." In: *Astrophys. J.* 272 (Sept. 1983), pp. 317–324. DOI: 10.1086/161295.

[141] J. P. Huchra et al. "The 2MASS Redshift Survey—Description and Data Release". In: *Astrophys. J. Suppl. S* 199.2, 26 (Apr. 2012), p. 26. DOI: 10.1088/0067-0049/199/2/26. arXiv: 1108.0669 [astro-ph.CO].

[142] W. H. Baumgartner et al. "The 70 Month Swift-BAT All-sky Hard X-Ray Survey". In: *Astrophys. J. Suppl. S* 207.2, 19 (Aug. 2013), p. 19. DOI: 10.1088/0067-0049/207/2/19. arXiv: 1212.3336 [astro-ph.HE].

[143] Sjoert van Velzen et al. "Radio galaxies of the local universe. All-sky catalog, luminosity functions, and clustering". In: *aap* 544, A18 (Aug. 2012), A18. DOI: 10.1051/0004-6361/201219389. arXiv: 1206.0031 [astro-ph.CO].

[144] M. Ajello et al. "The Origin of the Extragalactic Gamma-Ray Background and Implications for Dark Matter Annihilation". In: *Astrophys. J. Lett.* 800.2, L27 (Feb. 2015), p. L27. DOI: 10.1088/2041-8205/800/2/L27. arXiv: 1501.05301 [astro-ph.HE].

[145] Matt A. Roth et al. "The diffuse γ-ray background is dominated by star-forming galaxies". In: *Nature* 597.7876 (Sept. 2021), pp. 341–344. DOI: 10.1038/s41586-021-03802-x. arXiv: 2109.07598 [astro-ph.HE].

[146] M. F. Skrutskie et al. "The Two Micron All Sky Survey (2MASS)". In: *aj* 131.2 (Feb. 2006), pp. 1163–1183. DOI: 10.1086/498708.

[147] D. Makarov et al. "HyperLEDA. III. The catalogue of extragalactic distances". In: *aap* 570, A13 (Oct. 2014), A13. DOI: 10.1051/0004-6361/201423496. arXiv: 1408.3476 [astro-ph.GA].

[148] C. Lunardini et al. "Are starburst galaxies a common source of high energy neutrinos and cosmic rays?" In: *J COSMOL ASTROPART P* 2019.10, 073 (Oct. 2019), p. 073. DOI: 10.1088/1475-7516/2019/10/073. arXiv: 1902.09663 [astro-ph.HE].

[149] D. B. Sanders et al. "The IRAS Revised Bright Galaxy Sample". In: *aj* 126.4 (Oct. 2003), pp. 1607–1664. DOI: 10.1086/376841. arXiv: astro-ph/0306263 [astro-ph].

[150] J. J. Condon et al. "The NRAO VLA Sky Survey". In: *aj* 115.5 (May 1998), pp. 1693–1716. DOI: 10.1086/300337.

[151] M.R. Calabretta, Lister Staveley-Smith, and D. G. Barnes. "A New 1.4 GHz Radio Continuum Map of the Sky South of Declination +25°". In: *pasa* 31, e007 (Jan. 2014), e007. DOI: 10.1017/pasa.2013.36. arXiv: 1310.2414 [astro-ph.IM].

[152] A. E. Wright and R. Otrupcek. “VizieR Online Data Catalog: Parkes Radio Sources Catalogue (PKSCAT90) (Wright+ 1990)”. In: *VizieR Online Data Catalog*, VIII/15 (May 1996), pp. VIII/15.

[153] Kyuseok Oh, M. Koss, C. B. Markwardt, et al. “The 105-Month Swift-BAT All-sky Hard X-Ray Survey”. In: *Astrophys. J. Suppl. S* 235.1, 4 (Mar. 2018), p. 4. DOI: 10.3847/1538-4365/aaa7fd. arXiv: 1801.01882 [astro-ph.HE].

[154] Fermi-LAT Collaboration. “3FHL: The Third Catalog of Hard Fermi-LAT Sources”. In: *Astrophys. J. Suppl. S* 232.2, 18 (Oct. 2017), p. 18. DOI: 10.3847/1538-4365/aa8221. arXiv: 1702.00664 [astro-ph.HE].

[155] Pierre Auger Collaboration. “Combined fit of spectrum and composition data as measured by the Pierre Auger Observatory”. In: *J COSMOL ASTROPART P* 2017.4, 038 (Apr. 2017), p. 038. DOI: 10.1088/1475-7516/2017/04/038. arXiv: 1612.07155 [astro-ph.HE].

[156] S. S. Wilks. “The Large-Sample Distribution of the Likelihood Ratio for Testing Composite Hypotheses”. In: *Ann. Math. Statist.* 9.1 (Mar. 1938), pp. 60–62. DOI: 10.1214/aoms/1177732360. URL: http://dx.doi.org/10.1214/aoms/1177732360.

[157] Pierre Auger Collaboration. “Measurement of the cosmic-ray energy spectrum above 2.5 $\times 10^{18}$ eV using the Pierre Auger Observatory”. In: *Prd* 102.6, 062005 (Sept. 2020), p. 062005. DOI: 10.1103/PhysRevD.102.062005. arXiv: 2008.06486 [astro-ph.HE].

[158] M. L. McCall. “A Council of Giants”. In: *mnras* 440.1 (May 2014), pp. 405–426. DOI: 10.1093/mnras/stu199. arXiv: 1403.3667 [astro-ph.GA].

[159] Telescope Array Collaboration. “Testing a Reported Correlation between Arrival Directions of Ultra-high-energy Cosmic Rays and a Flux Pattern from nearby Starburst Galaxies using Telescope Array Data”. In: *Astrophys. J. Lett.* 867.2, L27 (Nov. 2018), p. L27. DOI: 10.3847/2041-8213/aaebf9. arXiv: 1809.01573 [astro-ph.HE].

[160] Pierre Auger Collaboration. “Correlation of the Highest-Energy Cosmic Rays with Nearby Extragalactic Objects”. In: *Science* 318.5852 (2007), pp. 938–943. DOI: 10.1126/science.1151124. eprint: https://www.science.org/doi/pdf/10.1126/science.1151124. URL: https://www.science.org/doi/abs/10.1126/science.1151124.

[161] the Pierre Auger Collaboration. “Update on the correlation of the highest energy cosmic rays with nearby extragalactic matter”. In: *Astropart. Phys.* 34.5 (Jan. 2010), pp. 314–326. DOI: `10.1016/j.astropartphys.2010.08.010`. arXiv: `1009.1855 [astro-ph.HE]`.

[162] The Fermi Collaboration. “Fermi Large Area Telescope Fourth Source Catalog”. In: *Astrophys. J. Suppl. S.* 247.1 (Mar. 2020), p. 33. DOI: `10.3847/1538-4365/ab6bcb`. URL: `https://dx.doi.org/10.3847/1538-4365/ab6bcb`.

[163] Q. Z. Liu, J. van Paradijs, and E. P. J. van den Heuvel. “A catalogue of low-mass X-ray binaries”. In: *Astron. Astrophys.* 368 (2001), pp. 1021–1054. DOI: `10.1051/0004-6361:20010075`.

[164] Liu, Q. Z., van Paradijs, J., and van den Heuvel, E. P. J. “Catalogue of high-mass X-ray binaries in the Galaxy (4th edition)”. In: *A&A* 455.3 (2006), pp. 1165–1168. DOI: `10.1051/0004-6361:20064987`. URL: `https://doi.org/10.1051/0004-6361:20064987`.

[165] F Coti Zelati et al. “Systematic study of magnetar outbursts”. In: *J Phys.* 932.1 (Dec. 2017), p. 012022. DOI: `10.1088/1742-6596/932/1/012022`. URL: `https://dx.doi.org/10.1088/1742-6596/932/1/012022`.

[166] S. Olausen and V. Kaspi. “The McGill Magnetar Catalog”. In: *Astrophys. J. Suppl S* 212 (Sept. 2013). DOI: `10.1088/0067-0049/212/1/6`.

[167] G. Hobbs et al. “The atnf pulsar catalogue”. In: *IAU Symp.* 218 (2004), p. 139. arXiv: `astro-ph/0309219`.

[168] R. L. Fleischer et al. “Criterion for Registration in Dielectric Track Detectors”. In: *Phys. Rev.* 156 (1967), pp. 353–355. DOI: `10.1103/PhysRev.156.353`.

[169] J. Westgate, N NAESER, and Brent Alloway. “FISSION-TRACK DATING”. In: Jan. 2007, pp. 651–672. DOI: `10.1016/B0-444-52747-8/00052-1`.

[170] A. Gleadow et al. “Fission Track Dating of Phosphate Minerals and the Thermochronology of Apatite”. In: *REV MINERAL GEOCHEM* 48 (Jan. 2002), pp. 579–630. DOI: `10.2138/rmg.2002.48.16`.

[171] M. Toulemonde, C. Dufour, and E. Meftah A.and Paumier. “Transient thermal processes in heavy ion irradiation of crystalline inorganic insulators”. In: *NUCL INSTRUM METH B* 166 (May 2000), pp. 903–912. DOI: 10.1016/S0168-583X(99)00799-5.

[172] P. B. Price R. L. Fleischer and R. M. Walker. “Ion Explosion Spike Mechanism for Formation of Charged-Particle Tracks in Solids”. In: *Journal of Applied Physics* 36 (1965). DOI: https://doi.org/10.1063/1.1703059.

[173] Goto E. “On the Observation of Magnetic Poles”. In: *J. Phys. Soc. Japan* 13 (1958).

[174] S.L. Guo, S.F. Sun, et al. “Fission track dating of muscovite mica for searching for magnetic monopoles”. In: *International Journal of Radiation Applications and Instrumentation. Part D. Nuclear Tracks and Radiation Measurements* 15 (1988), pp. 703–705.

[175] R. L. Fleischer et al. “Search for magnetic monopoles in deep ocean deposits”. In: *Phys. Rev.* 184 (1969), pp. 1393–1397. DOI: 10.1103/PhysRev.184.1393.

[176] J.I. Collar and K. Zioutas. “Exotic Heavily Ionizing Particles can be Constrained by the Geological Abundance of Fullerenes”. In: *Phys. Rev. Lett.* 83 (1999).

[177] D.P. Snowden-Ifft, E.S. Freeman, and P.B. Price. “Limits on Dark Matter Using Ancient Mica”. In: *Phys. Rev. Lett.* 74 (1995).

[178] S. Baum et al. “Searching for Dark Matter with Paleo-Detectors”. In: *Phys. Lett. B* 803 (2020), p. 135325. DOI: 10.1016/j.physletb.2020.135325. arXiv: 1806.05991 [astro-ph.CO].

[179] A. Drukier et al. “Paleo-detectors: Searching for dark matter with ancient minerals”. In: *Phys. Rev. D* 99 (Feb. 2019). DOI: 10.1103/PhysRevD.99.043014.

[180] N. Tapia and S. Horiuchi. “Measuring solar neutrinos over gigayear timescales with paleo detectors”. In: *Phys. Rev. D* 103 (June 2021). DOI: 10.1103/PhysRevD.103.123016.

[181] S. Baum et al. “Galactic Geology: Probing Time-Varying Dark Matter Signals with Paleo-Detectors”. In: *Phys. Rev. D* (July 2021).

[182] J. F. Acevedo, J. Bramante, and A. Goodman. “Old Rocks, New Limits: Excavated Ancient Mica Searches For Dark Matter”. In: (May 2021). arXiv: `2105.06473 [hep-ph]`.

[183] A.s Bollhöfer et al. “High sensitivity airborne radon concentration measurements in the Alligator River Region: rehabilitated Nabarlek uranium mine”. In: (Nov. 2022).

[184] H. V. Gunten. “Distribution of mass in spontaneous and neutron-induced fission”. In: *Actinides Rev. 1* (1969), pp. 275–298.

[185] S. Baum et al. “New Projections for Dark Matter Searches with Paleo-Detectors”. In: *Instruments* (June 2021).

[186] W. Haxton, R. Robertson, and A. Serenelli. “Solar Neutrinos: Status and Prospects”. In: *Annual Review of Astronomy and Astrophysics* 51 (Aug. 2012). DOI: `10.1146/annurev-astro-081811-125539`.

[187] M. Agostini et al. “Experimental evidence of neutrinos produced in the CNO fusion cycle in the Sun”. In: *Nature* 587 (2020), pp. 577–582. DOI: `10.1038/s41586-020-2934-0`. arXiv: `2006.15115 [hep-ex]`.

[188] R. M. Bionta et al. “Observation of a Neutrino Burst in Coincidence with Supernova SN 1987a in the Large Magellanic Cloud”. In: *Phys. Rev. Lett.* 58 (1987), p. 1494. DOI: `10.1103/PhysRevLett.58.1494`.

[189] J. Jordan et al. “Measuring Changes in the Atmospheric Neutrino Rate over Gigayear Timescales”. In: *Phys. Rev. Lett.* 125 (Nov. 2020). DOI: `10.1103/PhysRevLett.125.231802`.

[190] “The Messinian Salinity Crisis: Past and future of a great challenge for marine sciences”. In: *Marine Geology* (2014). DOI: `10.1016/j.margeo.2014.02.002`.

[191] R. Boyd et al. “Science from detection of neutrinos from supernovae”. In: *J Phys G* 29 (Nov. 2003). DOI: `10.1088/0954-3899/29/11/009`.

[192] G. Allen et al. “On the Expansion Rate, Age, and Distance of the Supernova Remnant G266.2-1.2 (Vela Jr.)” In: *Astrophys. J.* 798 (Oct. 2014). DOI: `10.1088/0004-637X/798/2/82`.

[193] URL: `https://github.com/tedwards2412/paleopy`.

[194] T. Gaisser, R. Engel, and E. Resconi. “Cosmic Rays and Particle Physics”. In: 2nd edition. Cambridge University Press, 2016.

[195] S. Agostinelli et al. “Geant4 - A Simulation Toolkit”. In: *Nucl. Instrum. Meth. A* 506 (2003), pp. 250–303.

[196] M. Su, T. R. Slatyer, and D. P. Finkbeiner. “Giant Gamma-ray Bubbles from Fermi-LAT: AGN Activity or Bipolar Galactic Wind?” In: *Astrophys. J.* 724 (2010), pp. 1044–1082. DOI: 10.1088/0004-637X/724/2/1044. arXiv: 1005.5480 [astro-ph.HE].

[197] J. Bland-Hawthorn et al. “The Large-scale Ionization Cones in the Galaxy”. In: *Astrophys. J.* 886 (Nov. 2019), p. 45. DOI: 10.3847/1538-4357/ab44c8.

[198] P. Predehl et al. “Detection of large-scale X-ray bubbles in the Milky Way halo”. In: *Nature* 588.7837 (2020), pp. 227–231. DOI: 10.1038/s41586-020-2979-0. arXiv: 2012.05840 [astro-ph.GA].

[199] H. -Y. K. Yang, M. Ruszkowski, and E. G. Zweibel. “Fermi and eROSITA bubbles as relics of the past activity of the Galaxy’s central black hole”. In: *Nature Astron.* 6.5 (2022), pp. 584–591. DOI: 10.1038/s41550-022-01618-x. arXiv: 2203.02526 [astro-ph.HE].